LUDWIG-MAXIMILIANS UNIVERSITÄT MÜNCHEN

MASTER THESIS

Timing Calibration of the ATLAS Muon Spectrometer for a Search for charged stable massive Particles with Run–2 data

Author:
Philipp SEIFERMANN

Supervisor:
Dr. habil. Sascha MEHLHASE

A thesis submitted in fulfillment of the requirements for the degree of Master of Physics

in the

Faculty of Physics
Elementary Particle Physics

August 18, 2020

LUDWIG-MAXIMILIANS UNIVERSITÄT MÜNCHEN

MASTERARBEIT

Kalibration der Zeitmessung des ATLAS Muonspektromters für eine Suche nach geladenen stabilen massiven Teilchen mit dem Run–2 Datensatz

---

Author:
Philipp SEIFERMANN

Supervisor:
Dr. habil. Sascha MEHLHASE

Eine Masterarbeit erarbeitet im Zuge des Masterprogramms

an der

Fakultät für Physik
Elementarteilchenphysik

August 18, 2020

LUDWIG-MAXIMILIANS UNIVERSITÄT MÜNCHEN

Abstract

Faculty of Physics
Elementary Particle Physics

Master of Physics

Timing Calibration of the ATLAS Muon Spectrometer for a Search for charged stable massive Particles with Run–2 data

by Philipp SEIFERMANN

A timing calibration of the ATLAS Muon Spectrometer with 139 fb^{-1} of proton–proton collisions at $\sqrt{s}$ = 13 TeV during Run–2 is presented in the context of a search for charged stable massive particles. Charged stable massive particles leave the signature of heavy muon-like particles. Due to the their high mass, they are expected to traverse the detector at speeds well below the speed of light and thus offer a model-independent approach to observe New Physics. The low velocity manifests as long time-of-flight values, especially in the outer parts of the detector. The timing measurement of the muon spectrometer is thus an important variable for the identification of charged stable massive particles. A calibration procedure for the timing measurement is therefore necessary, involving calibration constants for over 725,000 individual detector elements.

Acknowledgements

Without the help and support of several people this master's thesis could not have been done. To anyone who supported me during the time it took to complete this work, I want to express my sincere gratitude.
Nevertheless, some people deserve to be mentioned specifically.

The first person I need to thank is Dr. habil. Sascha Mehlhase for his supervision of this thesis. Without his help this thesis would not have been possible. I want to especially emphasize the warm and positive attitude he nourished during my time in his research group.

Further, I am thankful to Prof. Dr. Dorothee Schaile for the opportunity to write this thesis at her chair in the first place and the kind and helpful work environment she fostered at her chair. Additionally, I would like to thank her for the possibility to visit CERN and ATLAS itself.

A special thanks to Ferdinand Krieter, who not only provided some of the framework used for this work but was also always willing to offer his support with any sort of problem that arose.

More generally, I would like to thank every member of the LS Schaile for the great work environment, joint lunches and occasional ping-pong breaks. I am lucky to say, that I could spend the time in such a kind-hearted and helpful atmosphere.

To Joschua Krink I want to express my sincere gratitude for almost six years of friendship. I am not sure how my academic studies would have evolved without him and the other members of the BlankoBlattBande. Especially as the usual work environment was not available any more, due to the Corona pandemic, the help he provided within the little office we set up was essential for finishing this work.

Last, but surely not least, I want to thank my family for the constant support I received during my studies and the time it took to write this thesis.

Contents

Chapter 1

Introduction

The general idea of elementary particle physics is to provide a description of the interactions between the smallest units that matter is build of in our universe. Over the years physicists provided continuous improvements to that description. Throughout the last decades a framework called the Standard Model of particle physics emerged as the leading theory. The Standard Model had huge success and was even able to predict particles exceeding the technological capabilities of detection at the time. With the discovery of the Higgs boson in 2012 [1, 2], the last remaining puzzle peace of the Standard Model was found. Even though the Standard Model was successfully tested throughout the years, it is known to be limited in its explanatory power. Indeed more and more observations in and outside the realm of particle physics occur, that can not be fully explained within the Standard Model. First and foremost a coherent implementation of gravity is not included inside the Standard Model. In addition, the Standard model is neither capable of providing a suitable dark matter candidate, needed to explain astrophysical and cosmological observations, nor is it able to explain the observed difference between anti-matter and matter observed in our universe.

Therefore, a variety of of theories Beyond the Standard Model (BSM), also called New Physics, are proposed aiming at resolving one or several shortcomings of the Standard Model. So far no one-fits-all solution was able to emerge, which allows for open-mindedness in the search for New Physics. However, many of these new theories include the existence of new particles, which could be created at particles colliders and be detected with modern detectors. As indications of their existence would have already been found, if these particles would have masses comparable to Standard Model particles, they are usually predicted with masses exceeding the range of Standard Model masses. The mechanisms that result in some long-living particles in the Standard Model, could similarly lead to new particles being either stable or having a life-time long enough to traverse the detector. Many proposed theories include such long-living particles carrying an electric charge, which are therefore called charged stable massive particles in this work.

Charged stable massive particles offer an interesting approach to a search for New Physics. Because of their charge and long life-time, they can be observed directly by a particle detector and not via the reconstruction of their decay. This autonomy of the specific decay process makes the search model-independent, as the exact production and decay process must not be known. Due to their large mass and available electromagnetic charge, a charged stable massive particle traversing a particle detector would suffer a large ionisation energy loss and would propagate through the detector with a velocity significantly slower than the speed of light. By measuring the time it took the traversing particle to reach the detector element it interacted

with, this velocity can be obtained. In addition to the model-independence, these searches have little to no Standard Model background because no Standard Model particle would leave such a signature. This leads to the detector mismeasurements being the main background that has to be considered for such an analysis. A clear understanding and a thorough calibration of the detector system used in the search is therefore necessary.

Within the ATLAS Collaboration, multiple searches for charged stable massive particles were conducted so far but none observed a significant excess over the estimated background. To gather information about the energy loss through ionisation the Inner Detector of ATLAS can be used and for a time-of-flight measurement the tile calorimeter, as well as the monitored drift tubes and resistive plate chambers of the Muon Spectrometer, can be used. The work at hand focuses on a timing calibration of the latter two detector parts placed in the outermost region of the detector using the data taken by ATLAS during Run–2 with a centre-of-mass energy of $\sqrt{s} = 13$ TeV. The thesis is structured as follows: in Chapter 2 an introduction of the theoretical framework of the Standard Model is given and the need for a search for charged stable massive particles is motivated. Chapter 3 introduces the experimental setup at CERN with focus on the LHC and ATLAS. The characteristics of charged stable massive particles at ATLAS are introduced in Chapter 4. Chapter 5 details the calibration procedure deployed in this work, as well as their effects on the timing measurement and the final resolution of the velocity. In the final Chapter 6 a conclusion and an outlook are given.

Chapter 2

Theory

The foundation of modern particle physics is given by the Standard Model. It describes the elemental building blocks of nature and three of the four known fundamental interactions in physics through quantum field theories. Even though the Standard Model is one of the best validated theories in physics, there are already known limitations in the applicability of it. Therefore, theorists have been imagining theories superseding the Standard Model for a while.
The following chapter will give a brief introduction into the particle content of the Standard Model and the interactions it describes. Since the work at hand focuses on long-lived particles in the context of New Physics, the subject of longevity will be addressed shortly, as well as the limitations of the Standard Model, and the need for a BSM theory will be motivated.
In this work, the for particle physics usual convention of $c := \hbar := 1$ is used.

2.1 The Standard Model of Particle Physics

The Standard Model describes all known building blocks of matter and their interactions through three of the four known fundamental forces, which are the electromagnetic, weak, strong and gravitational force. A proper description of gravity, in the context of a quantum field theory, has not been successful so far, and therefore, it is not included in the Standard Model. Even though gravity is dominant on large scales and consequently essential in fields like astrophysics, on small scales and at low energies, the effects of gravity are inconsequential compared to the effects of the other three forces and thus negligible in today's particle physics. Therefore, the absence of gravity does not entail a major detriment on the effectiveness of predictions made by the Standard Model. The fundamental building blocks and the particles that mediate the forces are assumed to be point-like, which means they do not have an inner structure and are thus called elementary particles. References [3, 4] give comprehensive introductions into the Standard Model and were used as inspirations for much of this chapter.

2.1.1 Elementary Particles

Elementary particles can be split into two major groups according to their spin. On the one hand, there are fermions which have half-integer spin and are the building blocks of matter. On the other hand, there are bosons, which have integer spin. They act as the mediators of the forces and are responsible for the particles attaining their masses.

Fermions

Fermions are further divided into three generations, where each partner of a higher generation has a higher mass but is the same otherwise. Furthermore, they can be divided according to their behaviour towards the strong interaction. Leptons are particles without the charge necessary for the strong interaction and thus do not take part in it. On the contrary, quarks have a colour charge and consequently do take part in the strong interaction. There are six different types of leptons gathered into two groups with three elements, respectively. Charged leptons have an electric charge of $-1e$, where e is the elementary charge[1] and contain the electron (e^-), muon (μ^-) and tauon (τ^-). The neutral leptons have fittingly an electric charge of 0 and encompass the electron neutrino (ν_e), muon neutrino (ν_μ) and tauon neutrino (ν_τ).

Within each generation of leptons, there is a pair of one charged and one neutral lepton. The first generation consists of the combination of electron and electron neutrino (e^-,ν_e), the second generation contains the muon and the muon neutrino (μ^-,ν_μ) and the third generation encloses the tauon and the tauon neutrino (τ^-,ν_τ). Similar to leptons, quarks come in in three generations with two elements each. One element is an up-type quark and the other is a down-type quark. Each up-type quark carries an electric charge of $\frac{2}{3}e$ and one of the three colour charges red (r), blue (b) or green (g). The three different up-type flavours are called up (u), charm (c) and top (t). The three down-type quarks, down (d), strange (s) and bottom (b), posses an electric charge of $-\frac{1}{3}e$ and, similar to the up-type quarks, one of the three colour charges. The up and down quarks build the doublet (u,d) of the first generation, the charm and strange quarks form the doublet (c,s) for the second generation and the doublet of the third generation consists of the top and bottom quark (t,b). An overview of the leptons can be found in Table 2.1 and of the quarks in Table 2.2.

Additionally, the Standard Model contains an anti-particle for each fermion. Anti-particles have the same mass as the corresponding particle but have opposite charges, except spin. The anti-particles of the quarks ($\bar{u}$, $\bar{d}$, $\bar{c}$, $\bar{s}$, $\bar{t}$, $\bar{b}$) and neutrinos ($\bar{\nu_e}$, $\bar{\nu_\mu}$, $\bar{\nu_\tau}$) are usually denoted by a bar over the symbol of the associated particle, and anti-quarks carry one of the anti-colours anti-red ($\bar{r}$), anti-blue ($\bar{b}$) or anti-green ($\bar{g}$). However, for the charged leptons, the bar is often replaced by an explicit denotation of the positive electric charge (e^+, μ^+, τ^+).
Furthermore, the fermions have a property called chirality containing two possible eigenstates, called left-handed and right-handed. The weak interaction discriminates between left-handed and right-handed fermions.

	Leptons			
	Particle	Symbol	El. charge [e]	Mass [MeV]
1^{st} generation	electron	e^-	-1	0.511
	electron neutrino	ν_e	0	$< 225 \cdot 10^{-6}$
2^{nd} generation	muon	μ^-	-1	106
	muon neutrino	ν_μ	0	< 0.19
3^{rd} generation	tauon	τ^-	-1	1776.82 ± 0.16
	tauon neutrino	ν_τ	0	< 18.2

TABLE 2.1: Leptons of the Standard Model, ordered by generation. Masses taken from [5].

[1]The electric charge of a proton; $e = 1.602176634 * 10^{-19} C$.

	Quarks			
	Particle	Symbol	El. charge [e]	Mass [MeV]
1st generation	up	u	$+2/3$	$2.3^{+0.7}_{-0.5}$
	down	d	$-1/3$	$4.8^{+0.5}_{-0.3}$
2nd generation	charm	c	$+2/3$	$(1.275 \pm 0.025) \cdot 10^3$
	strange	s	$-1/3$	95 ± 5
3rd generation	top	t	$+2/3$	$(173.21 \pm 1.22) \cdot 10^3$
	bottom	b	$-1/3$	$(4.25 \pm 0.15) \cdot 10^3$

TABLE 2.2: Quarks of the Standard Model, ordered by generation. Masses taken from [5].

Bosons

Since the spin of a particle can either be integer or half-integer, all non-fermionic particles are bosons. The Standard Model knows two types of bosons: gauge bosons with a spin of 1, which act as mediators for the fundamental forces, and one scalar boson with a spin of 0, which is the excitation of the field responsible for the particles attaining their masses. Each interaction has its own set of mediator particles.
The electromagnetic interaction is conveyed by the electrically neutral and colourless photon (γ), which can couple to every electrically charged particle. Gluons (g) are the mediators of the strong force and interact with all colour-charged particles. Gluons are electrically neutral, however they do carry colour charge[2] themselves and are therefore able to interact with other gluons. In total there are eight independent combinations of the colours (r,b,g) and anti-colours ($\bar{r}$,$\bar{b}$,$\bar{g}$) and thus eight different glouns. Since the symmetries of the underlying theory of the electromagnetic interaction and strong interaction are not broken, their mediators are massless. However, this is not the case for the weak interaction. The symmetry of the electroweak interaction is spontaneously broken and therefore the mediators of the weak force have mass while the photon remains massless. These mediators are the colourless and electrically charged W^+- and W^--bosons and the colourless and electrically neutral Z^0-boson.
The last and also most recently confirmed member of the Standard Model is the scalar Higgs boson (H^0) [1, 2]. The H^0-boson is electrically neutral and colourless, couples to all massive particles, and acts as the mediator of the Higgs-field. Due to the Higgs mechanism, the Higgs-field gives the $W^\pm$- and Z^0-bosons their masses, while quarks and leptons get their masses through Yukawa-coupling with the Higgs field. An overview of the bosons of the Standard Model is shown in Table 2.3.

	Bosons					
Interaction	Particle	Symbol	Mass [GeV]	Spin	El. charge [e]	Colour
electromagnetic	photon	γ	0	1	0	no
weak	W-boson	$W^\pm$	80.385 ± 0.015	1	± 1	no
	Z-boson	Z^0	91.1876 ± 0.0021	1	0	no
strong	gluon	g	0	1	0	yes
	Higgs	H^0	125.07 ± 0.4	0	0	no

TABLE 2.3: Bosons of the Standard Model, ordered by their corresponding interaction. Masses taken from [5].

[2] A gluon carries one colour and one anti-colour.

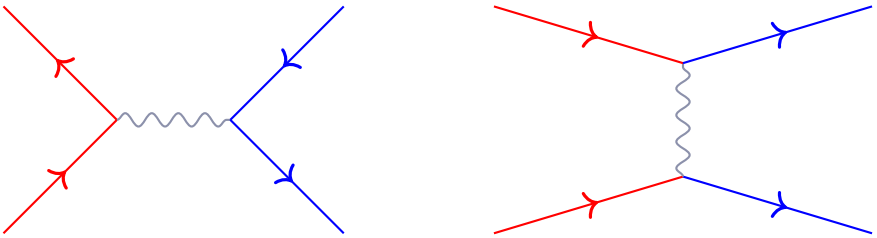

FIGURE 2.1: Schematic drawings of a Fewynman diagram.

2.1.2 Interactions

The mathematical framework used by the Standard Model is called quantum field theory (QFT). In a QFT, particles are described by excitations of the field and their interactions correspond to the interaction terms of these fields. Bound states, decays and scattering are investigated as probes for the interactions of the elementary particles. By evaluating the dynamics through Feynman diagrams, which are graphical depictions of the process at hand, and the kinematics by evaluating the available phase space, through the medium of the momenta and masses of the involved particles, one can calculate lifetimes for decays and cross-sections for scattering events.

A schematic drawing of such Feynman diagrams is shown in Figure 2.1. The red lines represent the incoming particles and the blue lines represent outgoing particles. Those four external lines embody visible particles and the grey line represents a virtual particle that can not be measured directly. Opposite to the observable particles, the virtual particle can have any mass and is called off-shell when the mass differs from its rest-mass. Even though any mass is possible, when the mass difference to the rest-mass becomes bigger, the process becomes less likely.

The Feynman diagram depicted in Figure 2.1 shows a process composed of three-point interactions, these interaction points are called vertices. These three-point vertices are the dominant building blocks of all higher-order diagrams. Each vertex introduces a factor $\sqrt{\alpha_i}$ where α_i is the coupling constant of the interaction the vertex belongs to. The range on which an interaction can occur depends on the mass of its mediator: a massless mediator gives rise to an infinite range on which the interaction can occur, a mediator with mass restricts the range.

Electromagnetic Interaction

The quantum field theory used to describe the electromagnetic interaction is called quantum electrodynamics (QED). QED is a gauge theory with $U(1)_{QED}$ as a symmetry group. The mediator of QED is the photon which couples with electric charges and therefore couples with all quarks and charged leptons, as well as charged composite particles. A coupling of the photon to the $W^{\pm}$-bosons is possible, however, this process is very rare. Figure 2.2 shows the emission or absorption of a photon (γ) by a charged fermion ($f^{\pm}$). This is the basic vertex of all QED processes. The coupling constant of the electromagnetic interaction is α_{em} ($\sim \frac{1}{137}$), for small energy scales. Since the photon is massless, the electromagnetic interaction has an infinite range.

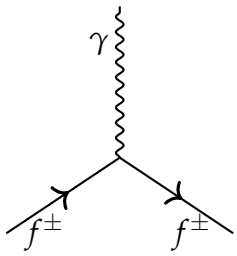

FIGURE 2.2: Feynman diagram showing the fundamental QED vertex.

Weak Interaction

As the name suggests, the weak interaction is significantly weaker than the other two interactions described in the Standard Model and is solely responsible for flavour changing processes. The weak interaction can be described by the symmetry group $SU(2)_L$. The mediators of the weak interaction couple to the weak isospin. All left-handed fermions and right-handed anti-fermions do possess a weak isospin and therefore take part in the weak interaction.

The interactions of the weak force can be divided into two different types. The charged current is mediated by a $W^{\pm}$-boson and acts only on left-handed fermions and right-handed anti-fermions. The neutral current is mediated by the Z^0-boson and acts with differing strength on left-handed and right-handed fermions or anti-fermions. Their fundamental vertices are shown in Figure 2.3, where Figure 2.3a shows the fundamental vertex of the charged current, which couples the $W^{\pm}$-bosons to either an up-type and down-type quark combination or to a combination of a lepton and the corresponding neutrino. Meanwhile Figure 2.3b shows the basic vertex of the neutral current, which couples the Z^0-boson to all fermions. While the neutral current is similar to the fundamental vertex of QED, with the exception that the Z^0 -boson also couples with neutrinos, the charged current differs significantly. For leptons, this vertex corresponds to the conversion of a charged lepton into a neutrino of the same generation or vice versa. When the charged current involves quarks it connects up-type quarks with down-type quarks and allows conversion between them. This conversion is not bound by interactions inside one generation.

This is explained by the weak interaction not acting on the mass eigenstates but rather acting on weak eigenstates. The weak eigenstates of up-type quarks are the same as the mass eigenstates. However, for down-type quarks, the weak eigenstates are a linear combination of the mass eigenstates. This connection of weak eigenstates to mass eigenstates is expressed in Equation 2.1. The connecting matrix is the CKM[3] matrix. Therefore, the charge current of the weak interaction acts on left-handed doublets and not at all on the right-handed singlets shown in Figure 2.4. The coupling constant of the weak interaction is α_w ($\mathcal{O}(10^{-7} - 10^{-6})$) and since all mediators of the weak force are massive, the range is restricted to approximately $\mathcal{O}(10^{-16})$ m.

$$\begin{pmatrix} d' \\ s' \\ b' \end{pmatrix} = \begin{pmatrix} V_{ud} & V_{us} & V_{ub} \\ V_{cd} & V_{cs} & V_{cb} \\ V_{td} & V_{ts} & V_{tb} \end{pmatrix} \cdot \begin{pmatrix} d \\ s \\ b \end{pmatrix} \tag{2.1}$$

[3]Named after Nicola Cabibbo, Makoto Kobayashi and Toshihide Maskawa.

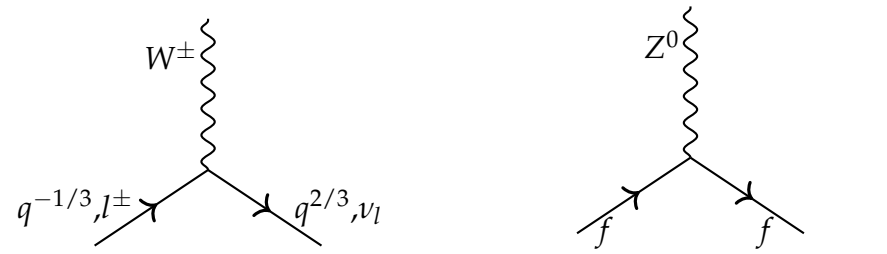

(A) Vertex of the charged current. (B) Vertex of the neutral current.

FIGURE 2.3: Feynman diagram showing the two fundamental weak vertices. (A) shows the vertex for the coupling via the charged current and (B) depicts the coupling for the neutral current.

$$\begin{pmatrix} u \\ d' \end{pmatrix}_L \quad \begin{pmatrix} c \\ s' \end{pmatrix}_L \quad \begin{pmatrix} t \\ b' \end{pmatrix}_L \qquad\qquad \begin{pmatrix} \nu_e \\ e \end{pmatrix}_L \quad \begin{pmatrix} \nu_\mu \\ \mu \end{pmatrix}_L \quad \begin{pmatrix} \nu_\tau \\ \tau \end{pmatrix}_L$$

$$u_R \, d_R \, c_R \, s_R \, t_R \, b_R \qquad\qquad e_R \, \mu_R \, \tau_R$$

FIGURE 2.4: Division of fermions in left-handed doublets and right-handed singlets.

Electroweak Unification

While the electromagnetic and the weak interaction seem to be rather different at low energies, they can be treated on equal footing at the scale of $\mathcal{O}(100\,\mathrm{GeV})$. Therefore, both interactions can be expressed by a unified gauge theory which is based on the symmetry group $SU(2)_L \otimes U(1)_Y$ and often called Glashow–Weinberg–Salam–model[4] (GSW model). Where $Y := 2(Q - I_3)$ is the hypercharge, which is a combination of the electric charge Q and the third component of the weak isospin I_3. As mediators of the GWS model, there are the gauge bosons W^0, W^1, W^2 which couple with the weak isospin, and the B^0 which couples to the hypercharge. Since the W bosons couple to the weak isospin, they are only able to interact with left-handed fermions and right-handed anti-fermions. The mediators of the electromagnetic and weak interaction can now be expressed as linear combinations of these gauge-bosons. This combination is given in Equation 2.2 with the weak mixing angle θ_W[5]. This admixture explains the different treatment of left-handed and right-handed fermions in the weak interaction. The combination of the photon leads to an equal treatment of the different handednesses. In order to explain why three of the four mediators have mass, the mechanism of spontaneous symmetry breaking (also known as Higgs mechanism) was introduced in 1964 and incorporated into the GWM model.

$$W^{\pm} = \frac{1}{\sqrt{2}}(W^1 \pm W^2) \quad Z^0 = W^0 \cos\theta_W - B \sin\theta_W \quad \gamma = W^0 \sin\theta_W + B \cos\theta_W \tag{2.2}$$

[4]S.L. Glashow, S.Weinberg and A.Salam were rewarded with the Nobel price in 1979 for their work on the electroweak unification.

[5]$\sin^2(\theta_W) = 0.231$ [5]

Strong Interaction

The model describing the strong interaction is a quantum field theory called quantum chromodynamics (QCD), which has a $SU(3)_C$ symmetry. The mediator of the strong force is the massless and electrically neutral gluon (g). The gluon couples to colour charges and is itself colour-charged, and therefore able to interact with itself. Quarks are the only Standard Model particles, other than gluons, that carry colour charge and are thus the sole participant in strong interactions. Some of the possible QCD vertices are shown in Figure 2.5 with exemplary colours. Figure 2.5a is the basic QCD vertex which depicts the interaction of a quark with a gluon, where the incoming quark radiates a gluon and thereby changes its colour. Figure 2.5b and Figure 2.5c show the three-gluon and four-gluon vertices, respectively. Since one gluon can actually couple to itself, and gluons can even form bound states, the spectrum of possible QCD vertices is much richer.

The coupling constant of the strong force is $\alpha_S \sim \mathcal{O}(1)$. This means that in contrast to the electroweak force, higher-order diagrams do not decrease in their importance on the described process. However, this is not the coupling actually observed in experiments. Similar to the screening effect a dipole resting in between two charges has, there is a screening effect in QCD. Due to the strong coupling, this screening mechanism is rather strong which leads to the coupling being distance dependent. For short distances, the quarks get asymptotically free, whereas the coupling gets stronger for longer distances. This behaviour of the strong interaction induces an important consequence called confinement. Confinement states that colour-charged particles do not appear isolated on observable scales. Consequently, quarks and gluons form overall colourless bound states. Even though the gluon is massless and therefore the strong force has an infinite range in theory, due to confinement, its effective range is restricted to approximately $\mathcal{O}(10^{-15})$ m.

While combinations of solely gluons, so-called glueballs, are possible, they have not been found yet. For quarks, this means that they need to build colour neutral states called hadrons. There are two ways to achieve that. One is to combine a colour with its anti-colour and thus form a colourless black state. Hence, a quark is combined with an anti-quark and forms a so-called meson. The other possibility is to combine all three colours, or anti-colours,and build the colourless white state. These particles, consisting of three quarks or three anti-quarks, are called baryons or anti-baryons, respectively.

Another interesting consequence of the distance dependence of the coupling strength is that, much like a spring, while two colour-charged particles move apart, the field between them grows stronger. Once the distance between the particles is large enough, it is energetically favourable to produce a $q\bar{q}$ pair out of the vacuum. This process is depicted in Figure 2.6. Since modern collider experiments produce colour-charged particles with sufficient momentum, this pair creation occurs until the kinematic energy falls below a certain threshold, and the coloured partons combine into colour neutral hadrons. This process is called hadronisation and leads to a signature in the detector called jet, several hadrons going in approximately the same direction.

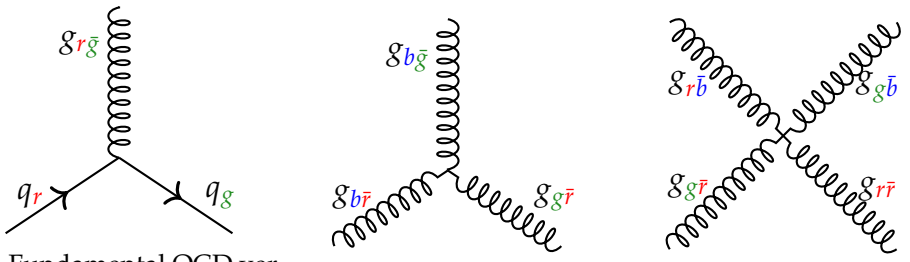

(A) Fundamental QCD vertex involving two quarks and a gluon.

(B) Gluon three-point interaction vertex.

(C) Gluon four-point interaction vertex.

FIGURE 2.5: Feynman diagrams showing the three QCD vertices.

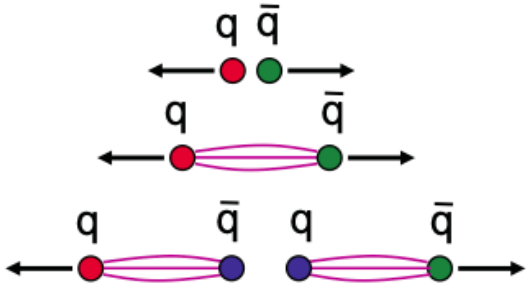

FIGURE 2.6: The result of colour confinement in QCD. Two separating quarks increase the force between them. To counteract the field in between them, two new quarks are created. Figure taken from [6].

The entire Standard Model can thus be described as a quantum field theory with a $SU(3)_C \otimes SU(2)_L \otimes U(1)_Y$ symmetry. The properties of the individual interactions are summarised in Table 2.4.

Interaction	Mediator	Strength	Range [m]
electromagnetic	γ	$\sim 1/137$	∞
weak	$W^{\pm}$ Z^0	$\sim 10^{-6}$	$\mathcal{O}(10^{-16})$
strong	g	1	$\mathcal{O}(10^{-15})$

TABLE 2.4: Overview of the properties of the interactions.

2.2 Lifetime of Particles

In the context of QFT, the lifetime is not a discrete value but rather a mean value that is used for a statistical description of the chance of a particle already having decayed after a certain time. For large enough sample sizes, the decay follows the Equation 2.3a where $N(t)$ is the number of particles after the time t when there were N_0 particles in the sample, to begin with, and Γ_{tot} is the total decay rate. Since particles often have several channels they can decay into, the total decay rate is simply the sum of all decay rates for the individual channels Γ_i, see Equation 2.3b.

$$N(T) = N_0 \cdot e^{-\Gamma_{tot} t} \qquad \Gamma_{tot} = \sum_i \Gamma_i \qquad \tau = \frac{1}{\Gamma_{tot}} \tag{2.3a-c}$$

$$\Gamma = \frac{(2\pi)^4}{2M} S \int |\mathcal{M}|^2 \delta^4 \left(P - \sum_{i=1}^{n} p_i \right) \prod_{i=1}^{n} \frac{d^3 \vec{p}_i}{(2\pi)^3 2E_i} \tag{2.4}$$

For every single decay channel, Γ_i can be calculated using Fermi's Golden Rule, displayed in Equation 2.4. M and P are the mass and four-momentum of the decaying particle. p_i and E_i are the four-momentum and energy of the decay products. S is a statistical factor accounting for identical particles. The absolute value of the matrix element $|\mathcal{M}|$, sometimes called amplitude, can be calculated using Feynman calculus and includes all dynamical properties of the process. The δ-function ensures that energy- and momentum-conservation is upheld. As can be seen in Equation 2.3c the total decay rate is connected to the mean lifetime τ, which is the average the time it takes for a particle to decay.

These dependencies on the lifetime τ lead to a couple of reasons for a long mean lifetime of a particle.

- Due to energy-conversation, particles are only able to decay into lighter particles. Therefore, the lightest particle in a system including a conserved, or almost conserved, quantum number has no possible decay mode that would not violate the conserved quantity and thus a long τ. This can be seen for example with the proton (p). Protons are the lightest baryons and the baryon number is a conserved quantity. Consequently, a free proton has an extremely long mean lifetime.[6]

- When the available phase space for the decay is limited, the integral in Equation 2.4 leads to a small outcome. This happens when there is a slightly heavier particle than the lightest particle of a system of an (almost) conserved quantum number. As an example serves the neutron which is the second lightest baryon and only a little heavier than its decay products p, e^- and $\bar{\nu_e}$. The already rather weak β-decay is further suppressed, which leads to a neutron lifetime of $\tau_n \approx$ 880 seconds [8].

- The dynamics of the process can be in a way that $\mathcal{M}$ becomes small. This can be achieved if the process is allowed only in higher-level Feynman diagrams or the participating virtual particle has a large mass difference to its usual rest-mass. More generally, due to the weak coupling, decays via the weak interaction usually lead to longer lifetimes as well. The long lifetime of the muon $\tau_\mu = 2.197 \mu s$ [5] is caused by the process only being possible via the weak force and since the muon is much lighter than the W^-. Its decay can be seen in Figure 2.7.

[6] The half-live of the proton is larger than $\mathcal{O}(10^{33} years)$ [7].

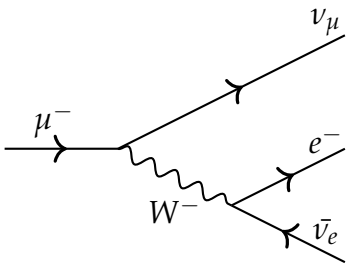

FIGURE 2.7: Feynman diagram for the decay of the muon.

2.3 The need for New Physics

The Standard Model is one of the experimentally best tested and verified theories in physics and had tremendous success in many of its predictions. As examples for this serve the prediction of the existence of the charm and top quarks [9, 10] and the bosons $W^\pm$, Z^0 and H^0 [11, 12]. Nonetheless, there are open questions that cannot be solved within the Standard Model, and therefore might need an extension of it or even a new theory altogether. One of the instances that could be solved, through an extension of the Standard Model, was the observation of neutrino oscillations[7] [13]. Since neutrino oscillations are only possible if neutrinos possess mass and the Standard Model considered them massless, the Standard Model needed to be extended towards massive neutrinos [4].

Unification of the Forces GUT

Since the electroweak unification already provided a mechanism that encloses the description of two fundamental interactions in one model, theorists believe that there could also be a theory combining the electromagnetic, weak and strong force into one model, called Grand Unified Theory (GUT). This is expected to happen at the GUT scale at $\mathcal{O}(10^{16}\ \text{GeV})$ [14], and would imply that the coupling constants of the electromagnetic, weak and strong interaction become similar at the GUT scale. As shown in Figure 2.8a extrapolations from the Standard Model to the GUT scale do not yield that result. Therefore, new physics between the weak scale and the GUT scale is necessary for a possible unification, as sketched in Figure 2.8b.
At the Planck scale $\mathcal{O}(10^{19}\ \text{GeV})$ gravitational effects can no longer be neglected in particle interactions and thus a full description would need to incorporate a quantum-mechanical description of gravity[8]. Therefore, opening the possibility for a further unification sometimes referred to as Theory of Everything.

Dark Matter

There are astrophysical observations, such as galactic rotation curves [17], stellar velocity dispersions [18], effects of gravitational lensing [19] or general cosmological models [20] which hint to the existence of large amounts of massive matter that does not interact electromagnetically or strongly and cannot be explained by the Standard Model. Since this matter does not interact electromagnetically, it cannot be seen with any sort of light and is therefore called dark matter. Recent measurements by the Planck satellite [21] conclude that the matter composed by the Standard Model

[7] Takaaki Kajita and Arthur McDonald received the Nobel prize in 2015 for that discovery.

[8] The current description of gravity, given by general relativity, seems to be fundamentally incompatible with the Standard Model [15].

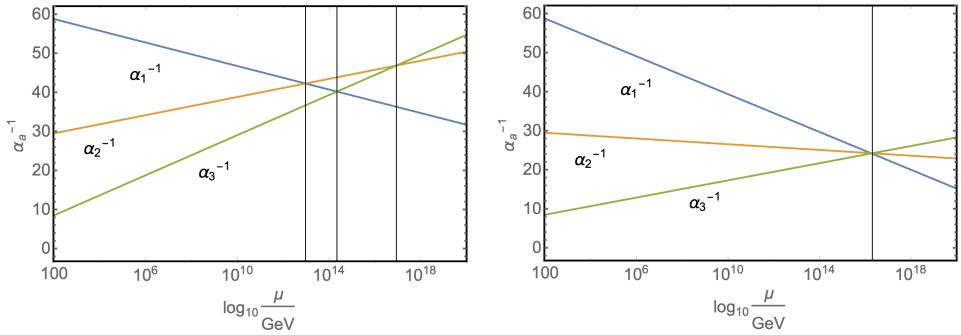

(A) SM (B) MSSM

FIGURE 2.8: Progression of gauge couplings $\alpha_{1,2,3}^{-1}$ for the electromagnetic (in blue), weak (in orange) and strong (in green) interaction as a function of momentum transfer Q and grey vertical lines for intersection points. Extrapolations of the Standard Model (SM) are shown in (A) and an example of BSM physics is shown in (B), in form of a Minimal Supersymmetric Standard Model (MSSM). Figures taken from [16].

only amounts to 4.9% of the total energy content of the universe, while dark matter amounts to 26.8%. The remaining 68.3% are referred to as dark energy, which counteracts gravity on large scales and leads to the accelerating expansion of the universe. This is one of the most baffling observations in contemporary physics. After the discovery of neutrino oscillations, it was suggested that dark matter is made of neutrinos. Due to the low upper limit on their mass in combination with their cosmic abundance, they could be ruled out as the sole constituent of dark matter [22].

Baryon Asymmetry

The Big Bang model predicts that matter and anti-matter are created in equal abundances, however our visible universe consists almost exclusively of matter. To explain this asymmetry there needs to be a process that discriminates between matter and anti-matter and thereby allows matter to become dominant. Such a process is called a charge-parity (CP) violating process. While CP violating processes exist in the Standard Model, the resulting asymmetry is orders of magnitude below the observation [23–25].

Hierarchy Problem

Even thought the discovery of the Higgs boson in 2012 [1, 2] is a success of the Standard Model, its mass of m_H =125 GeV gives rise to some concerns. The mass of the Higgs boson is closely related to the Higgs field, with the potential given in Equation 2.5, because of $\mu = \frac{m_H}{\sqrt{2}}$, m_H collects large quantum corrections from each particle the Higgs field couples to.

$$V(\Phi) = -\mu^2|\Phi|^2 + \lambda^2|\Phi|^4 \tag{2.5}$$

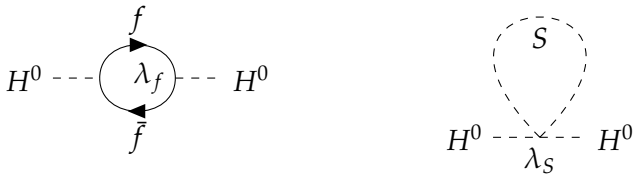

(A) Fermion interaction.

(B) Scalar boson interaction.

FIGURE 2.9: One-loop quantum correction to the physical Higgs mass coming from virtual loop couplings to fermions with coupling constant λ_f in (A) and to scalar bosons with coupling constant λ_S in (B).

$$m_H^2 = m_0^2 - 6\lambda_f^2 \int \frac{d^4k}{(2\pi)^4} \frac{1}{k^2} \qquad \Delta m_H^2 \approx -\frac{|\lambda_f|^2}{8\pi^2} \Lambda_{UV}^2 \tag{2.6a-b}$$

As shown in Equation 2.6a, the measured value m_H is therefore a combination of its bare mass m_0 and quantum corrections received through loop diagrams, like the one depicted in Figure 2.9a. The coupling constant of fermions to the Higgs field is λ_f and is related to the mass of the considered fermion. However, this integral does not converge and its computation is only possible by defining an ultraviolet cut-off Λ_{UV}, to which the theory is valid. The correction can then be expressed to first order as shown in Equation 2.6b [26]. Taking Λ_{UV} to the Planck scale[9] $\mathcal{O}(10^{19}$ GeV$)$ leads to enormous mass corrections about 34 orders of magnitude larger than m_H [27]. This raises the question why m_H[10] is ≈ 125 GeV and not much more massive, after all the quantum corrections need to cancel each other with astonishing precision and this fine-tuning is considered unnatural [28, 29].

2.4 Beyond the Standard Model

Because of the limitations of the Standard Model, as discussed in Section 2.3, there is a consensus that some form of BSM physics has to exist. While aiming to solve these problems, BSM theories must still be able to explain the current measurements that are well described by the Standard Model. Therefore, a commonly used approach is to embody the Standard Model in the context of a new and extended phenomenology. Even though there is a large variety of BSM physics, the following section will focus on perhaps the most prominent set, which involves a new fundamental symmetry between bosons and fermions called supersymmetry.

Supersymmetry

The primary intention of supersymmetry [30–35], often abbreviated as SUSY, is to address the hierarchy problem. Conveniently, it can also provide a unification of the electroweak and strong force [36–39] and dark matter candidates [40, 41]. Similar to the corrections to the Higgs mass m_H from fermions, expressed in Equation 2.6b, a process where the Higgs boson radiates and reabsorbs a hypothetical massive scalar particle coupling with constant λ_S is possible. The process is shown in Figure 2.9b

[9] Since a complete theory should be valid up to the Planch scale.

[10] And with it the entire mass spectrum of the Standard Model.

and yields a correction term for m_H, which is expressed to first order in Equation 2.7 [42].

$$\Delta m_H^2 \approx \frac{|\lambda_S|^2}{16\pi^2}[\Lambda_{UV}^2 - 2m_S^2 \ln(\frac{\Lambda_{UV}}{m_S})] \tag{2.7}$$

When each fermion of the Standard Model is associated with two scalar bosons, where $\lambda_S = |\lambda_f|^2$, the Λ_{UV}^2 terms in Equations 2.6b and 2.7 cancel nicely. This leads to the hypothesis that there is a new fundamental symmetry, called supersymmetry, which associates fermions to bosons and vice versa. The mathematical realisation of this is an operator Q that transforms fermionic states into bosonic ones and bosonic states into fermionic ones, as expressed in Equation 2.8.

$$Q|fermion\rangle = |boson\rangle \qquad Q|boson\rangle = |fermion\rangle \tag{2.8}$$

Further restrictions on the model can ensure that higher-order corrections also cancel each other. Particles linked by Q are called superpartners and form so-called supermultiplets [43]. Besides the spin, they are equal in their quantum numbers.

To distinguish between Standard Model particles and their superpartners, the superpartners of the Standard Model particles are denoted with an additional tilde "~" above the particle symbol. For the superpartners of Standard Model particles the naming convention is as follows: to represent their scalar nature, superpartners of fermions acquire the prefix "s" and thus are called sfermions, while superpartners of bosons pick up the suffix "ino". Therefore, the superpartners of gauge bosons are referred to as gauginos. Since left-handed and right-handed particles are treated differently in the Standard Model, both of them get linked to their own supersymmetric partner. Due to the scalar nature of that superpartner, they are, however, no longer left- and right-handed. This way there is at least one supersymmetric partner for each Standard Model particle. The entire set of supersymmetric partners of the Standard Model particles is often referred to as supersymmetric particles.

Since the term supersymmetry consolidates several different models, there are theories with a much larger particle content. To avoid gauge anomalies, the models have to add more particles than just the sfermions and gauginos [44]. The model with the smallest amount of added particles, that avoids these gauge anomalies, is called Minimal Supersymmetric (version of the) Standard Model (MSSM) and requires, in addition to sfermions and gauginos, five Higgs bosons and their higgsinos instead of the usual one [45]. In the MSSM the electroweak symmetry breaking, which gives the $W^{\pm}$- and Z^0-bosons their masses, leads to a mixing of the gauginos with the higgsinos into mass eigenstates. The uncharged gauginos ($\widetilde{B}$ and $\widetilde{W^0}$) and higgsinos ($\widetilde{H}_u^0$ and $\widetilde{H}_d^0$) build four neutral mass eigenstates, called neutralinos $\widetilde{\chi}_i^0$ ($i = 1, 2, 3, 4$)[11], and the charged winos ($\widetilde{W}^+$ and $\widetilde{W}^-$) and higgsinos ($\widetilde{H}_u^+$ and $\widetilde{H}_d^-$) form four charged eigenstates, called charginos $\widetilde{\chi}_i^{\pm}$ ($i = 1, 2$)[12] This mixing into new mass states also occurs for sfermions within one generation. For the first two generations this effect is negligible and thus ignored, while the third generation mixes into the mass eigenstates $\tilde{t}_i$, $\tilde{b}_i$ and $\tilde{\tau}_i$ ($i = 1, 2$). The entire additional particle content the MSSM predicts

[11] The convention is to order the labels by ascending mass, so that $m_{\widetilde{\chi}_1^0} < m_{\widetilde{\chi}_2^0} < m_{\widetilde{\chi}_3^0} < m_{\widetilde{\chi}_4^0}$.

[12] The convention is to order the labels by ascending mass, so that $m_{\widetilde{\chi}_1^{\pm}} < m_{\widetilde{\chi}_2^{\pm}}$.

Name	Spin	P_R	Gauge Eigenstate	Mass Eigenstate
Higgs Bosons	0	+1	$H_u^0\ H_d^0\ H_u^+\ H_d^-$	$h^0\ A^0\ H^\pm$
Squarks	0	-1	$\widetilde{u}_L\ \widetilde{u}_R\ \widetilde{d}_L\ \widetilde{d}_R$	(same)
			$\widetilde{s}_L\ \widetilde{s}_R\ \widetilde{c}_L\ \widetilde{c}_R$	(same)
			$\widetilde{t}_L\ \widetilde{t}_R\ \widetilde{b}_L\ \widetilde{b}_R$	$\widetilde{t}_1\ \widetilde{t}_2\ \widetilde{b}_1\ \widetilde{b}_1$
Sleptons	0	-1	$\widetilde{e}_L\ \widetilde{e}_R\ \widetilde{\nu}_e$	(same)
			$\widetilde{\mu}_L\ \widetilde{\mu}_R\ \widetilde{\nu}_\mu$	(same)
			$\widetilde{\tau}_L\ \widetilde{\tau}_R\ \widetilde{\nu}_\tau$	$\widetilde{\tau}_1\ \widetilde{\tau}_2\ \widetilde{\nu}_\tau$
Gluino	1/2	-1	$\widetilde{g}$	(same)
Neutralinos	1/2	-1	$\widetilde{B}^0\ \widetilde{W}^0\ \widetilde{H}_u^0\ \widetilde{H}_d^0$	$\widetilde{\chi}_1^0\ \widetilde{\chi}_2^0\ \widetilde{\chi}_3^0\ \widetilde{\chi}_4^0$
Charginos	1/2	-1	$\widetilde{W}^\pm\ \widetilde{H}_u^+\ \widetilde{H}_d^-$	$\widetilde{\chi}_1^\pm\ \widetilde{\chi}_2^\pm$
Gravitiino	3/2	-1	$\widetilde{G}$	(same)

TABLE 2.5: Additional particles predicted by the Minimal Supersymmetric Standrad Model. Table taken from (Cite martin 19)

is shown in Table 2.5, including their spin, gauge eigenstates, mass eigenstates and a new property P_R called R-parity.

R-parity

In order to explain the long lifetime of the proton, the Standard Model needs baryon number and lepton number conservation. However, many supersymmetric models do violate these conservations if no further measures are taken. Therefore, they often introduce a new multiplicative quantum number called R-parity[13], which is defined in Equation 2.9 [46], where S is the spin, B the baryon number and L the lepton number of the particle.

$$P_R = (-1)^{2S+3(B-L)} \tag{2.9}$$

All Standard Model particles and the added Higgs bosons have $P_R = +1$ and their superpartners have $P_R = -1$. In order to prohibit the proton decay, R-parity is often considered to be a conserved quantity[14] [48, 49], which has some notable implications. Interactions between Standard Model particles can only lead to the production of even numbers (mostly pairs) of supersymmetric particles. Furthermore, all supersymmetric particles have an odd amount of supersymmetric particles in their decay products and thus cannot decay into exclusively Standard Model particles. From there follows, that the Lightest Supersymmetric Particle (LSP) cannot decay any further and therefore is stable. If it is electrically neutral and carries no colour charge, it can function as a dark matter candidate. Many SUSY models keep the dark matter requirements in mind and lead to the lightest neutralino or the gravitino[15] being the LSP and thus a suitable dark matter candidate [50].

[13]Sometimes also referred to as matter parity.

[14]It is also possible to build models that do not conserve R-parity and lead to protons lifetimes many times larger than the age of the universe [47].

[15]Supersymmetric partner of the graviton, the mediator of gravity in a GUT.

Supersymmetry breaking

Supersymmetry has a noteworthy problem. If there where a perfect symmetry between particles and their superpartners, all supersymmetric particles would not only have the exact same quantum numbers, except the spin, but also exactly the same mass, which means they would be already produced at contemporary experiments and thus would be observable. Since no supersymmetric particle has been found to this day, supersymmetry must be a broken symmetry so the superpartners can differ in mass. There are several ways to introduce this breaking mechanism and SUSY models are often distinguished by their breaking mechanism. Many models include a separation of the observable SUSY sector from a hidden SUSY-breaking sector, for example by assuming additional spacetime dimensions [51, 52]. Different types of mediation between the visible and hidden sector lead to different models like gauge-mediated supersymmetry breaking (GMSB) [42, 53], anomaly-mediated supersymmetry breaking (AMSB) [54, 55] or minimal supergravity (mSUGRA) [56, 57]. However, the expected mass scale of many of those models is on the order of a few TeV and are therefore within the range of modern experiments [45, 58, 59]. Since there was no sign of a supersymmetric particle so far, experiments set increasingly stronger exclusion limits on the masses of supersymmetric particles [60, 61]. Thereby reducing the available phase space for supersymmetric particles substantially [62–64]. Unfortunately, with increasing mass difference between the Standard Model and supersymmetric particles the remaining possible models yield less pleasant solutions to the hierarchy problem [65].

Stable Massive Particles

Since many BSM theories want to have a dark matter candidate, and dark matter has to be stable on the time scale of the universe[16], many of them include Stable Massive Particles (SMPs). In models with additional compactified dimensions for example Standard Model particles are accompanied by Kaluza-Klein excitations, which differ in mass. A conserved symmetry leads to the lightest Kaluza-Klein particle being long-lived [66]. In supersymmetry many different models predict SMPs regardless of whether they conserve R-parity [67, 68] or not [69, 70]. In models that conserve R-parity the LSP is often a suitable candidate for dark matter and thus electrically neutral and colourless.

If the next-to-lightest supersymmetric particle is just slightly heavier than the LSP, it could be long-lived and traverse a particle detector and thus be considered stable. When it is electrically charged or carries an additional colour charge, it would interact with the detector and therefore would be detectable, see Section 3.2 and Chapter 4. One possibly exploitable difference to Standard Model particles is the considerably larger mass, which would lead to them propagating the detector at considerably lower velocities. Therefore, their signature could look like the signature of a much heavier and slower copy of a Standard Model particle. From the considerably slower velocity follows that searches for SMPs have a relatively small background of Standard Model processes with similar signatures in the event. However, detector effects do provide a background and therefore a good understanding of the detector itself is necessary before a search for charged stable massive particles can be conducted.

[16] Otherwise it would decay and would not be as abundant in the universe.

Depending on the exact breaking mechanism, the stau ($\widetilde{\tau}$), the lighter chargino ($\widetilde{\chi}_1^{\pm}$) or gluinos ($\widetilde{g}$) are possible candidates for charged stable massive particles in the MSSM. Similar to quarks, gluinos would hadronise into R-hadrons which would then interact with the detector and could even undergo a process that changes their charge. So far searches for SMPs remained unsuccessful but where able to place stringent limits on their minimal masses [71].

2.5 Summary

The Standard Model of particle physics describes elementary particles and three of their four know interactions. Even though it has been highly successful so far, it is incomplete and therefore physics beyond the Standard Model has to exist. One notable class of theories extending the Standard Model is called supersymmetry, which proposes a new fundamental symmetry between bosons and fermions. It predicts a set of new particles with similar quantum numbers, except for the spin. Due to the fact that such particles have not been found yet, the symmetry must be softly broken and the supersymmetric particles must have masses considerably larger than their Standard Model counterparts. Some of these models include charged stable massive particles, which would register the same information in the detector as a much heavier copy of the muon.

Chapter 3

The Experiment

This chapter focuses on the experimental setup. The **C**onseil **E**uropéen pour la **R**echerche **N**ucléaire (CERN) is one of the worlds largest research centres. It is located at the Franco–Swiss border near Geneva and mainly focuses on research in particle physics and hence operates different particle accelerators and hosts multiple detectors. CERN was founded in 1954 and was one of Europe's first joint ventures in science. Today there are 23 member states [72, 73].
At first, this chapter introduces the main experiment at CERN, the Large Hadron Collider (LHC) [74], followed by a brief description of the ATLAS Experiment [75] with a focus on the detector components relevant to this work.

3.1 The Large Hadron Collider

Currently, the LHC is the largest and most powerful particle collider in the world and is residing in the tunnel that was built for its predecessor, the Large Electron Positron Collider (LEP) [76–78]. As the name suggests LEP used to accelerate and collide electrons and positrons[1] whereas the LHC works with hadrons. More precisely, most of the time the LHC accelerates and collides protons[2]. During some special data-taking runs, called heavy-ion runs, the LHC also operates with lead-nuclei and produces proton–lead and lead–lead collisions [79]. This work uses data from pp collisions, therefore the following explanations focus on the proton–proton runs of the LHC. Since the synchrotron-radiation scales with the mass of the accelerated particle according to m^{-4} [80], hadron colliders can achieve much higher energies than electron–positron colliders could. This advantage in energy comes at a cost. While electrons and positrons are considered to be fundamental particles and therefore without substructure, hadrons do have substructure, their constituents are referred to as partons (quarks or gluons). From this follows, that the momenta of the interacting partons in hadron collisions are not known exactly, but rather described statistically by a distribution called parton distribution function (PDF). Furthermore, it is not clear which parton took part in the interaction or whether or not several partons of the same hadron took part in an interaction.

The tunnel of the LHC is located between 175 m (under the Jura) and 50 m (close to Lake Geneva) below the surface, resulting in a tilt of roughly 1,4%. The LHC's shape roughly describes a circle with a circumference of 26.659 km that is composed of eight arcs and eight straight sections. In order to bend the two particle beams along the arcs, a total of 1232 dipole magnets are used and 392 quadupole magnets

[1] Anti-electrons.
[2] A baryon build out of two up quarks and one down quark.

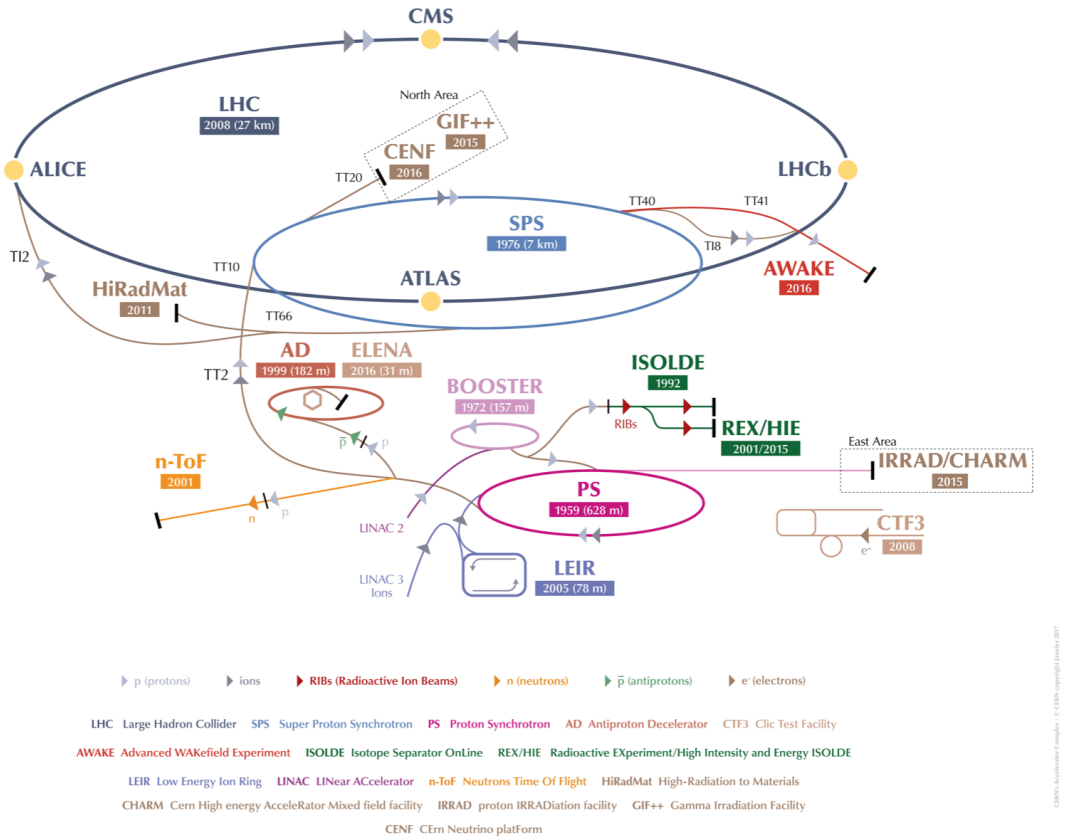

FIGURE 3.1: The accelerator complex of CERN [85].

are used to control the shape of the particle beams. To achieve the bending, the magnetic field created by the dipole magnets needs to be enormous, which can only be realised by superconducting electromagnets. Hence, the accelerator is connected to a cooling system using liquid helium which lowers the temperature of the magnets to 1.9 K[3], which is even colder than outer space. The strength of the magnetic field of the dipole magnets is the determining factor for the maximal centre-of-mass energy $\sqrt{s}$ the LHC can reach. The LHC was designed for a centre-of-mass energy of $\sqrt{s} = 14$ TeV and therefore 7 TeV per beam. Together with magnets used for beam-injection and beam-dumping, the total number of magnets operated by the LHC amounts to 9593 [81].

The eight straight sections are referred to as insertion regions. One of them contains eight radio-frequency cavities for each beam that are used for the acceleration of the beams. Four insertion regions contain interaction points, where the counter-rotating beams are crossed, resulting in proton–proton collisions. The four interaction points host the four large experiments at LHC called ALICE (**A** **L**arge **I**on **C**ollider **E**xperiment [82]), ATLAS (**A** **T**oroidal **L**HC **A**pparatu**S**, Section 3.2), CMS (**C**ompact **M**uon **S**olenoid [83]) and LHCb (**L**arge **H**adron **C**ollider **b**eauty[4] [84]). ATLAS and CMS are general-purpose detectors with a vast physics program, LHCb is specialised in studying the slight differences between matter and anti-matter and ALICE focuses on studying heavy-ion physics.

[3] $-271.3°C$

[4] The bottom-quark is sometimes referred to as beauty-quark.

Before the protons can be injected into the LHC they have to go through an injector chain, which subsequently increases the energy of the proton–beam. A schematic drawing of the full CERN accelerator complex is shown in Figure 3.1. As proton source, a bottle of hydrogen gas is used. After the electric field stripped the hydrogen atoms of their electrons, the remaining protons are accelerated to 50 MeV by a linear accelerator (Linac 2). Subsequently, the protons are injected into the Proton Synchrotron Booster (PSB), which brings them to 1.4 GeV. The Proton Synchrotron (PS) further increases their energy to 25 GeV. The Last stop, before entering the LHC, is the Super Proton Synchrotron (SPS) where the protons reach 450 GeV. From the SPS the protons are injected into the two beam pipes of the LHC, while being separated into 2808 different packages, called bunches, of approximately $1.2 \cdot 10^{11}$ protons with a time spacing of 25 ns[5] [81, 86]. The LHC is responsible for the acceleration to the final collision energy. During the first period of data taking, Run–1, the LHC operated at beam energies of 3.5 TeV(2010 and 2011) and 4 TeV (2012), which resulted in centre-of-mass energies of 7 TeV and 8 TeV, respectively [87]. After a two year period without data taking, used for upgrades and maintenance, the LHC resumed its operation in 2015 with a centre of mass energy of 13 TeV for the whole Run–2 that ended in 2018 [88].

As expressed in Equation 3.1a the rate of a process $\frac{dn}{dt}$ and its cross-section σ are related by a quantity called instantaneous luminosity L. L itself depends on many parameters of the accelerator and with the assumption of Gaussian shaped bunches, can be expressed as shown in Equation 3.1b. Where σ_x and σ_y are the widths in x- and y-direction of the Gauss shaped bunches, which revolve around the accelerator ring with frequency f. N_b is the number of bunches filled into each beam pipe and N_1 and N_2 are the amount of protons in each bunch. The LHC was designed with an instantaneous luminosity of 10^{34} cm^{-2}s^{-1} in mind [75] and by the end of 2017 actually managed to reach $2.06 \cdot 10^{34}$ cm^{-2}s^{-1} being twice its nominal value [89]. In order to go from the rate $\frac{dn}{dt}$ of a process to the total number of events during a specific data-taking run, one has to integrate over time. Therefore, the integrated luminosity, given in Equation 3.1c, serves as a measure of how much data was taken. The total amount of events N_i of a specific process i is described by Equation 3.1d.

$$\frac{dn}{dt} = L \cdot \sigma \qquad L = \frac{N_b f N_1 N_2}{4\pi\sigma_x\sigma_y} \qquad \mathcal{L} = \int L dt \qquad N_i = \sigma_i \cdot \mathcal{L} \tag{3.1a-d}$$

The evolution of the integrated luminosity $\mathcal{L}$ over the entire Run–2 data-taking period is shown in Figure 3.2a. Depicted in green is the amount the LHC was able to deliver to ATLAS, being $\mathcal{L}_{LHCDelivered} = 156$ fb^{-1}. The yellow part shows how much of that supply ATLAS was able to record, which is $\mathcal{L}_{ATLASRecorded} = 147$ fb^{-1}. The blue graph displays the extent which is deemed to be of good quality which therefore is usable for physics analysis. It reaches $\mathcal{L}_{GooodforPhysics} = 139$ fb^{-1}.

Since the time scale of a Run of the LHC is set, increasing the total amount of data being taken can only be done by increasing the rate at which data is taken. To do so the instantaneous luminosity needs to be enhanced. This however comes at a price: as each bunch includes several protons there is a chance that while the bunches

[5] $2.5 \cdot 10^{-8} s$

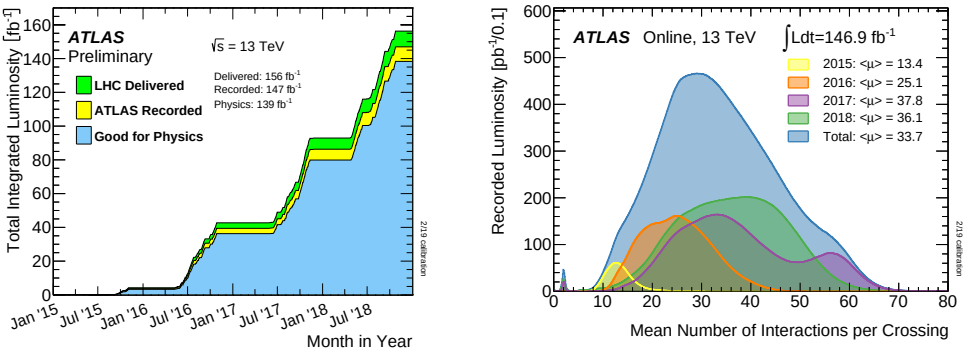

(A) Integrated Luminosity. $\mathcal{L}$ (B) Pileup profile in ATLAS.

FIGURE 3.2: The integrated luminosity $\mathcal{L}$ delivered by the LHC during Run–2 pp data-taking is shown in (A) and the pile-up profile during that period is shown in (B). Figures are taken from [90]

cross, several proton pairs collide and interact simultaneously. These additional interactions are referred to as pile-up and pose a challenge for the separation of each interaction and accordingly the reconstruction of the event. Figure 3.2b shows the pile-up profile for the recorded luminosity during Run–2, both separated for each year and combined. During the whole Run–2 an average of $\langle\mu\rangle = 33.7$ simultaneous interactions were recorded in ATLAS, with values reaching up to 70 interactions at once.

3.2 The ATLAS Detector

ATLAS is one of two multi-purpose particle detectors designed for a broad spectrum of studies, ranging from high-precision measurements of the Standard Model to a variety of studies beyond the Standard Model. ATLAS has a cylindrical shape with a length of 44 m and a diameter of 25 m and is the largest of the four experiments at the LHC. Figure 3.3 shows a schematic drawing of the detector with its subsystems. Similar to other multi-purpose particle detectors ATLAS has an onion-like structure around the beam pipe with layers of different detector systems. In order to achieve almost a full 4π coverage, ATLAS uses concentrical detector layers parallel to the beam pipe in its barrel region and layers of disks, called end-caps, with detector layers perpendicular to the beam pipe on both sides closing the barrel. Particles coming from the interaction point first reach the Inner Detector (ID, see Section 3.2.1), which is a tracking system embedded in a solenoidal magnetic field of 2 T [91]. The latter bends the trajectory of charged particles and allows for a precision momentum measurement. Following the ID there are two layers of calorimeters (see Section 3.2.2), the electromagnetic calorimeter and the hadronic calorimeter, where most particles are absorbed and their energy is evaluated. The last layer of ATLAS is another tracking system embedded in a 4 T toroidal magnetic field [91], in order to provide an additional momentum measurement of the traversing particle. Since muons and neutrinos are the only Standard Model particles that do not stop in the calorimeters and neutrinos interact too weakly for ATLAS to detect them, this last layer is called Muon Spectrometer (MS, see Section 3.2.3).

One of the reasons for this layering of the detector into subsystems is to allow for the identification of the particle traversing the detector. Since particles differ in their

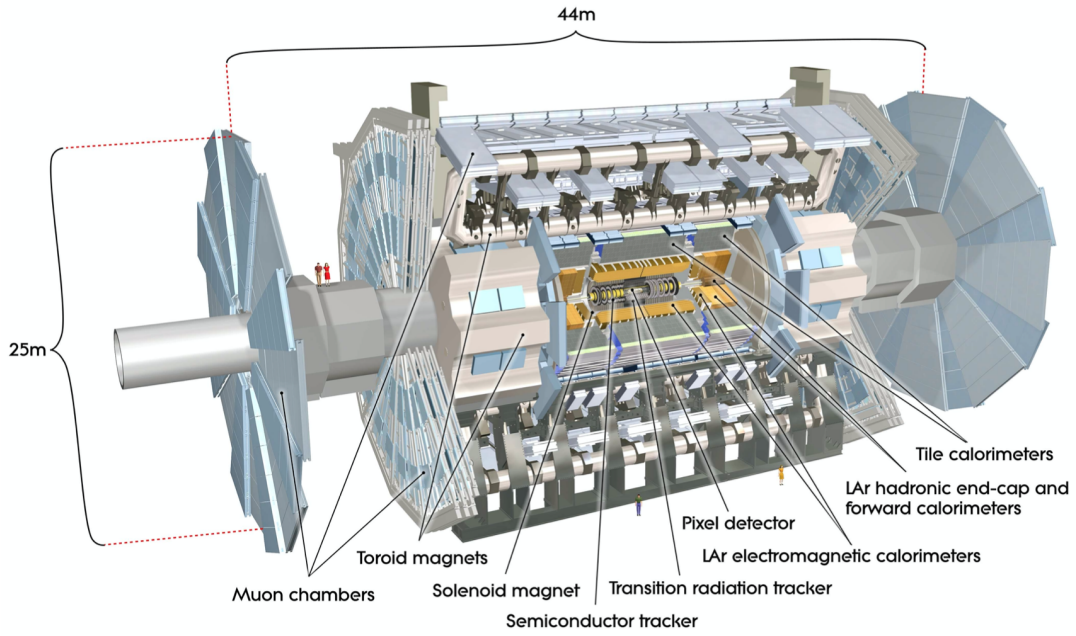

FIGURE 3.3: Computer-generated schematic drawing of the ATLAS detector with its subsystems labelled and two humans in proportion. Figure taken from [75].

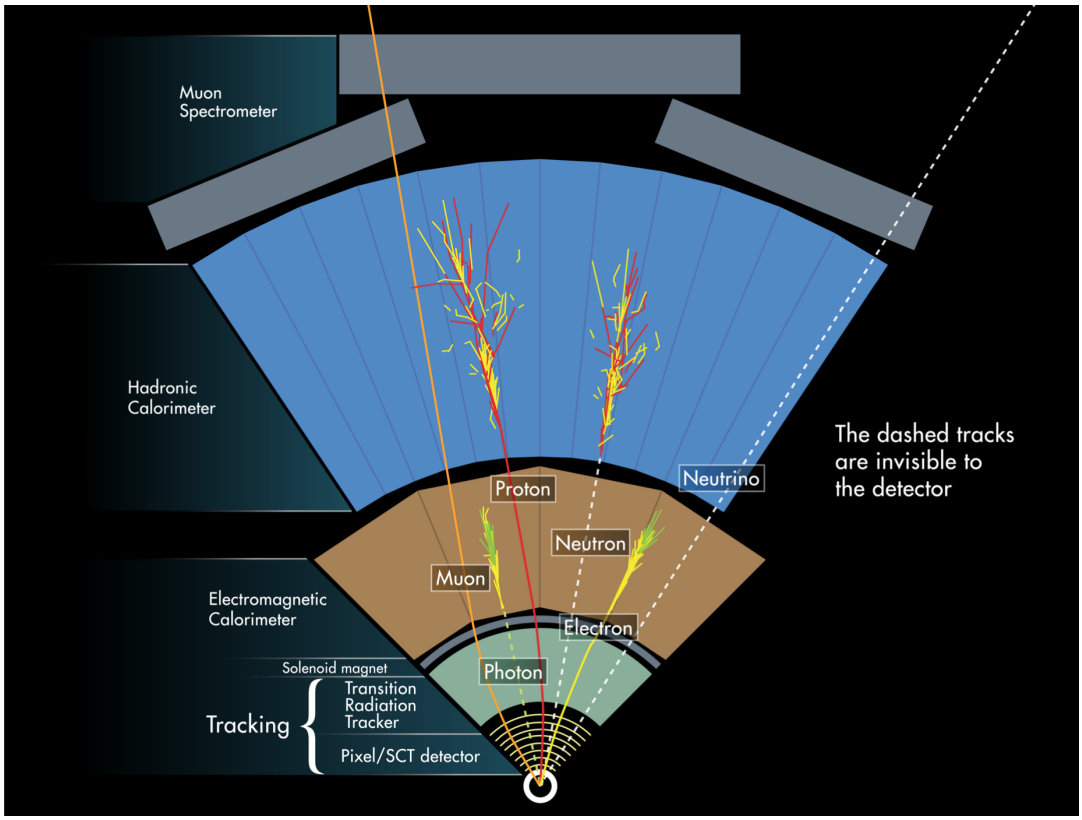

FIGURE 3.4: A slice of ATLAS showing how different particles interact with the subdetectors [92].

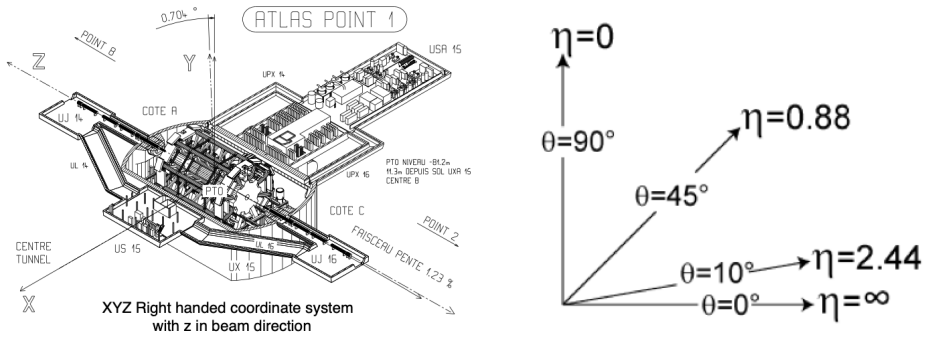

(A) (B)

FIGURE 3.5: (A) Positioning of the ATLAS coordinate system. Figure taken from [93]. (B) The relation of the pseudorapidity to θ. Figure taken from [94].

quantum numbers and consequently in their possibility to take part in specific interactions, different particles can interact in very diverse ways with the subdetectors and thus leave a variety of combined signals. Figure 3.4 shows a schematic picture of the combined signals for some Standard Model particles, where dotted lines indicate no interaction with the detector up to that point. One note of caution: contrary to the depiction, hadrons do interact with the electromagnetic calorimeter and deposit a small amount of their energy in them. With solely the information of the electromagnetic calorimeter for example, one could not distinguish between electrons and photons. However, by combining the information of the electromagnetic calorimeter with the inner detector, they are easy to separate by the mere existence of the track leading to the energy deposit in the electromagnetic calorimeter. While neutrinos do not interact with the detector in any measurable way, their participation in a process can be detected using energy and momentum conservation.

At hadron colliders the exact momentum of the interacting partons is unknown and therefore energy and momentum conservation can not be used in all three spatial dimensions. Nevertheless, since the proton beams are collided head-on, energy and momentum conservation in the plane orthogonal to the beam can be applied. Accordingly, the sum of the transverse momenta p_T or energies E_T of all particles taking part in the interaction has to be zero. In consequence the missing transverse momentum or energy, which can be calculated according to Equation 3.2, where $\vec{p}_\mathrm{T}^{\,i}$ and E_T^{i} are the momenta and energies of the measured particles, indicates if there is at least one particle that left ATLAS undetected whenever $\vec{p}_\mathrm{T}^{\,miss}$ and E_T^{miss} are not zero.

$$\vec{p}_\mathrm{T}^{\,miss} = -\sum \vec{p}_\mathrm{T}^{\,i} \qquad E_\mathrm{T}^{miss} = -\sum E_\mathrm{T}^{i} \tag{3.2a-b}$$

ATLAS uses a right-handed coordinate system with the interaction point as its origin. The x-axis points towards the centre of the LHC, the y-axis points straight up towards the surface and the z-axis is aligned with the beam pipe. A schematic drawing of this orientation can be seen in Figure 3.5a. More practically for data analysis, a spherical coordinate system is used, where the azimuthal angle ϕ is measured in the x-y-plane with respect to the positive x-axis and the polar angle θ is measured in the r-z-plane with respect to the positive z-axis, with the radial distance $r := \sqrt{x^2 + y^2}$. θ is often replaced by the pseudorapidity η which can be calculated from θ according to Equation 3.3. The advantage of η is that differences in it are Lorentz invariant

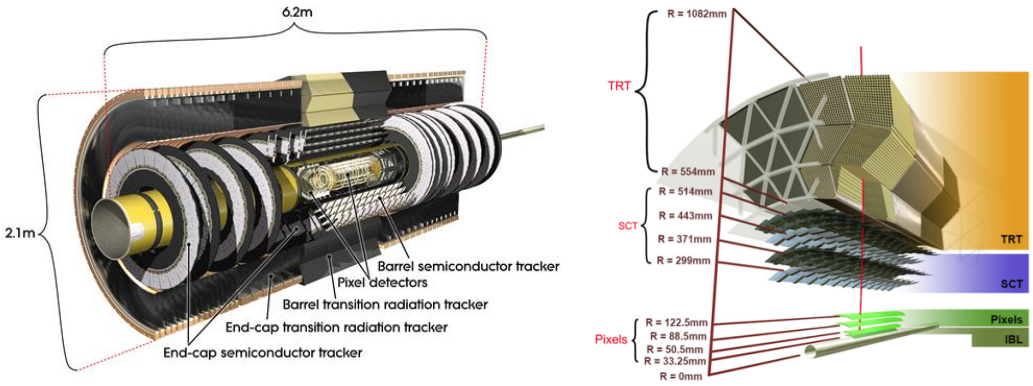

(A) (B)

FIGURE 3.6: Cut-away view of the inner detector of ATLAS including the different subsystems and the radii of the different layers. (A) taken from [96], (B) taken from [97].

under boosts along the z-axis. Figure 3.5b shows η for some exemplary values of θ.

$$\eta := -ln\left(\tan\frac{\theta}{2}\right) \tag{3.3}$$

With a bunch crossing each 25 ns, which translates to a collision frequency of 40 MHz, the amount of data produced by the ATLAS detector is not recordable on disk. For this reason ATLAS employs a two-level-trigger system that decides which events are read out and stored by previously defined selection criteria. The hardware-based Level-1 trigger (L1) reduces the rate to 100 kHz and the software-based High-level Trigger (HLT) further reduces the rate to approximately 1 kHz, which is storable [95].

3.2.1 Inner Detector

The ATLAS ID's main task is to measure the momentum of charged particles that traverse it. This is achieved by measuring the positions of a charged particle with high precision and by combining these position measurements into a trajectory. Since the ID is embedded in a magnetic field, the Lorentz force bends the trajectory of charged particles and by evaluating the curvature of the track one obtains the momentum, as well as the sign of the charge. The ID is 6.2 m long and 2.1 m in diameter, covers the $|\eta|$ range up to 2.5 and can be further divided into three types of detectors: the Pixel Detector, the Semiconductor Tracker (SCT) and the Transition Radiation Tracker (TRT). Each component works independently and they complement each other. The layout of the ID, with its components, can be seen in Figure 3.6a, Figure 3.6b shows the layered structure in the barrel region of the ID. Besides the momentum measurement, a further task of the ID is to identify primary and secondary vertices and to associate the tracks to them. Reconstructing the primary vertex, the point where the proton–proton interaction occurred, helps to clean the event from tracks that originate from pile-up collisions, and by reconstructing secondary vertices meta-stable[6] particles can be identified and studied.

[6]Particles with a lifetime long enough to travel a short distance from the interaction point but small enough to decay inside the beam pipe or ID.

Pixel Detector

The innermost sub-detector of the ID is the silicon Pixel Detector [98]. In the barrel region, it consists of four concentric layers at average radii of 33.25 mm, 50.5 mm, 88.5 mm and 122.5 mm and covers $|\eta|$ values up to 1.7. The first layer, called Insertable B-Layer (IBL [99]), was not part of the initial design of the Pixel Detector but could be added in 2014 after a narrower beam-pipe was installed. Due to its installation at a very small radius, it was able to improve the identification of vertices providing another high-precision hit improving the tracking. The typical pixel used in the IBL has a size of 50 μm $\times$ 250 μm in transverse and longitudinal direction and a thickness of 200 μm. Pixels in the other three layers have a typical size of 50 μm $\times$ 400 μm with a thickness of 250 μm. The barrel reaches a position resolution accuracy of 10 μm in ϕ and 115 μm in z. The end-cap consists of three disks on each side, perpendicular to the beam-pipe at $|z|$ values of 495 mm, 580 mm and 650 mm and covers the region $1.7 < |\eta| < 2.5$. In total, the Pixel Detector consists of $86.4 \cdot 10^6$ pixels, $73.2 \cdot 10^6$ of them in the barrel and the remaining $13.2 \cdot 10^6$ in the end caps. In addition to the precision position information, the Pixel Detector is capable of measuring the charge collected via a time-over-threshold measurement [100], which serves as a value for the energy deposit in the Pixel Detector.

Semiconductor Tracker

The ATLAS ID's second layer is the SCT [101]. The SCT is another silicon-based detector organised in four cylindrical double layers of silicon strip detectors with average radii between 299 mm and 514 mm, covering $|\eta|$ values up to 1.4 in the barrel region. The typical strip length is 126 mm with a pitch of 80 μm and the layers are mounted with a small stereo angle of 40 mrad in order to get information in the non-precision direction along the strips (z-direction). The SCT achieves a resolution of 16 μm in ϕ and 580 μm along the z-axis. The end-caps of the SCT consist of nine disks on each side covering $|\eta|$ values up to 2.5. In total, the SCT possesses $6.4 \cdot 10^6$ readout channels.

Transition Radiation Tracker

The TRT [102] is the last and outermost part of the ATLAS ID. Similar to the other two sub-detectors of the ID it consists of a barrel region and end-caps. The TRT is made of thin-walled proportional drift tubes, called straw tubes. Each tube has a diameter of 4 mm and can detect radiation produced by relativistic particles traversing the polypropylene foils around the straws. Each straw is filled with gas[7] and has a gold-plated tungsten wire with a diameter of 30 μm in its centre, acting as an anode. In the barrel region, the TRT is composed of 52,544 straw tubes located outside the SCT, covering radii from 554 mm to 1082 mm. Each straw has a length of 144 cm and is oriented parallel to the beam-pipe, covering $|\eta|$ values up to 0.7. In both end-capes 122,880 straws with a length of 37 cm, oriented radially to the beam-pipe, are used, which extend the covered $|\eta|$ range to 2.0. In the barrel, the straws are split and read out from both sides, while the straws in the end-caps are red out on one side. Each channel provides a spatial resolution of 170 μm perpendicular to the direction of the straw. Alongside the straw (z-direction in the barrel, r direction in the end-caps) no measurement can be conducted. Since the strength of the transition radiation depends on the velocity of the particle, the TRT allows for limited particle

[7] $70\%Xe, 27\%CO_2, 3\%O_2$, in leaking straws Argon was used as a substitute for the expensive Xenon.

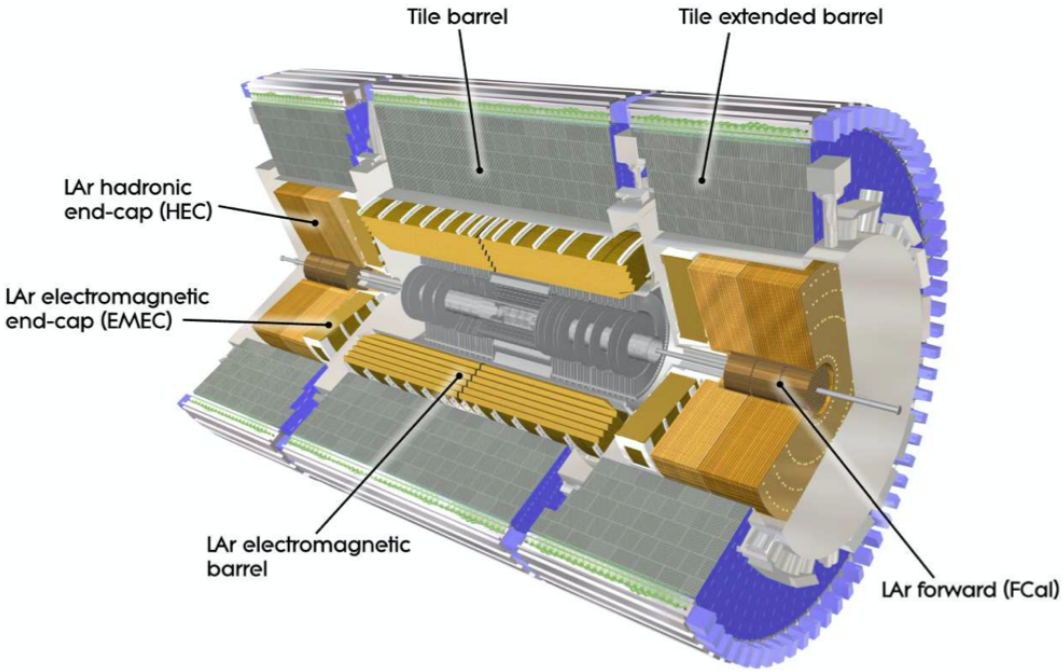

FIGURE 3.7: Schematic cut-away view of the calorimeter system of ATLAS and its positioning outside the inner detector, depicted in grey right next to the beam-pipe. Figure taken from [105].

identification and is able to distinguish between light electrons and heavy charged hadrons.

3.2.2 Calorimeters

The main goal of the ATLAS calorimeter system [103, 104] is to measure the energy a particle loses by passing through the detector. Usually, calorimeters are designed in a way that the particle deposits its entire energy in them and is stopped. ATLAS uses sampling calorimeters which are composed of passive and active materials placed in a sandwich structure. Inside of the passive material the traversing particle interacts intensively with the detector material and forms showers which are then absorbed by the active material, where the energy deposit is measured. This intensive interaction can either be achieved electromagnetically or via the strong interaction and thus form electromagnetic or hadronic showers, respectively. ATLAS uses both types of showers to measure the energy of a particle. The lighter particles, like electrons and the massless photons, are stopped in the electromagnetic calorimeter and the heavier hadrons are usually stopped in the hadronic calorimeter. Figure 3.7 shows a schematic drawing of the calorimeter system deployed in ATLAS.

Electromagnetic Calorimeter

When a highly energetic electron traverses the dense passive layers of the electromagnetic calorimeter it is subject to bremsstrahlung and therefore emits a photon. In the presence of heavy nuclei, photons with a high-enough energy undergo a pair–creation process of electron–positron pairs. The combination of these two processes leads to the formation of electromagnetic showers. The showers die out when the energy of the produced particles falls below a critical threshold at which ionisation

energy loss takes over for electrons. The total charge produced in such a showering process is proportional to the energy of the initial particle. By measuring the charge in the active material the calorimeter can thereby estimate the total energy being deposited. The radiation length resembles the distance where the energy has been reduced to $1/e$. Since ATLAS aims to measure the full energy, even for highly energetic electrons or photons, the electromagnetic calorimeter of ATLAS has a minimum thickness of 22 radiation lengths [103]. Similar to the sub-detectors of the ID the electromagnetic calorimeter consists of a barrel region covering a $|\eta|$-range up to 1.475, with a radial extension from approximately 1.4 m to 2.0 m and end-caps that extend the range to $1.375 < |\eta| < 3.2$. The passive material used is lead and the active material employed is liquid argon[8]. The layers have an accordion-shaped structure which allows for a design without holes in ϕ-direction. The resolution varies with η and reaches a granularity of $\Delta\eta \times \Delta\phi = 0.025 \times 0.0245$ in the barrel and $\Delta\eta \times \Delta\phi = 0.1 \times 0.1$ in the end-caps. Since the particles reaching the electromagnetic calorimeter have already traversed the inner detector, the cryostat and the solenoid magnet and lost some energy doing so, a presampler was installed covering $|\eta| < 1.8$ to aid in the correction process for this energy loss.

Hadronic Calorimeter

Analogous to electrons, highly-energetic hadrons create particle showers when they traverse dense material. The processes creating these showers however are different and caused by the strong interaction. While the showering mechanism is more complicated than the one for electromagnetic showers, the principle is similar. The hadronic shower typically has a longer penetration depth though. Hence, an additional and more dense hadronic calorimeter is used by ATLAS. Similar to the electromagnetic shower, the depth of a hadronic shower is characterised by the hadronic interaction length. The maximum thickness of the hadronic calorimeter is eleven times the interaction length, which is enough to prevent a punch-through into the Muon Spectrometer. The barrel region consists of a barrel segment covering $|\eta| < 1.0$ and an extended barrel with $0.8 < |\eta| < 1.7$. The active layers are made of scintillating tiles[9] and the passive layers consist of iron. The granularity of the barrel region is $\Delta\eta \times \Delta\phi = 0.1 \times 0.1$ [104]. In the end-caps the hadronic calorimeter achieves a granularity of $\Delta\eta \times \Delta\phi = 0.2 \times 0.2$ with liquid argon being used as active and lead as passive material. In order to cover an additional $|\eta|$ range of $3.1 < |\eta| < 4.9$ ATLAS additionally employs a forward calorimeter using liquid argon as active material. The first layer of passive material is made of copper and the following two layers consist of tungsten. With a radial extension of up to 4.2 m, the tile calorimeter can also be used for time-of-flight measurements and calculations of the velocity of the traversing particle.

3.2.3 Muon Spectrometer

The outermost component of ATLAS is the Muon Spectrometer, which serves two tasks: firstly, providing fast signals of traversing muons[10] that the trigger system can use and secondly making a high precision measurement of the momentum of traversing particles. Similar to the ID the MS, therefore, is immersed in a strong magnetic field provided by eight toroid magnet coils and two end cap toroids with

[8] Therefore, the electromagnetic is often replaced with "Liquid Argon" or just LAr.

[9] It is therefore often referred to as tile calorimeter.

[10] The only detectable Standard Model particle reaching the MS.

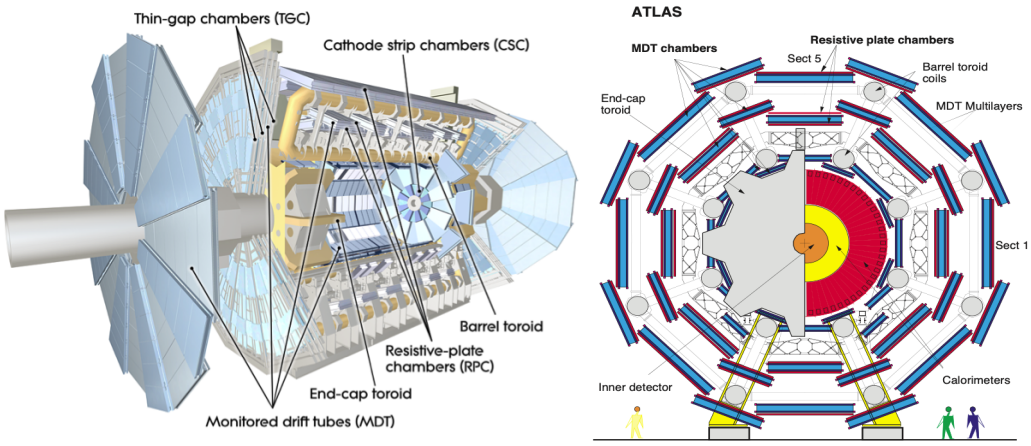

(A) (B)

FIGURE 3.8: (A) shows a shematic cut-away drawing of the ATLAS Muon Spectrometer including the subsystems. Figure taken from [106]. (B) shows a schematic representation of of ATLAS in the x-y projection with indications for the positions of the inner detector and the calorimeters. Monitored Drift Tubes are drawn in blue and Resistive Plate Chambers in Red. Figure taken from [107].

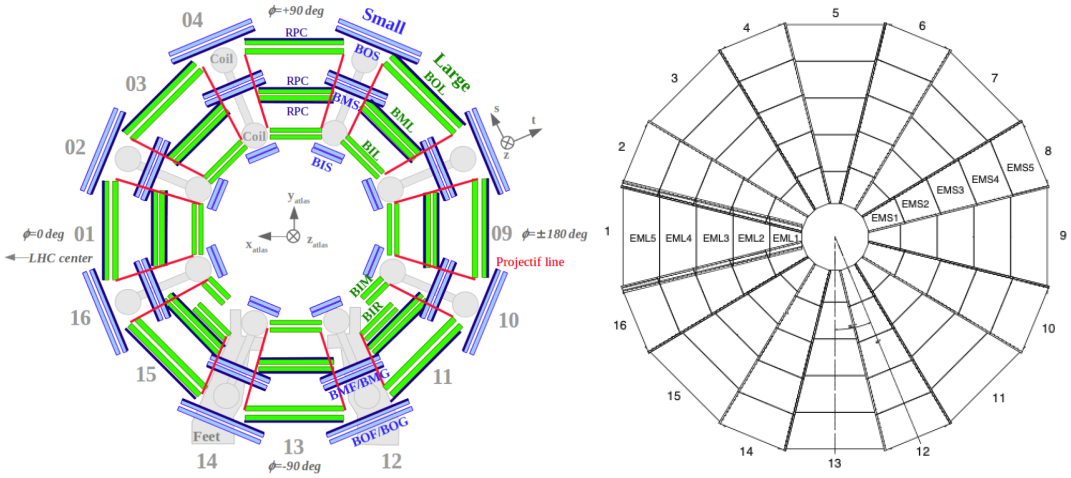

(A) Barrel region (B) End-cap region

FIGURE 3.9: Schematic drawing of the ATLAS MS depicting the naming and numbering scheme. (A) shows the barrel region. Large detector chambers are shown in green, small ones in light blue, RPC modules in dark blue, the toroid magnets and the feet in grey. Figure taken from [108]. (B) shows a sketch of the middle layer of the end-cap system. Figure taken from [109].

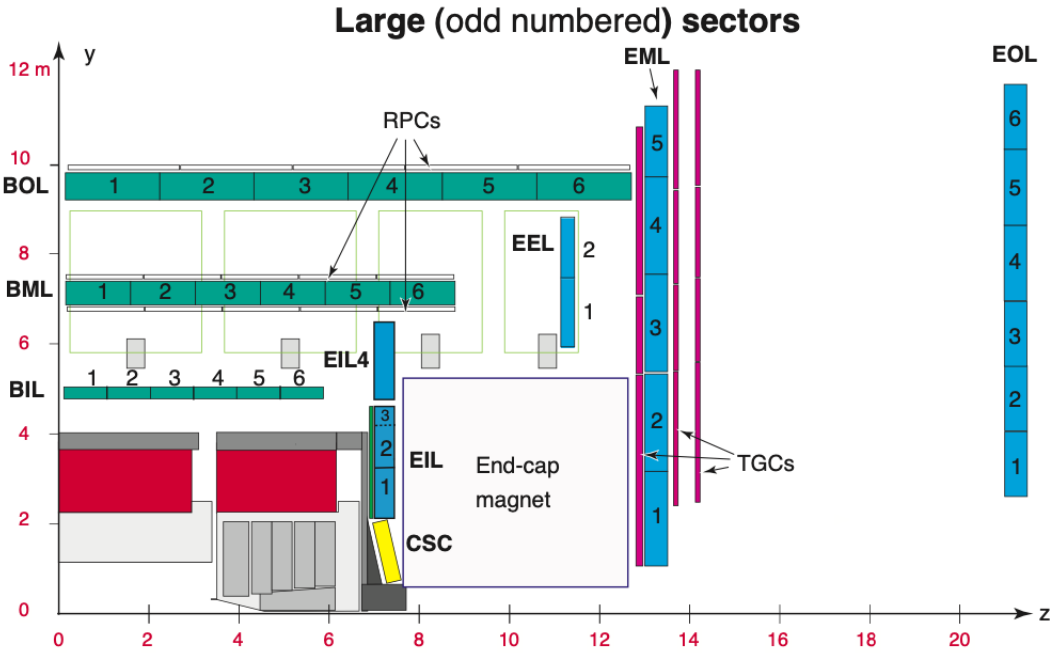

FIGURE 3.10: Schematic view of a part of the ATLAS Muon Spectrometer depicting the naming and numbering scheme for the large chambers. Figure taken from [109].

eight coils each. Just as the other detector layers, the MS is separated into a barrel region and end-caps. A schematic cut-away picture of the ATLAS MS and its subsystems can be seen in Figure 3.8a, Figure 3.8b shows a schematic representation of the cross-section view along the z-direction. In the barrel region, the detector chambers are arranged into three cylindrical layers around the beam-pipe called Barrel Inner (BI), Barrel Middle (BM) and Barrel Outer (BO). Each layer is further divided into 16 sectors in the ϕ-plane, the sectors being counted clockwise beginning with the sector on the positive x-axis. Sectors with an even number host large chambers, which are located between two coils of the toroid magnet (BIL,BML,BOL) and sectors with odd numbers host small chambers, which are located under, between and above one toroid coil (BIS,BMS,BOS). Since the feet of ATLAS are located in sectors 12 and 14, the chambers in and around those sectors may differ in size and therefore have different acronyms. A schematic view of the placement of the chambers in the sectors can be seen in Figure 3.9a. The end-cap system possesses four discs on each side perpendicular to the beam axis, called End-cap Inner (EI), End-cap Extra (EE), End-cap Middle (EM) and End-cap Outer (EO). The end-cap system uses the same ϕ sectors as the barrel, thus is composed of large (EIL,EEL,EML,EOL) and small (EIS,EES,EMS,EOS) chambers as well. Additionally, the disks are divided into sectors along the radius of the disk. Figure 3.9b shows the location of the chambers within the disk and Figure 3.10 shows the placement of the different disks of the end-cap system along the z-axis and the layers of the barrel region for a large section along the y-axis. This acts as a representation of the radii from the interaction point. Employing this setup the ATLAS MS can detect particles with $|\eta| < 2.7$ [110].

Since the MS has two separate purposes, different detector elements are used, specialised for one of the tasks. There are four different detector types in service: Monitored Drift Tubes (MDT's), Resistive Plate Chambers (RPC's), Thin Gap Chambers

(TGC's) and Cathode Strip Chambers (CSC's) [111]. The precision measurement of the momentum is mainly done by MDT's. Since the work at hand uses data from MDT's and RPC's, they will be explained in more detail in a separate subsection. For the $|\eta| > 2$ region there is a high counting rate expected in ATLAS. Since MDT's are not well suited for measurements under those conditions, in this region CSC's are used to perform the precision tracking measurement. CSC's are multi-wire proportional chambers, where a particle crossing the chamber ionises a gas and this ionisation is then measured. They have a wire spacing of 2.54 mm and the same distance between the wire and the cathode. As their ionising gas the CSC's use a Ar-CO_2-CF_4-mixture. The CSC's reach a spatial resolution of 60 μm in the bending direction and due to the wider strips only 5 mm in the non-bending direction, as well as a timing resolution of 3.6 ns, which can not be used in this work. [111].

The triggering is performed by separate detector systems in the barrel and in the end-caps. As shown in Figure 3.10 RPCs are installed in the barrel region, where they perform the triggering task, while TGCs are used for the triggering in the end-caps. Similar to CSCs TGCs are multi-wire proportional chambers but due to their small wire-to-cathode distance of 1.4 mm, they have a very fast signal. As ionising gas they use a CO_2-n-pentane mixture and they achieve a timing resolution of 4 ns. Even though tracking is not their priority, they also do provide information about the trajectory of the traversing particle with a resolution of less than 6 mm in the radius and less than 7 mm in ϕ [75].

Monitored Drift Tubes

The fundamental structure of MDT's is similar to multi-wire proportional chambers. They consist of aluminium drift tubes pressurised to 3 bar with a diameter of 29.970 mm and a length of up to 6.5 m. In the centre of the tube, which is filled with gas consisting of 97% Ar and 7% CO_2, there is a gold-plated tungsten-rhenium wire with a diameter of 50 μm, which acts as an anode and is held in position relative to the tube with a precision of < 10 μm [75]. When a muon crosses the tube it ionises the gas and the free charges drift towards the anode. The distance of the muon passing the tube to the wire determines the drift time which can be as high as 700 ns. The radius of the drift circle R_{min}, which can be seen in Figure 3.11a, is therefore determined by the arrival of the charges from the part of the track closest to the centre.

In the ATLAS MS, there are three layers of MDT chambers installed. Each chamber is build of two multilayers of drift tubes, which are separated by a mechanical spacer as Figure 3.8b shows. Each multilayer consists of three or four layers of MDT's, which are shifted by one radius between adjoining layers. Depending on the specific chamber, the distance between the multilayers ranges from 6.5 mm to 317 mm. Since the performance needs to be higher when the chamber is closer to the interaction point, the chambers of the inner layer are composed of multilayers with 4 layers of MDTs each. The middle and outer layers host chambers with 3 layers in each multilayer. The combination of the layers into chambers improves the resolution from approximately 80 μm per tube to approximately 50 μm per multilayer and to approximately 35 μm per chamber. [112]

As shown in Figure 3.12 the readout of the signal is done for up to 24 drift tubes at once by a mezzanine card. Each chamber contains up to 18 mezzanine cards, which

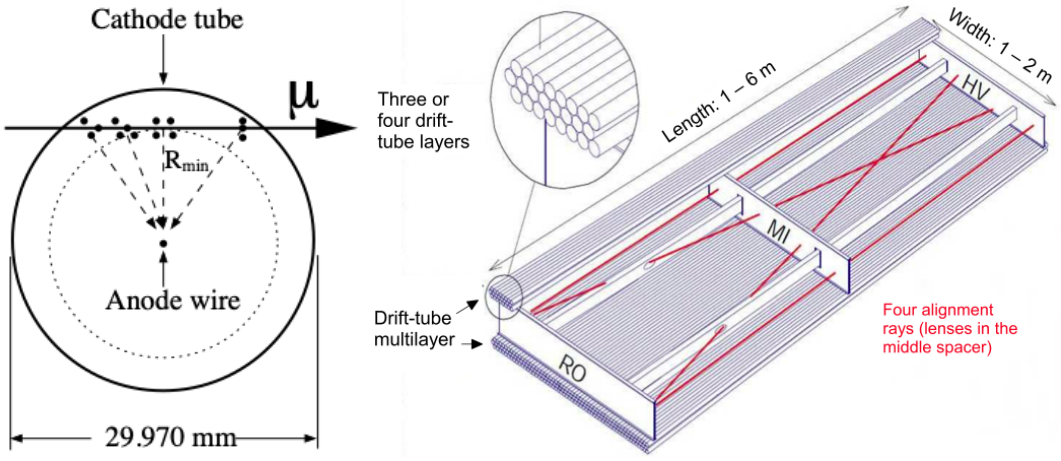

(A) (B)

FIGURE 3.11: (A) shows the cross-section of a tube with the ionisation caused by a traversing muon and the resulting R_{min}. (B) shows the layout of a MDT chamber composed of two multilayers and a spacer. Figures taken from [75].

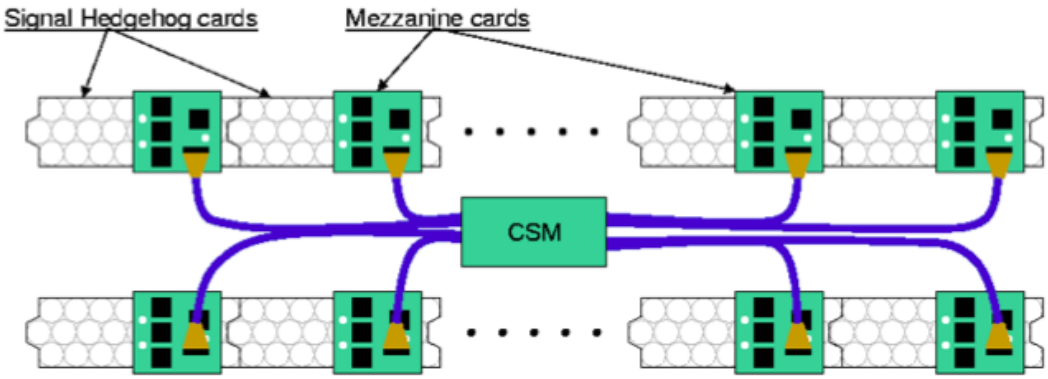

FIGURE 3.12: The readout electronics for a MDT chamber in ATLAS. Figure taken from [113].

are connected to a local processor, the Chamber Service Module. In total, there are 1,171 chambers with a total of 354,240 tubes installed in ATLAS [111].

Resistive Plate Chambers

The three RPC layers are installed in the barrel region of the MS and as displayed in Figures 3.10 and 3.9a two of them are installed on both sides of the MDT chambers in the middle layer (BM). The last layer is attached to the MDT chambers in the outer layer (BO). For even sectors, this third layer is installed on the inside of the MDT chamber and for odd sectors, it is installed on the outside. One RPC chamber consists of two detection layers with orthogonally oriented strips measuring the η and ϕ position independently. Inside of the chamber, a gas mixture of 94.7 % $C_2H_2F_4$, 5 % $Iso - C_4H_{10}$ and 0.3 % SF_6 and a voltage gradient of about 4.9 kV/mm is placed in the 2 mm gap between two rectangular resistive phenolic-melanimic plastic laminate plates. Each chamber consists of two independent gas gaps. A muon traversing through the chamber causes an avalanche within the gas gap, which is then read out

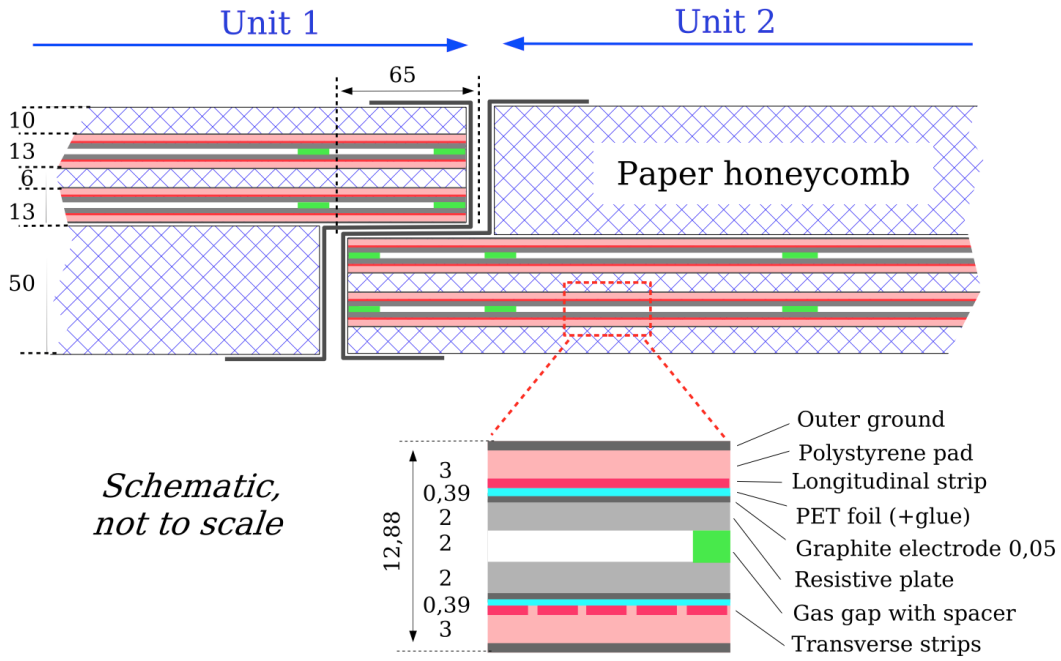

FIGURE 3.13: Cross-section of the overlap region of a RPC module, showing how two gas gap segments are combined into one module. Measures given in mm. Figure taken from [75].

through metallic strips in η and ϕ direction. These η- or ϕ-strips are 2.3 to 3.5 cm wide and up to 3.2 m long. If the chamber is longer than that, it consists of two gas gap segments that are attached to each other as can be seen in Figure 3.13. Each strip has a spatial resolution of 10 mm and a nominal timing resolution of 1.5 ns. Similar to the ATLAS triggering system the internal logic of the RPC system uses a 320 MHz clock, while proton–proton collisions occur at a frequency of 40 MHz or 25 ns. Therefore each bunch crossing is divided into eight equidistant ticks each 3.125 ns, where the readout occurs. This intrinsic granularity of the readout system for RPCs is visible in the RPC timing measurement and has to be taken into consideration during track reconstruction and calibrations. In the ATLAS MS, there are about 3600 gas volumes and 370,000 individual readout strips combined into 606 chambers [114, 115].

Chapter 4

Charged Stable Massive Particles at ATLAS

Charged stable massive particles are predicted by a variety of BSM theories. In this context, stable refers to a lifetime, which is long enough for the particle to traverse the detector before its decay. Therefore, these particles are able to interact with the detector and leave signatures similar to those of muons. As SMPs are predicted with much higher masses than muons, their velocity is significantly lower than the speed of light, differentiating their signature from Standard Model muons. Hence, searches for SMPs offer a model-independent way of looking for New Physics with little to no Standard Model background. This chapter will give a short insight into the production of charged stable massive particles, followed by an explanation of the observables used in searches for them, as well as a brief look into their reconstruction.

4.1 Production

The exact production mechanism depends on the specific model used to predict the SMP, but since most of them include a conserved quantity of some sort, they are mostly predicted to be directly produced in pairs. Feynman diagrams for the production of staus and charginos, as they are predicted by the MSSM to be candidates for charged stable massive particles, on tree level are shown in Figure 4.1. A charged stable massive particle could also be the result of the decay of an even heavier supersymmetric particle. This production mechanism has typically little impact on the effective signature in the detector due to the combination of two factors. Firstly, the heavier the primary particle, the lower is its cross–section for production and secondly, when the mass of the primary particle is close to the mass of the charged stable massive particle, the available phase space for the decay becomes small and thus suppresses the decay.

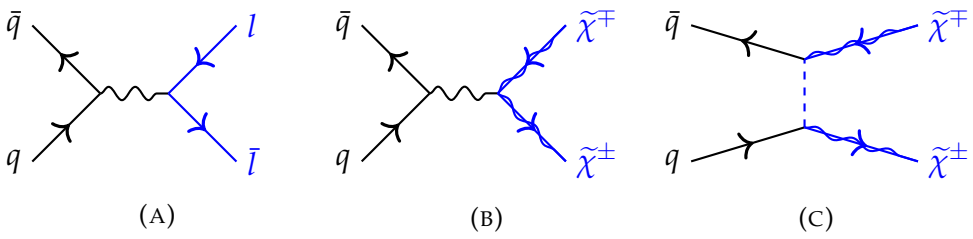

(A) (B) (C)

FIGURE 4.1: Feynman diagram for the production of sleptons via quark–quark-fusion in (A) and for the production of charginos via quarl–quark-fusion in (B) and quark–quark-scattering in (C).

While a single production channel for SMPs is theoretically possible, the production cross–section is proportional to the decay width in this case and therefore proportional to the inverse of the lifetime. In order to achieve lifetimes long enough to be considered stable, the cross–section becomes negligible. Furthermore, it is possible for a charged stable massive particle to be produced in combination with an uncharged stable massive particle. This may occur when they have almost the same mass and the neutral particle is the lightest particle with a new conserved quantum number. In the MSSM, this could be the case for the combination of the lightest neutralino and chargino. As a result, the neutral particle would most likely not be detectable, leaving only a missing transverse energy E_{T}^{miss} as its signature [67].

4.2 Observables

Charged stable massive particles offer an appealing approach for a search for BSM theories. As they are electrically charged, they interact with the detector material and therefore leave a signal that can be measured. The high predicted mass leads to the expectation of large ionisation energy losses in the ID and a velocity significantly lower than the speed of light ($\beta\gamma \leq 0.9$ [116]) that can be used for identification. Thus, the difference between the expected time of arrival[1] and the timing information of the interaction with the detector can be a useful measure. Since no Standard Model process leads to similar signatures, the background for an analysis looking for charged stable massive particles is dominated by detector mismeasurements.

4.2.1 Ionisation Energy Loss

A charged particle traversing the detector interacts with the electrons of the detector material and by exciting or ionising them, the traversing particle deposits some of its energy in the detector material. This energy loss is referred to as ionisation energy loss or $\langle \frac{dE}{dx} \rangle$. The ID deployed in ATLAS is capable of measuring $\langle \frac{dE}{dx} \rangle$ with its pixel detector and TRT, while the SCT does not provide a $\langle \frac{dE}{dx} \rangle$ measurement. The mean of the energy loss per travelled distance of a particle with energy E, charge z and velocity v can be calculated using the Bethe–Bloch–formula shown in Equation 4.1 [117, 118].

$$\left\langle \frac{dE}{dx} \right\rangle = \frac{4\pi e^4 z^2 n}{m_e c^2 \beta^2} \left(\frac{1}{2} ln \left(\frac{2 m_e c^2 \beta^2 \gamma^2 T_{max}}{I_e} \right) - \beta^2 - \frac{\delta}{2} \right) \tag{4.1}$$

The electron density of the material is denoted with n, while m_e and e symbolise the rest-mass and the charge of electrons, respectively. The mean ionisation potential is described by I_e and δ is a material constant accounting for density effects. The speed of light is denoted with c. As can be seen in Equation 4.2a, β results from the ratio of the velocity v and the speed of light, while the Lorentz factor γ is defined in Equation 4.2b. T_{max} denotes the maximum energy transfer a single electron can receive. If the traversing particle is much heavier than the electron, T_{max} is given by Equation 4.2c.

[1] Particles traversing ATLAS are expected to travel at the speed of light.

$$\beta := \frac{v}{c} \qquad \gamma := \frac{1}{\sqrt{1-\beta^2}} \qquad T_{max} = 2m_e c^2 \beta^2 \gamma^2 \tag{4.2a-c}$$

Since Equation 4.1 is only dependent on variables specific to the material and the velocity of the traversing particle, the $\langle \frac{dE}{dx} \rangle$ measurement serves as a way to calculate the velocity of the traversing particle. The pixel detector gives one $\langle \frac{dE}{dx} \rangle$ measurement per layer and thus four individual measurements of the ionisation energy. By averaging them, one can get the Most Probable Value (MPV). Since it is known that $\langle \frac{dE}{dx} \rangle$ is Landau distributed, the MPV differs from the mean of Equation 4.1. Therefore, an empiric Bethe–Bloch–formula is used to get a relation between the MPV of $\langle \frac{dE}{dx} \rangle$ and the velocity. This empiric formula can be seen in Equation 4.3.

$$\text{MPV}_{\frac{dE}{dx}} = \frac{A}{(\beta\gamma)^C} + B \tag{4.3}$$

A, B and C are calibration constants determined by low-momentum pions, kaons and protons reconstructed by ATLAS in low-luminosity runs [116] and as shown in Equations 4.2a and 4.2b, $\beta\gamma$ is only dependent on the velocity of the traversing particle and therefore serves as a measure for it. In order the reduce the impact of the tales of the Landau distribution and to ensure that the mean of the $\langle \frac{dE}{dx} \rangle$ measurements gives a good estimate for the $\text{MPV}_{\frac{dE}{dx}}$, it is calculated disregarding the highest $\langle \frac{dE}{dx} \rangle$ measurement. In combination with the measured momentum, p, the ID is even able to perform a calculation of the rest-mass m_0 of the traversing particle by using Equation 4.4 [119].

$$m_0 = \frac{p}{\beta\gamma} \tag{4.4}$$

4.2.2 Time-of-Flight Measurement

Another independent approach to measure the velocity, or β, is to evaluate the time it took for the particle to travel from the interaction point to a detector element at distance d. This approach is referred to as Time-of-Flight (ToF) measurement. Particles with the same energy but different masses also differ in their β, which means that heavier particles have a smaller β and therefore need more time to reach a specific element of the detector. Thus, a variable t_0 is introduced, given in Equation 4.5a, which measures the difference between the actual time of flight ToF_a and the time of flight of a particle traversing the detector at the speed of light ($\beta = 1$) ToF_c. As can be seen in Equation 4.5b, the t_0 value can be used to calculate β. By using additional information about the momentum p of the traversing particle, its rest-mass m_0 can then be calculated according to Equation 4.4.

$$t_0 = \text{ToF}_a - \text{ToF}_c = \text{ToF}_a - \frac{d}{c} \qquad \beta = \frac{d}{\text{ToF}_a} \cdot \frac{1}{c} = \frac{d}{d + t_0 \cdot c} \tag{4.5a-b}$$

Due to their large distance from the interaction point and the available timing information, the tile calorimeter as well as the MDT tubes and RPC strips of the MS are suitable detector elements to perform a ToF, and thereby a measurement of β.

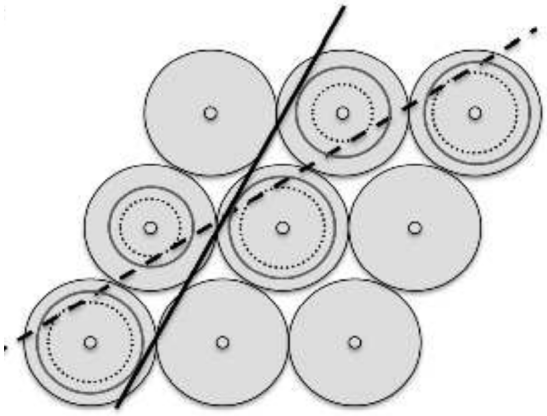

FIGURE 4.2: Cross section of a MDT multilayer with a wrongly reconstructed track and drift circles in solid black and correct reconstruction in dashed and dotted black, respectively. Figure taken from [124].

4.3 Muon Reconstruction

In the Standard Model, only muons are electrically charged and able to escape the calorimeters and thus reach the MS. However, charged stable massive particles predicted by BSM theories could also reach the MS and similarly to muons, leave a signature in it. A notable difference is the high predicted mass and therefore lower velocity. Particles with a suitable signature for charge stable massive particles are therefore often referred to as slow muons at ATLAS.
The purpose of ATLAS is to detect and investigate as many particles emerging from collisions as possible. To achieve this, the computational reconstruction process of ATLAS uses a variety of algorithms trying to combine the information of the subdetectors to the trajectory and properties of the particle causing the signal. Particle-detector interactions, called hits, in the Muon Spectrometer are most likely caused by muons and thus are used by several algorithms aiming to reconstruct muons.

There are some algorithms starting with the reconstruction of muons in the ID [120], or the calorimeters [120] but most of them start by fitting a track to the Muon Spectrometer hits [121, 122]. The tracks are then extrapolated towards the interaction point and outer detector layers to assign the hits in the other detector systems to the muon as well. In order to achieve the best possible accuracy, the results of the different muon reconstructions are then combined and, depending on their reconstruction quality, e.g. number of hits and χ^2 of the track fit, assigned a loose, medium or tight quality label [123].

Since only muons usually reach the MS and they are produced with $\beta \approx 1$, most of the reconstruction algorithms for muons decrease significantly in their reconstruction efficiency for simulated particles leaving muon like tracks with smaller β. This has two main reasons. On the one hand, hits that are delayed too much might be associated with the wrong bunch crossing, which worsens the track-fitting process or even outright prevents it. On the other hand, due to their late arrival in the MDT tubes, the drift radii appear larger than usual, which leads to wrongly fitted tracks as can be seen in Figure 4.2.

This creates the problem that charged stable massive particles with a high-enough mass would simply not be reconstructed in ATLAS with decent efficiency and could therefore not be analysed. To resolve this issue, a new reconstruction algorithm called MUGIRLLOWBETA [125, 126] was introduced, applying a number of different techniques in contrast to the other muon reconstruction algorithms:

- By additionally considering the next bunch crossing, hits and especially trigger hits are recovered and used for reconstruction.
- Due to its close proximity to the interaction point, the ToF measured in the ID does not differ much for particles with a small β and particles propagating with at speed of light. Thus, measurements in the ID are less likely to be assigned to the wrong bunch crossing. Consequently, the reconstruction starts in the ID and extrapolates to the outer detector layers, where additional hits can be assigned with high efficiency.
- Instead of assuming $\beta \approx 1$, MUGIRLLOWBETA estimates β from the hit timing in the RPC strips and thus prevents the misidentification of the slow particle as a muon.
- β is treated as a free parameter when the MDT hits are fitted with a track, which allows for variable drift radii. The track with the best fitting result is then chosen.

As can be seen in Figure 4.3, MUGIRLLOWBETA is able to extend the range in which slow muons can be reconstructed with high efficiency greatly into areas with smaller β.

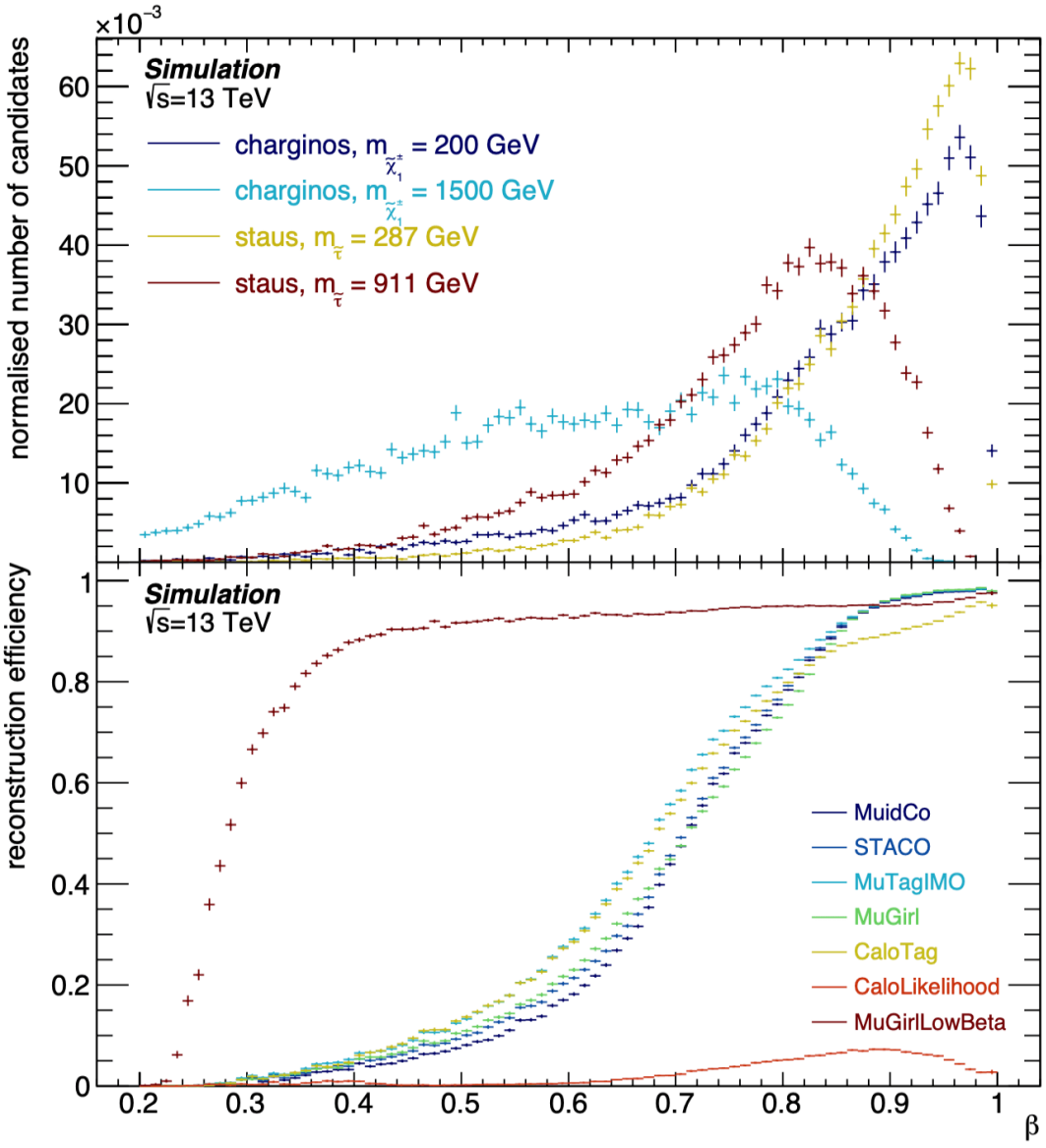

FIGURE 4.3: The top half shows the β distribution for pair-produced stable charginos and staus of various mass. The bottom half shows the reconstruction efficiency of different ATLAS muon reconstruction algorithms as a function of β. Algorithms without significant contribution were left out. Figure taken from [127].

Chapter 5

Calibration of the Timing Measurement of the ATLAS Muon Spectrometer

As already stated in the previous chapters, searches for charged stable massive particles offer a model-independent approach to a search for BSM physics with little to no Standard Model background. Thus, detector mismeasurements are the leading background for such analyses. A good understanding of the detector systems and their β resolution is therefore very important and by improving this β resolution, the chance detecting a charged stable massive particle can be increased or stronger exclusion limits can be obtained. The calibration of the $\langle \frac{dE}{dx} \rangle$ measurement can be adopted from [116], but no other search in ATLAS relies on a β measurement via a ToF measurement in the tile calorimeter or Muon Spectrometer and thus a calibration strategy for the ToF measurement has to be developed. A timing calibration of the ToF and according β measurement of the tile calorimeter can be found in Reference [128]. The work at hand focusses on the timing calibration of the measurement in the ATLAS Muon Spectrometer, which shall be described in this chapter.

The timing information of a hit in a single element of the Muon Spectrometer is swayed by several influences, which is the reason why different calibration steps are needed. Each calibration step tries to get rid of an effect distorting the timing measurement. Since muons are charged and reach the MS, they can be detected by it and used as a probe for such biases in the timing measurement. Due to their low mass, muons above a certain energy threshold traverse the detector with almost the speed of light and thus have $\beta = 1$. Therefore, they should be measured with $t_0 = 0$ ns. Due to the fact that a detector performs measurements with an uncertainty: instead of $t_0 = 0$ ns for each muon, a Gaussian distribution with its mean at $\bar{t}_0 = 0$ ns is expected as the result of the ToF measurement of several muons.

The general calibration strategy is therefore to analyse t_0 distributions for different dependencies and then apply a Gaussian fit to them. The mean of the fit can then be used as a correction constant for the specific dependency and the t_0 value of each hit can be calibrated step by step according to Equation 5.1. Hereby, t_0^{in} is the uncalibrated t_0 value of the hit, t_0^{corr} is the correction constant of a specific calibration step and t_0^{out} is the calibrated t_0 of the specific hit.

$$t_0^{out} = t_0^{in} - \sum_{calibrations} t_0^{corr} \tag{5.1}$$

5.1 Data and Event Selection

This calibration uses the data recorded by ATLAS in the entire Run–2, which amounts to an integrated luminosity of $\mathcal{L}_{GooodforPhysics} = 139$ fb^{-1}, with an uncertainty of 1.7% [129]. During the data-taking of Run–2, collisions occurred every 25 ns and the ATLAS trigger system allowed for a read-out frequency of approximately 1 kHz. Reconstruction algorithms are then applied on the raw detector data to form a dataset called Analysis Object Data (xAOD), which includes the reconstructed objects and their properties. The xAOD data-set for Run–2 is on the scale of several petabytes and thus too large to perform analyses in reasonable amounts of time. However, most of the analyses do not need the entire information stored in the xAOD format, which is why ATLAS employs a derivation framework [130] building specialised data-sets called Derived xAOD (DAOD). By means of pre-set criteria, a derivation might neglect entire events (skimming), remove objects (thinning) or omit specific variables (slimming) and thus reduce the Run–2 data-set to a manageable size. Searches for charged stable massive particles, as well as this work, use a derivation called SUSY6, which requires events to have fired an E_{T}^{miss} or muon trigger. While events added by the E_{T}^{miss} trigger are required in searches for stable massive particles, they are not useful for this calibration. Consequently, additional selection criteria on the particles reconstructed by MUGIRLLOWBETA are applied.

- Each event is required to have at least one muon with the quality medium or higher.
- Muons must have an $|\eta| < 2.5$ and a $p_{\mathrm{T}} > 25$ GeV, which is high enough to safely assume $\beta \approx 1$.
- Only muons that come from the primary vertex are considered.
- The entire information for muons must be available. Therefore, links between the different representations of the muons must be valid.

In ATLAS there is a clear decay signature for the decay of the Z^0 boson into a muon–anti-muon pair ($Z^0 \rightarrow \mu\mu$). As it might be helpful to be able to identify muons emerging from a $Z^0 \rightarrow \mu\mu$ decay, muons satisfying the following criteria are additionally flagged as possible candidates of muons emerging from a Z^0 decay.

- The event needs to have at least two muons fulfilling the previously stated criteria.
- There must be a combination of two muons, in which the invariant mass of the muon pair $m_{\mu\mu}$ is close to the mass of the Z^0 boson m_Z.
  In particular $|m_{\mu\mu} - m_Z| < 10$ GeV with $m_Z = 91.1876$ GeV.
- Since the Z^0 boson decays into a pair of a muon and an anti-muon, the two candidates must be of opposite charge.

5.2 Uncalibrated Distributions

Even though the detector actually measures t_0, the information is replaced by the ToF calculated from t_0 and the known distance d of the detector element from the interaction point, $d = \sqrt{x^2 + y^2 + z^2}$, in the reconstruction step. Figure 5.1 shows these ToF and d distributions for MDTs on the left-hand side and RPCs on the right-hand side. The three peaks in the MDT distribution can be explained by the different

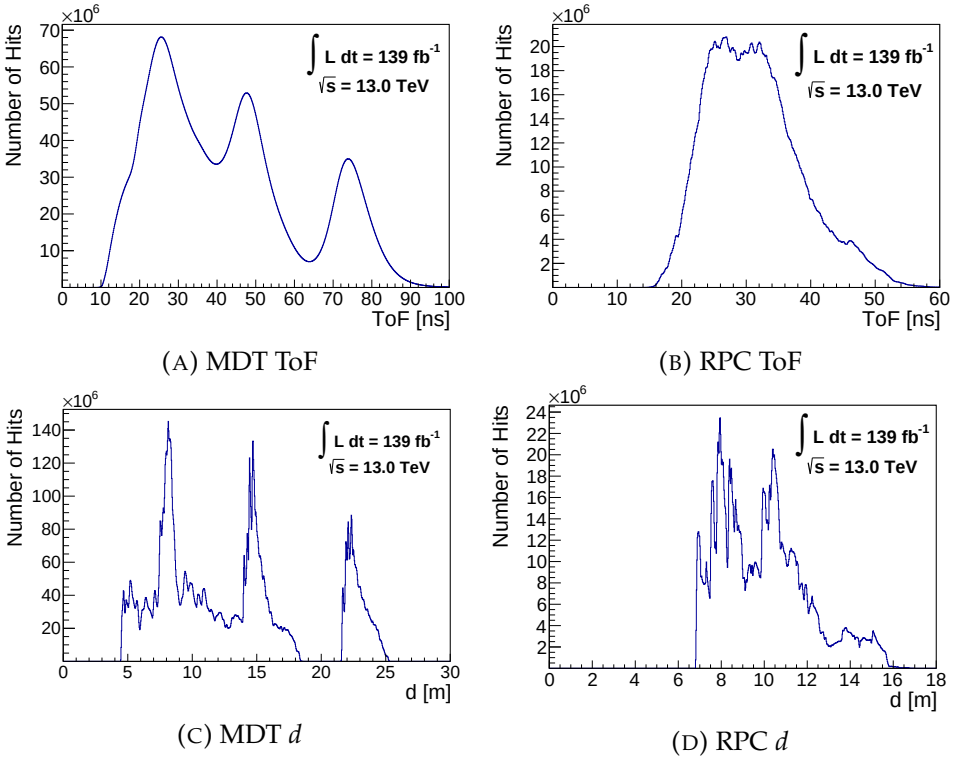

(A) MDT ToF

(B) RPC ToF

(C) MDT d

(D) RPC d

FIGURE 5.1: ToF and d distributions of the hits for MDT tubes on the left-hand side and RPC strips on the right-hand side. The upper half shows the ToF distributions and the lower half the d distributions. For a particle traversing the detector at the speed of light, the x-axes correspond to each other.

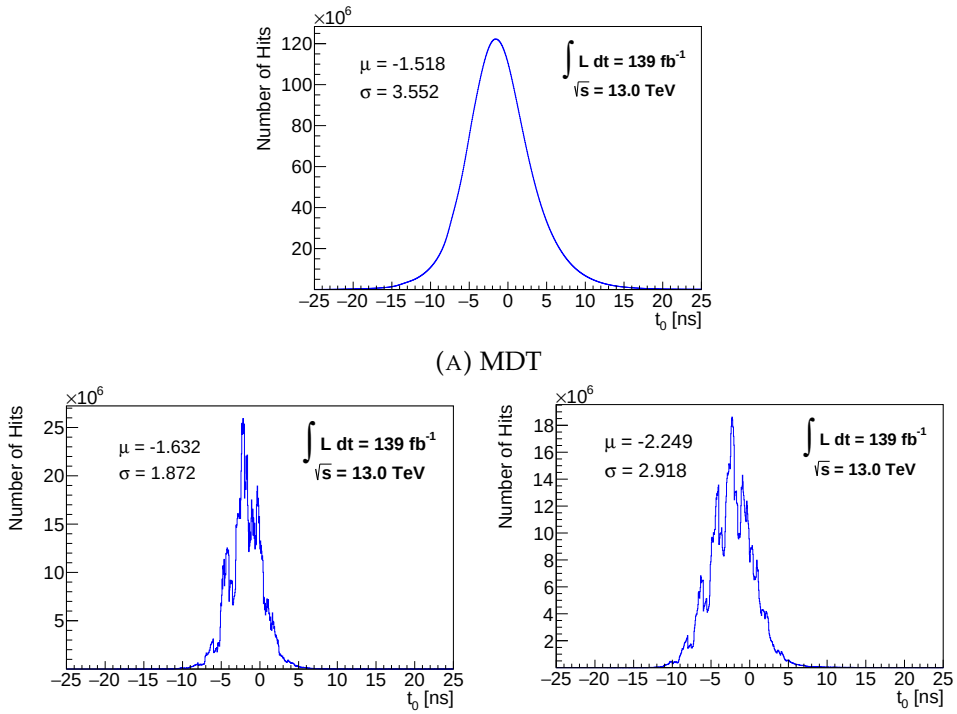

(A) MDT

(B) RPC η-strips

(C) RPC ϕ-strips

FIGURE 5.2: Uncalibrated t_0 distributions for MDT tubes in (A) and RPC η- and ϕ-stripes in (B) and (C), respectively. The spiky structure for RPCs occurs due to the readout granularity. In addition, the mean and standard deviation of a Gaussian fit with reduced fitting window of mean $\pm$ RMS are given.

detector layers. The first peak includes the layers of the barrel region and the EI of the end-cap system. The second peak results from the EM and the third from the EO. Since there are no RPCs in the end-caps, the distance from the interaction point to the detector element, and accordingly the ToF, has a lower upper bound and the peak structure of the MDT distribution can not be observed. The readout granularity mentioned in Section 3.2.3 leads to the less smooth nature of the ToF distribution for the RPCs.

The t_0 values can be calculated by reverse engineering the ToF calculation following Equation 4.5a, which leads to the uncalibrated t_0 distributions for MDT tubes and RPCs, divided into η- and ϕ-strips, depicted in Figure 5.2. The effect of the readout granularity with 3.125 ns can be seen very clearly in Figures 5.2b and 5.2c. To account for the position of the hit within the strip, a calculated propagation time is subtracted, which leads to distributions of the t_0 values around peaks determined by the readout granularity. RPC η- and ϕ-strips possess individual readout electronics and thus their t_0 distributions may differ. This difference can easily be seen by comparing Figure 5.2b and Figure 5.2c. Regarding the RPC ϕ-strips, the mean is further shifted from $\bar{t}_0 = 0$ ns and the width is significantly bigger than for RPC η-strips. It is therefore useful to treat RPC η- and ϕ-strips as separate detector systems for the calibration steps in this chapter. Even with this spiky nature, the general shape of the t_0 distributions resembles the expected Gaussian shape. The distributions can thus be fitted with a Gaussian defined in Equation 5.2.

$$f(x) = A \cdot e^{\frac{(x-\mu)^2}{2\sigma^2}} \tag{5.2}$$

A resembles the height of the function's peak and can mostly be ignored in this work, μ gives the position of the peak on the x-axis and also indicates the mean of the function. The standard deviation σ controls the width of the function and is therefore an important measure of the resolution of the fitted distribution. The mean $\bar{t}_0$ and the resolution σ quoted in Figure 5.2, and similar figures in this chapter, correspond to μ and σ of Equation 5.2, respectively.

While the shapes of the distributions depicted in Figure 5.2 comply with the expected Gaussian shape in general, their centre is clearly not at $\bar{t}_0 = 0$ ns. The aim of this calibration is to correctly centre the t_0 distribution for each detector system at $\bar{t}_0 = 0$ ns and to make them as narrow as possible. To achieve this, the following sections will look at different dependencies of the t_0 measurement and introduce calibration steps to account for them. Since the calibrations are considered to be independent of each other, the final calibrated t_0 value for every hit can be calculated as introduced in Equation 5.1.

As the ToF measurement aims at identifying traversing charged stable massive particles by their smaller β, it is useful to take a look at how β can be calculated from the t_0 measurement. Firstly, a traversing particle interacts with several detector elements and thus leads to several individual t_0 measurements. Since different detector elements might differ in their accuracy, it is beneficial to determine the β of the traversing particle as a weighted average of those measurements. Additionally, as stated in Equation 4.5b: $\beta_i \propto t_{0,i}^{-1}$ and thus it is easier to take the uncertainty $\sigma_{t_0,i}$ of the individual timing information $t_{0,i}$ into account when calculating a weighted

average of β^{-1}. This has the benefit that, since the individual $t_{0,i}$ are Gaussian distributed and directly proportional to β_i^{-1}, β_i^{-1} also follows a Gaussian distribution. The calculation of β_i^{-1} and its uncertainty $\sigma_{\beta_i^{-1}}$ can be seen in Equation 5.3 and the weighted average of β^{-1} and its uncertainty are expressed in Equation 5.4.

$$\beta_i^{-1} = \frac{t_{o,i} \cdot c}{d_i} + 1 \qquad \sigma_{\beta_i^{-1}} = \left| \frac{\partial \beta_i^{-1}}{\partial t_{0,i}} \right| \cdot \sigma_{t_{o,i}} = \frac{c}{d_i} \cdot \sigma_{t_{o,i}} \tag{5.3a-b}$$

$$\beta^{-1} = \frac{\sum_i \beta_i^{-1} / \sigma^2_{\beta_i^{-1}}}{\sum_i 1 / \sigma^2_{\beta_i^{-1}}} \qquad \sigma^2_{\beta_i^{-1}} = \frac{1}{\sum_i 1 / \sigma^2_{\beta_i^{-1}}} \tag{5.4a-b}$$

The combined β value of the traversing particle is then obtained by inverting β^{-1} and the uncertainty can be calculated according to Equation 5.5.

$$\beta = \frac{1}{\beta^{-1}} \qquad \sigma_\beta = \beta^2 \cdot \sigma_{\beta^{-1}} \tag{5.5a-b}$$

The distributions for the combined β can be seen in Figure 5.3. Even though the RPCs have a better timing resolution per hit than MDTs, the combined β resolution is worse. This is due to the lower average amount of hits occurring in the RPC system than in the MDT system.

5.3 Run-wise Calibration

During the data-taking period of Run–2, the LHC was filled several times with protons to provide proton–proton collisions at the experiments. Thus, Run–2 is divided into four years of data-taking 2015, 2016, 2017 and 2018 and each year is further segmented into time periods referred to as runs. During one run the LHC and ATLAS are operated at roughly the same setup. Therefore, it is sensible to examine the t_0 distributions as well as to derive and apply calibration constants for each run separately instead of obtaining a calibration constant acquired by investigating the t_0 distribution of an entire year or even the whole of Run–2. Since MDT tubes and the RPC η- and ϕ-strips are treated as independent detector systems, t_0 distributions for every run were analysed for each of those systems separately.

To be considered in this step, the distribution has to have at least 1000 entries. The mean of this fit is subsequently used as the calibration constant. The t_0 distributions and fit of a randomly chosen exemplary run can be seen in Figure 5.4. For MDT tubes, Figure 5.4a, a Gaussian fit with a fitting window of the location of the peak $\pm$ 20% of the histogram range was sufficient as a fitting method. Due to the readout granularity, this method did not yield satisfying results when applied to the distributions of the RPC η- and ϕ-strips, which are depicted in Figure 5.4b and Figure 5.4c, respectively. Consequently, a new fitting strategy was implemented for RPCs.

Instead of just one Gaussian fit, every t_0 distribution was separated into seven intervals of equal length, spread symmetrically around the peak of the distribution.

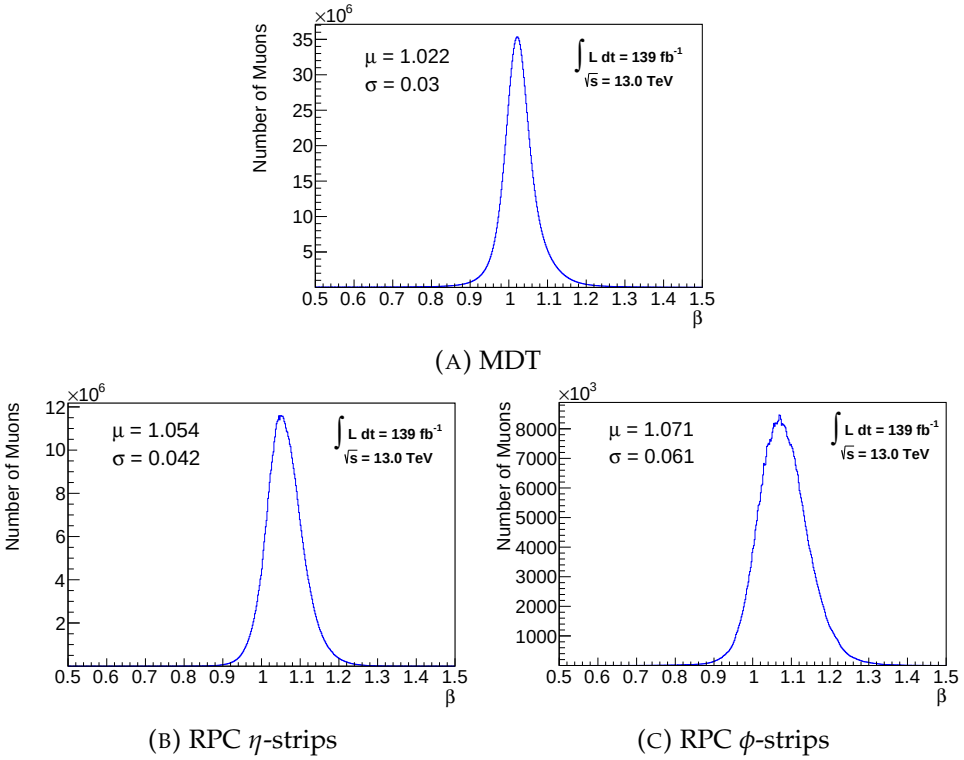

(A) MDT

(B) RPC η-strips

(C) RPC ϕ-strips

FIGURE 5.3: Uncalibrated β distributions for MDT tubes in (A) and RPC η- and ϕ-stripes in (B) and (C), respectively. In addition, the mean and standard deviation of a Gaussian fit using a reduced fitting window of mean $\pm$ RMS are given.

This division does not aim at covering the full range of the displayed histograms, but instead tries to target each side-peak individually. Therefore, a Gaussian fit, covering the entire interval, with its starting point at the intervals peak is conducted and the position of the fitted peak is noted. An additional Gaussian fit, covering the same window as for the MDT distribution, uses these previously fitted peaks as anchor points for its fit. The mean of this final fit is then used as the calibration constant.

The nominal readout granularity for the RPC system is 3.125 ns and was therefore first tried as the interval length. Unfortunately, this did not yield satisfying results as the side-peaks do not occur with a spacing of 3.125 ns. Since the different chamber types BOS, BMS1, BMS2, BOL, BML1 and BML2 are installed at different radii from the interaction point, and could therefore have peaks in t_0 at differing values, an additional division into t_0 distributions for each of those chamber types was investigated. However, this approach was discarded, as it did not significantly improve the outcome. Instead, several interval lengths were tested, while an interval length of 2 ns was empirically chosen for this work.

The calibration constants derived in this step can be seen in Figure 5.5 and the t_0 distributions, after deploying this calibration step, are shown in Figure 5.6. The distribution of the MDT system is shifted nicely towards $\bar{t}_0 = 0$ ns. For both RPC systems the shift towards $\bar{t}_0 = 0$ ns is less effective, but the distributions become less jagged after the calibration is applied and their standard deviation is slightly improved.

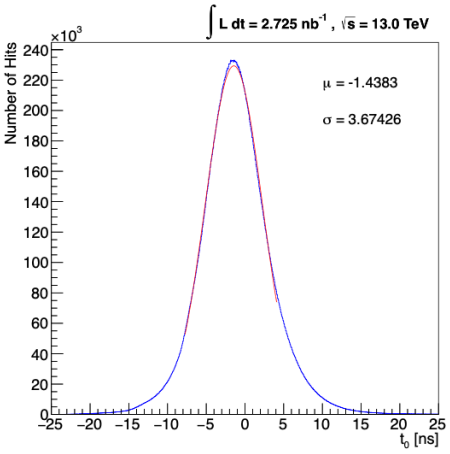

(A) MDT

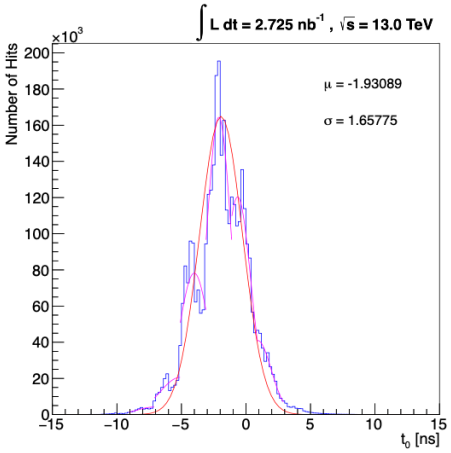

(B) RPC η-strips

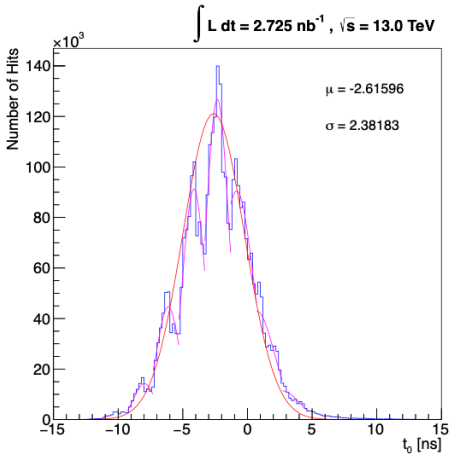

(C) RPC ϕ-strips

FIGURE 5.4: t_0 distributions and fits of the randomly chosen run 305920. (A) depicts the t_0 distribution of the MDT tubes in blue which was fitted by a Gaussian depicted in red. For the RPC η-strips in (B) and RPC ϕ-strips in (C), a more elaborate fitting method was used taking the readout granularity into account. The magenta lines represent a first fitting step, which is then used to produce the final fit depicted in red. The mean and the standard deviation of the final fits are given as well.

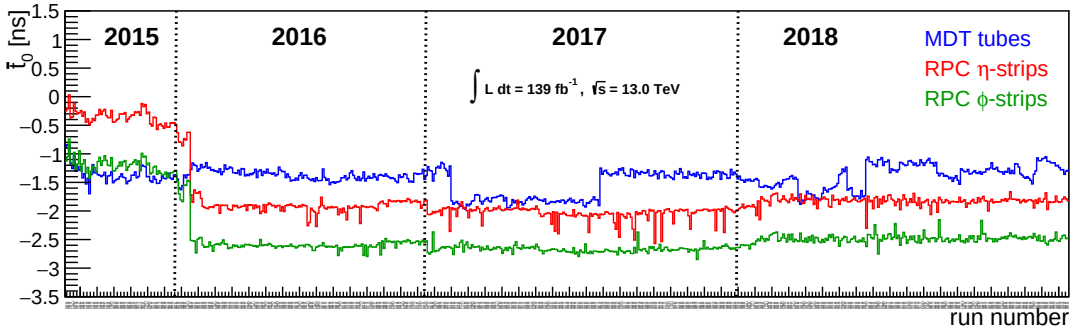

FIGURE 5.5: Calibration constant for every run. The different detector systems are displayed in different colours: MDT tubes in blue, RPC η-strips in red and RPC ϕ-strips in green. The dotted grey vertical lines indicate the last data-taking run of a year.

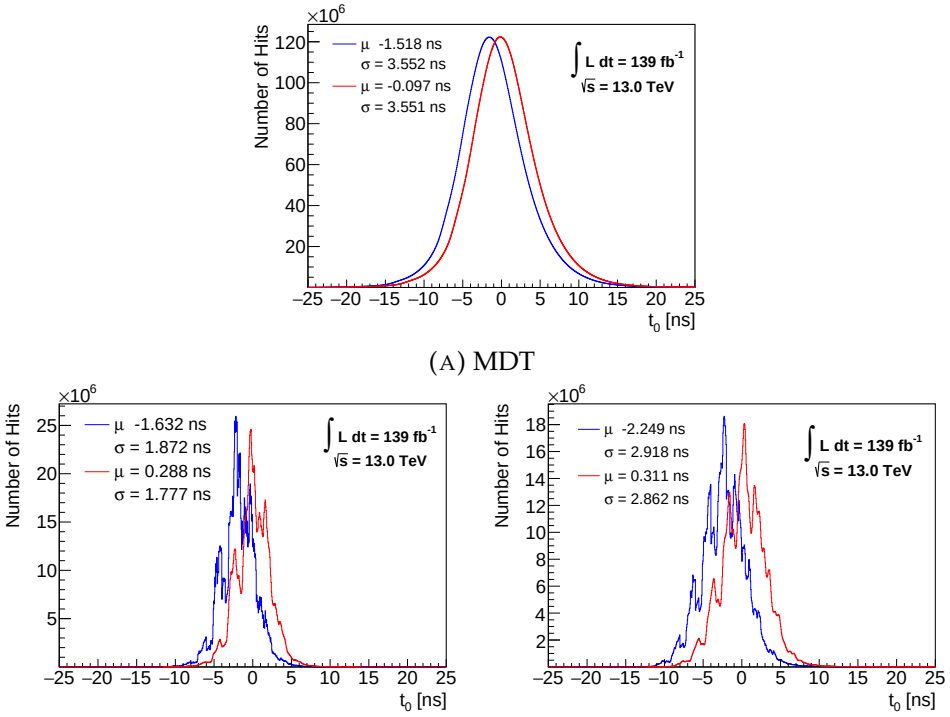

(A) MDT

(B) RPC η-strips

(C) RPC ϕ-strips

FIGURE 5.6: t_0 distributions before (blue) and after (red) the run-wise calibration is applied. Additionally, the mean and standard deviation of a Gaussian fit with reduced fitting window of mean $\pm$ RMS are given. (A) shows the run-wise calibration for MDT tubes, (B) and (C) show the calibration for RPC η- and ϕ-stripes, respectively.

5.4 Element-wise Calibration

The detector modules in the MS are composed of several individual elements. In the data set used in the work at hand, muons satisfying the selection criteria interacted with 354,347 separate MDT tubes and 371,616 different RPC stripes. Since additional data about each element was necessary and only available for 354,292 MDT tubes and 371,333 RPC strips, only hits detected by those elements were considered in this work.

As each element might differ in their t_0 measurement, t_0 distributions were implemented for each element separately and then fitted individually. Due to the large number of elements, the average number of entries per distribution is much smaller than in the previous calibration step. On average, one MDT tube registered approximately 69,000 hits and one RPC strip was hit on average nearly 10,000 times. Through this reduction in statistics, the distributions are not as smooth as in the previous calibration step and thus harder to fit properly, as outliers hold a bigger influence on the fitting procedure and a too large amount of bins could affect the fit negatively. To account for these problems, each t_0 distribution was fitted nine times and additional selection criteria were applied.

- As none of the used methods can be assumed to work reliably, elements with less than 40 registered hits where omitted in this step.
- RPC strips with an RMS greater than 10 ns show a peculiar t_0 distribution and are thus ignored. No such cut was applied for MDTs.
- For the remaining elements, the t_0 distribution was fitted nine times with the following conditions:
  - A Gaussian fit over the full range of [-25 ns, 25 ns].
  - In order to lessen the effect of outliers, a Gaussian fit in a reduced fitting window of [-18 ns, 18 ns] is used, taking the time-spacing between two bunch crossings of 25 ns and some additional nanoseconds for the width of the t_0 distributions into account.
  - To further lessen the impact of outliers, the fitting window of the Gaussian is reduced again to the location of the maximum $\pm$ the RMS provided by the histogram.
  - In order to account for elements with smaller statistics, the created histogram is rebinned by adding neighbouring bins into one. Afterwards, the previous three steps are applied.
  - A second rebinning, summing four neighbouring bins, is carried out and the first three steps are applied.
- The fit with the smallest χ^2 /ndof, with ndof being the number of degrees of freedom of the fit, is chosen as the best fit. When χ^2 /ndof > 300 for the best fit, none of the fits is considered a success.
- For the remaining elements the mean $\bar{t}_0$ and σ_{t_0} are stored and used as calibration constants. When the element was not rejected but no fit was considered a success, the mean and RMS provided by the histogram are used as calibration constants.

The above-mentioned fitting scheme was able to produce correction values for approximately 99.64 % of the regarded MDT tubes. Due to lower statistics and the additional rejection criteria, this percentage is lower for RPC strips, with roughly 96.23 %. In Figure 5.7 the abundances for the different methods providing the best fit are shown. On the left-hand side, the distribution of the ratio per element is shown and the right-hand side is additionally scaled with the number of hits each element provided. Differences of several magnitudes can be seen due to the logarithmic scaling of the y-axis. By comparing both sides, one can see, that the fitting method with smaller ratios per element further decrease their abundance when the hits are taken into account. Consequently, the assumption that elements with a smaller amount of hits need a different fitting method than a plane Gaussian can be confirmed.

For MDT tubes the smallest fitting window of mean $\pm$ RMS is used most often, which could point towards a higher amount of hits at the tails of the t_0 distribution than expected and thus a deviation from the Gaussian shape. Methods including a rebinning are less likely to provide the best fit than their counterpart performed on the initial histogram. As long as no rebinning is involved, the method covering the entire range produces the best results for both RPC strips slightly more often than the method with the smallest range. Similar to the MDTs, methods including the rebinning are less likely to result in the best fit than methods without it. However, once a rebinning is used, the smallest fitting window yields the best results most often.

The effect of the element-wise calibration on the t_0 distributions can be seen in Figure 5.8. For the MDT tubes, this calibration brings the centre of the distribution very close to $\bar{t}_0 = 0$ ns, and decreases the width slightly. The calibration step is able to almost entirely erase the spiky nature of the t_0 distribution, induced by the readout granularity, for both RPC systems. While the side-peaks are fully washed-out, a small bump distorting the Gaussian shape at negative t_0 values can be seen in both RPC systems as a possible remnant of the previously spiky structure. The smoother distribution is not the only positive effect, both t_0 distributions are pushed significantly closer towards $\bar{t}_0 = 0$ ns, and their width is decreased. The reduction of the standard deviation is more effective for the RPC ϕ-stripes and brings the previous broader distribution to almost the same width as the distribution for the RPC η-stripes.

To completely reduce the effects of the different setups of the ATLAS MS during Run–2, it would be necessary to perform the run-wise and element-wise calibration simultaneously instead of successively. However, this approach is currently not feasible as it encounters two major obstacles, which lead to the successive strategy being used in this work. Firstly, the amount of registered hits per element was already a reason for concern when calculating calibration constants for each element for the entirety of Run–2. A division into the 593 individual runs would further lower the statistics and thus decrease the amount of elements, for which meaningful calibration constant can be derived. On the computational side, with over 725,000 individual elements and 593 different runs regarded in this calibration, the amount of data needing to be processed would exceed memory and computing power capabilities at the time of writing.

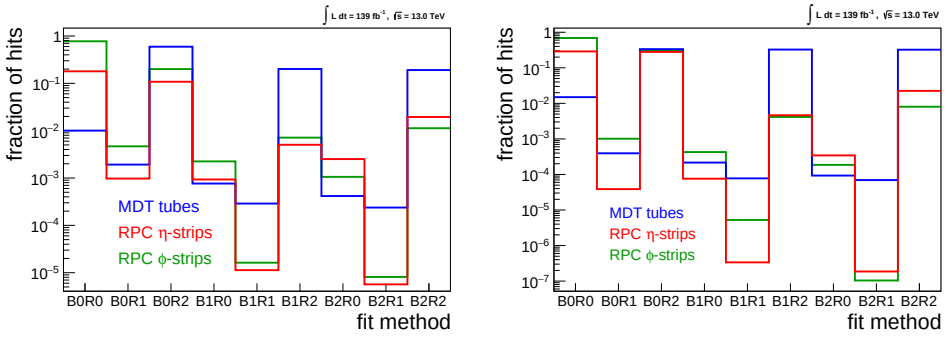

(A) (B)

FIGURE 5.7: Distribution showing which fit was chosen as the best, as a fraction of all successful fits on a logarithmic scale. Fits on the primary histogram are abbreviated with B0, B1 and B2 indicate the first and second rebinning, respectively. The abbreviation Ri denotes which range was used for the fit. R0 uses the full t_0 range of [-25 ns, 25 ns], R1 the reduced range of [-18 ns, 18 ns] and R2 the even further reduced fitting window of mean ± RMS. The three different detector systems are displayed in various colours: MDT tubes in blue, RPC η-strips in red and RPC ϕ-strips in green. (A) shows the distribution per detector element and (B) the distribution per hit.

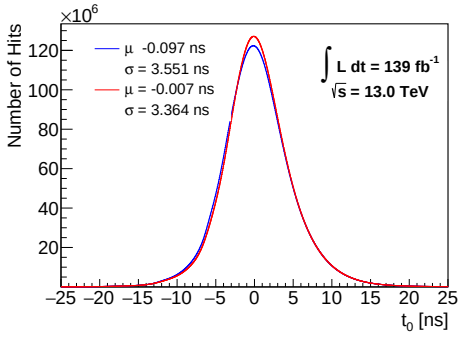

(A) MDT

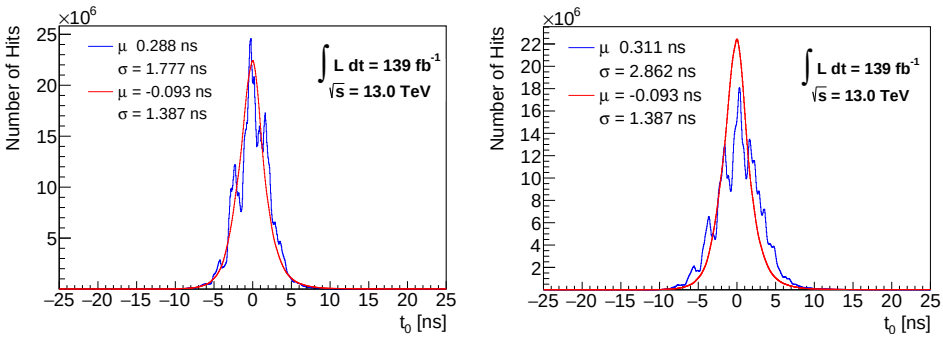

(B) RPC η-strips (C) RPC ϕ-strips

FIGURE 5.8: t_0 distributions before (blue) and after (red) the element-wise calibration is applied. Additionally, the mean and standard deviation of a Gaussian fit with reduced fitting window of mean ± RMS are given. (A) shows the element-wise calibration for MDT tubes and (B) and (C) show the calibration for RPC η- and ϕ-stripes, respectively.

5.5 Drift-time Calibration

A further dependency investigated is the correlation between the drift time t_{drift} of charges in the MDT tubes and the measured t_0 value. The correlation between t_{drift} and t_0 is shown in Figure 5.9a with the mean of a Gaussian fit performed for every t_{drift}-bin added in red.

Even though the nominal maximum for t_{drift} is 700 ns, recall Section 3.2.3, the figure clearly shows hits occurring with drift times exceeding this limitation. This is due to the fact, that t_{drift} is actually not measured in the MDT but rather recalculated from the track fit during the reconstruction process. This calculation has some leniency with regards to the physical barriers of t_{drift}, and thus hits measured with a very large t_0 can be assigned a t_{drift} exceeding 700 ns. However, it is not sensible to assign a large t_{drift} value to a small t_0 measurement. Instead, measurements of small t_0 values are assigned very low values of t_{drift}. This reconstruction process can explain the decreasing mean of the Gaussian fit for low, and the rise in the mean for very large t_{drift} values. For drift times exceeding 765 ns, the Gaussian fit returns a mean even exceeding the 10 ns range depicted in the figure. The mean has a clear upwards trend with increasing t_{drift} on the left side of the figure and plateaus around 2 ns. Before rising out of the range of the figure, it first dips towards negative $\bar{t}_0$ values. As the MDT tubes use a drift gas with a highly non-linear space-drift-time relation, the decrease of the mean in the region 650 ns $< t_{\text{drift}} <$ 725 ns can probably be attributed to an incorrect modelling of the drift gas during the reconstruction and the fact that t_{drift} is recalculated from the t_0 measurement.

The calibration strategy is the same as in the previous steps. The mean of the Gaussian fit in each t_{drift}-bin is used as a correction constant for the t_0 measurement of hits within the specific t_{drift} range. The results of an attempt to implement this strategy can be seen in Figure 5.9b. It is obvious, that this attempt did not yield the wanted results. While the evolution of the mean with t_{drift} is less pronounced, which can be viewed as a success, the actual value of the mean differs largely from the expectation of a flat line at $t_0 = 0$ ns. The calibration seems to overcorrect and brings the mean of the Gaussian fit for each t_{drift}-bin close to a line at $t_0 = -2$ ns. The spread of the mean at very high t_{drift} values can be explained by the t_0 distribution of that bin slowly reaching the limits of the produced histograms, which results in the fit starting to yield unreliable results.

The effect of this calibration step on the t_0 distribution of the MDT tubes can be seen in Figure 5.10. The overcorrection results in a shift of the mean of the distribution away from the targeted $\bar{t}_0 = 0$ ns. Due to the reduced t_{drift} dependency of the mean, the width of the distribution is decreased. As decreasing the width is one of the goals of this calibration and the general shift in t_0 can be dealt with in the following step, the calibration is still applied to the data. However, the cause of the overcorrection needs further investigation and the placement of this calibration step within the calibration order needs to be questioned since more calibration steps following this one would decrease the impact of the shift of $\bar{t}_0$.

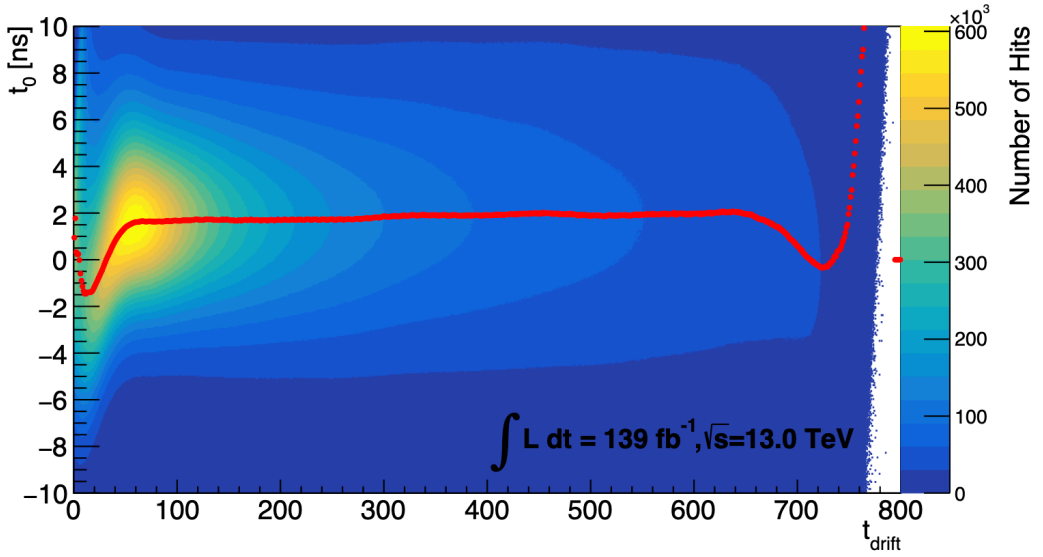

(A)

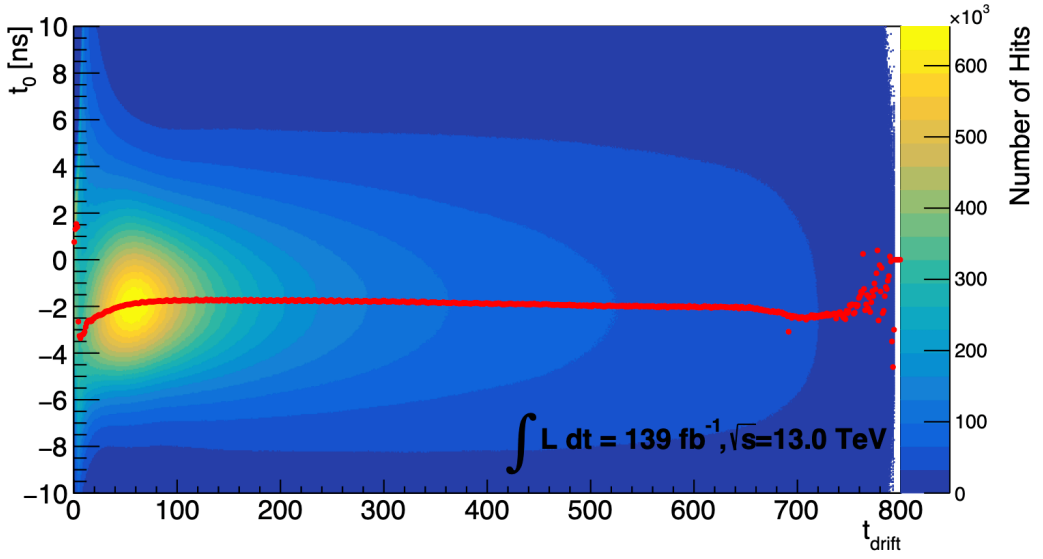

(B)

FIGURE 5.9: The correlation between t_0 and t_{drift} for MDT tubes. (A) shows the correlation before, and (B) after the drift-time calibration is applied. For each t_{drift}-bin, the mean of a Gaussian fit with reduced fitting window of mean $\pm$ RMS is shown in red.

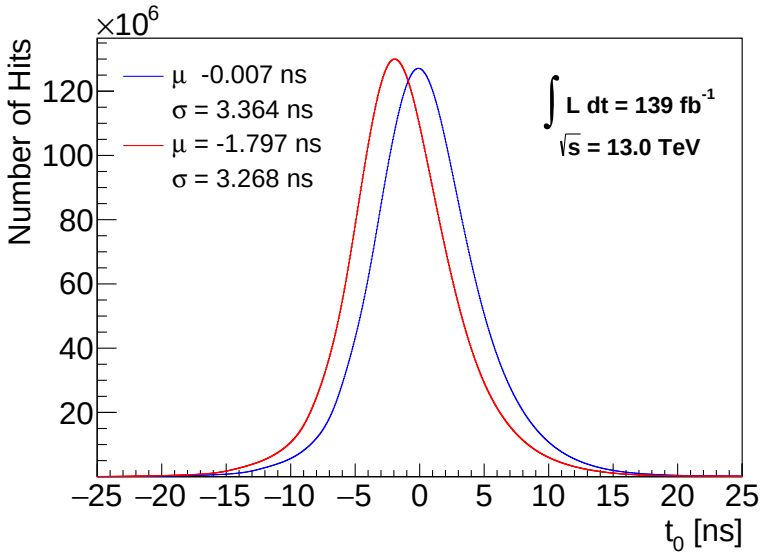

FIGURE 5.10: Effect of the drift-time calibration on the t_0 distribution of the MDT tubes. The distribution before the calibration is applied is depicted in blue while the red graph demonstrates the distribution after the calibration is applied. Additionally, the mean and standard deviation of a Gaussian fit with reduced witting window of mean $\pm$ RMS are given.

5.6 Phi Calibration

The last dependency investigated in this work is the impact of the location of the detector elements along different ϕ values on the t_0 measurement. The correlation for the MDT tubes between ϕ and t_0 is depicted in Figure 5.11a, additionally the mean of a Gaussian fit for every ϕ-bin, with a fitting window of mean $\pm$ RMS is drawn in red.

Firstly, a periodic occurrence of 16 small ϕ-regions registering additional hits can be observed. This is explained by the detector layout depicted in Figure 3.10. In order to avoid blind spots, the different small and large chambers are installed with an overlap in their ϕ coverage. Therefore, a particle traversing the detector at ϕ values in these overlapping regions can registers hits in both the small and the large chamber, which is the reason why more hits are counted in this overlapping region than in ϕ regions covered exclusively by a large or small chamber. As the ATLAS MS uses small and large chambers in an alternating fashion, the distance between two of these overlap regions is either the ϕ coverage of a small or a large chamber. The mean of each ϕ-bin shows a periodic sawtooth structure with two different lengths and peaks in the overlapping regions. This sawtooth structure is a consequence of the distance of the readout module from the hit occurring in the MDT chamber. As the propagation time of the signal along the wire inside one MDT tube is not taken into account, hits registered very close to the readout system are assigned a smaller t_0 than hits registered in a large distance from the readout system, additionally the distance from the IP might vary for different ϕ. Furthermore, this mean distribution is not deviating in this sawtooth manner from a line at $t_0 = 0$ ns, but rather a line closer to $t_0 = 1.8$ ns as a result of the shift of the general t_0 distribution introduced in the previous calibration step.

The same calibration method used in the previous steps is applied and the mean

of each ϕ-bin of Figure 5.11a is used as a correction constant for the t_0 measurement registered at the corresponding ϕ. The result of this calibration can be seen in Figure 5.11b. The ϕ dependency of the mean of each ϕ-bin resembles a horizontal line closely as the sawtooth structure is flattened significantly, while not being entirely dissolved. In addition, this horizontal line is now placed closely to the expected value of $t_0 = 0$ ns. Since the ϕ positions of the readout system are not the same for the barrel and in the end-cap system, a division into correlations for both systems separately might be a valuable approach to further increase the effectiveness of this calibration step. Additionally, it might proof useful to investigate the ϕ dependency for small and large chambers separately.

The correlation between ϕ and t_0 for RPC η-strips is shown in Figure 5.12a with the mean of a Gaussian fit for each ϕ-bin added in red. Similar to the distribution for the MDT tubes, a periodic structure can be seen in ϕ. This is explained by an imperfect calculation of the propagation time of the signal along the strip, leading, similarly as for the MDT tubes, to a dependency of the measured t_0 value on the distance from the hit to the readout system. As RPC η modules are split along ϕ into two units, each sector produces a "V"-like shape with the bottom tip of the "V" located in the centre of a sector. The mean of each ϕ-bin loosely represents this "V"-shape but there are numerous outliers towards negative t_0 values from the general shape, thus indicating potential problems with the fitting method.

Figure 5.12b shows the same correlation after the calibration is applied. While the amount of outliers towards negative t_0 is reduced, additional outliers towards positive t_0 values appear. This is a clear indication of the fitting method not yielding the best results. While the spiky nature of the general t_0 distribution for the RPC η-strips was almost dissolved entirely by the run- and element-wise calibration, for the individual ϕ-bins the side-peaks are still visible. This leads to the implemented fitting method not yielding reliable results due to the side-peaks affecting the fit negatively. The fitting process for this step does, therefore, need further improvement, a similar strategy as deployed in the run-wise calibration might lead to more reliable outcomes of the fitting process.

Regarding the RPC ϕ-strips no real dependency on ϕ was expected and no dependency of t_0 on ϕ is observed in Figure 5.12. Since the mean of the t_0 distribution was still slightly shifted from the goal of $\bar{t}_0 = 0$ ns, the calibration is still applied and the results are investigated.

The effect of this calibration step on the t_0 distributions for MDT tubes and RPC η- and ϕ-strips can be seen in Figure 5.14. The shift of the mean of the distribution for MDT tubes introduced in the previous calibration step is corrected almost completely, while the improvement in the standard deviation and therefore the width of the distribution was conserved. For the RPC η-strips, the mean of the distribution is pushed closer towards the goal of $\bar{t}_0 = 0$ ns, and the slight improvement in the ϕ dependency results in a marginally reduced width of the distribution. The distribution for the RPC ϕ-strips is pushed a little closer towards $\bar{t}_0 = 0$ ns, while it simultaneously worsens the standard deviation mildly and therefore widens the distribution slightly.

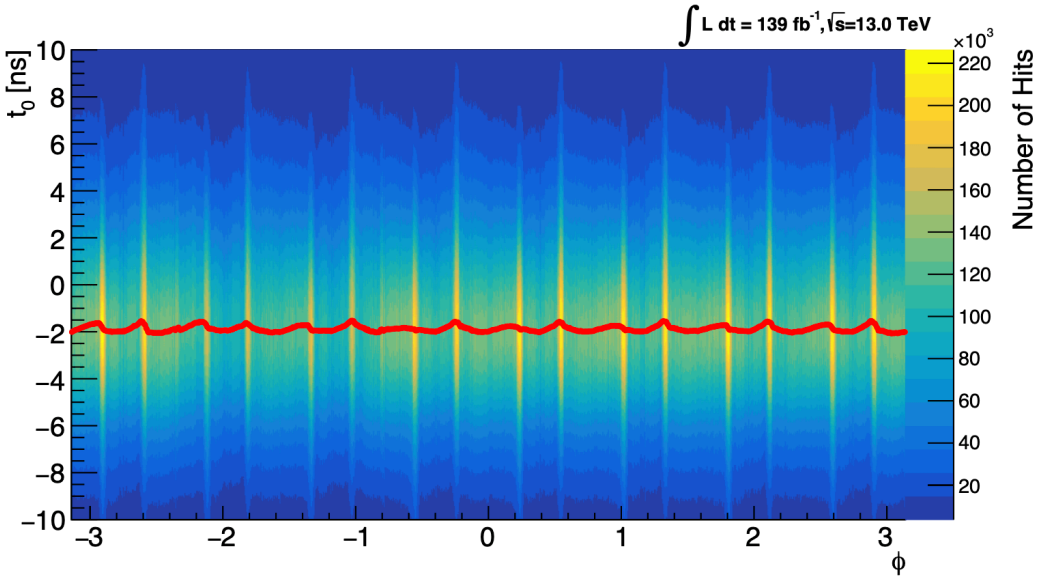

(A)

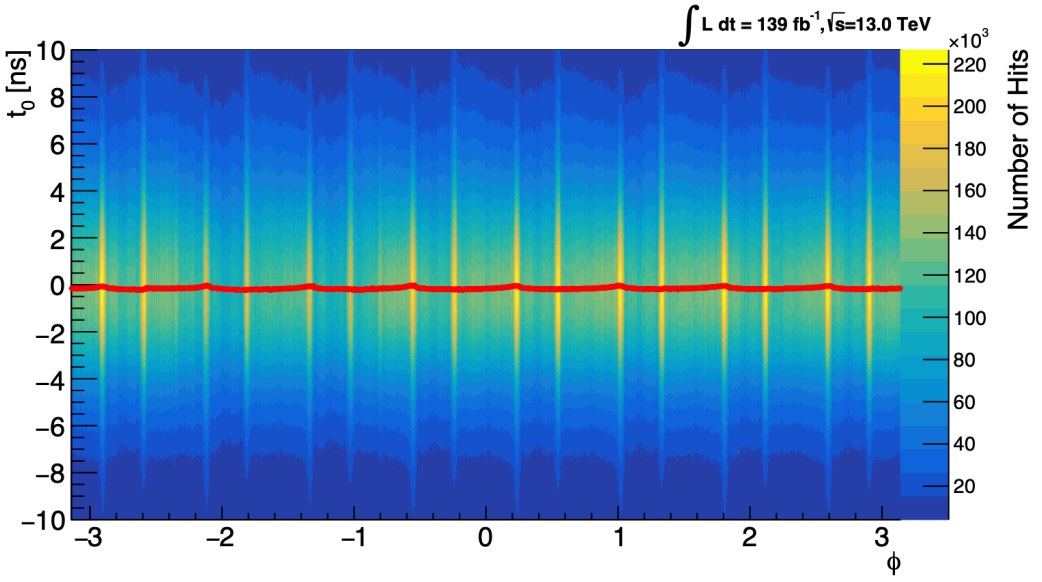

(B)

FIGURE 5.11: The correlation between t_0 and ϕ for MDT tubes. (A) shows the correlation before, and (B) after the drift-time calibration is applied. For each ϕ-bin, the mean of a Gaussian fit with reduced fitting window of mean $\pm$ RMS is shown in red.

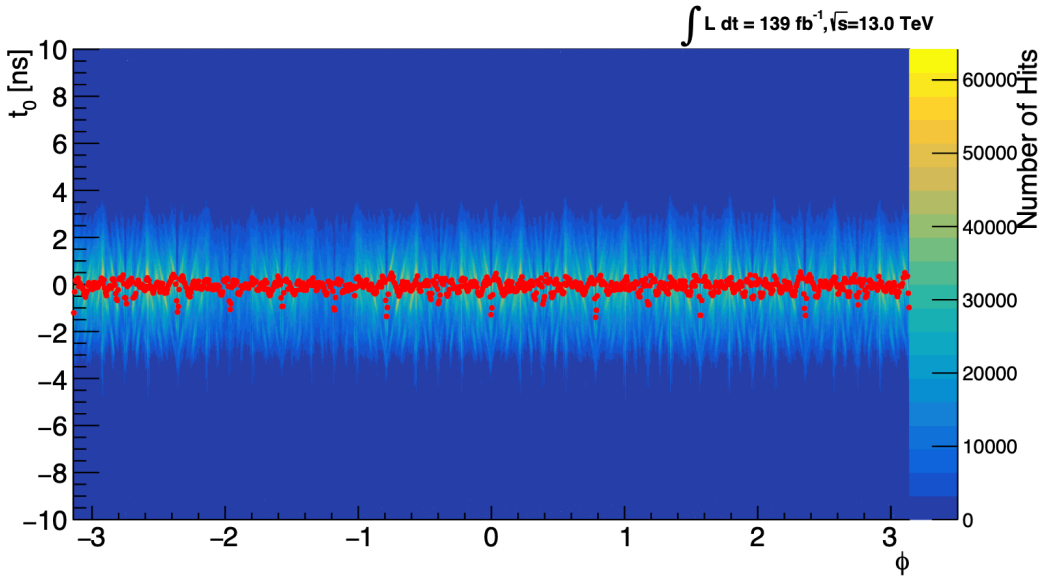

(A)

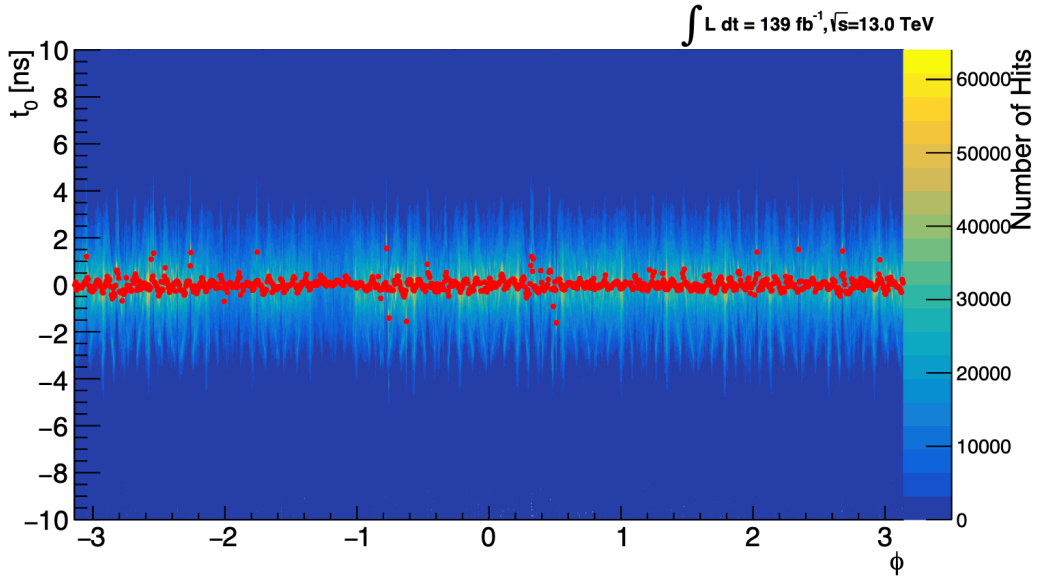

(B)

FIGURE 5.12: The correlation between t_0 and ϕ for RPC η-strips. (A) shows the correlation before, and (B) after the drift-time calibration is applied. For each ϕ-bin, the mean of a Gaussian fit with reduced fitting window of mean $\pm$ RMS is shown in red.

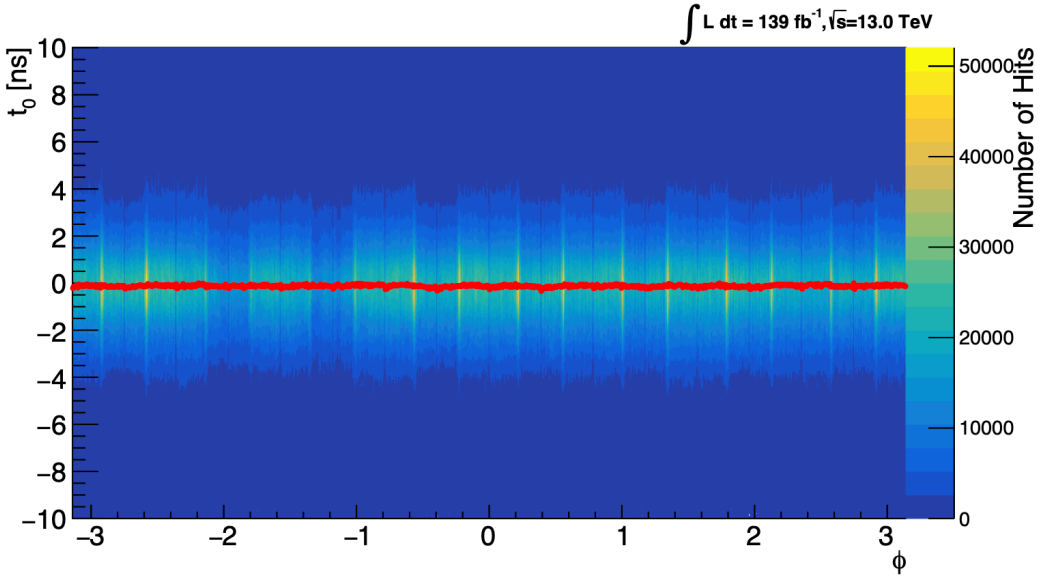

(A)

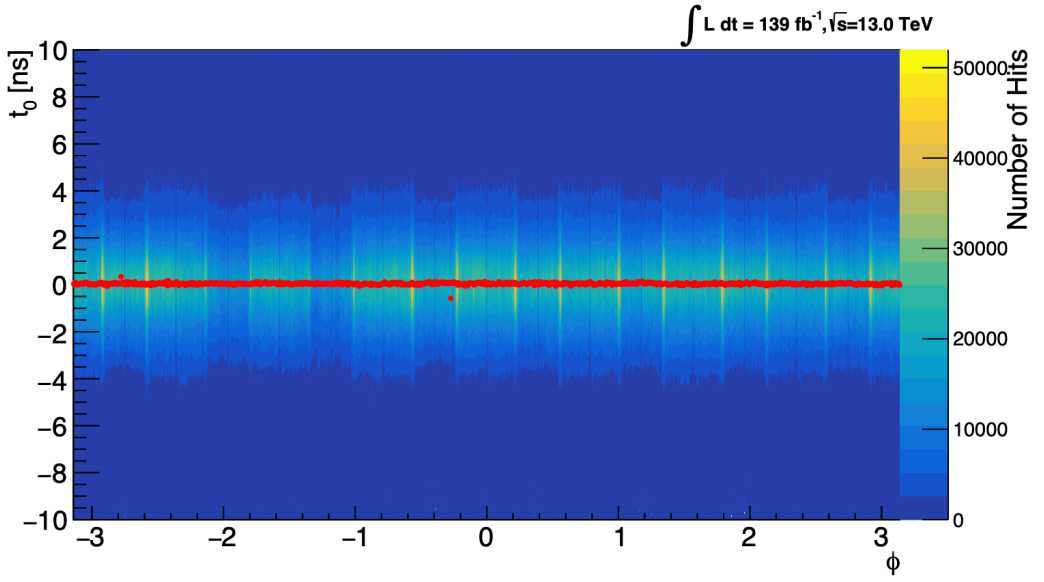

(B)

FIGURE 5.13: The correlation between t_0 and ϕ for RPC ϕ-strips. (A) shows the correlation before, and (B) after the drift-time calibration is applied. For each ϕ-bin, the mean of a Gaussian fit with reduced fitting window of mean $\pm$ RMS is shown in red.

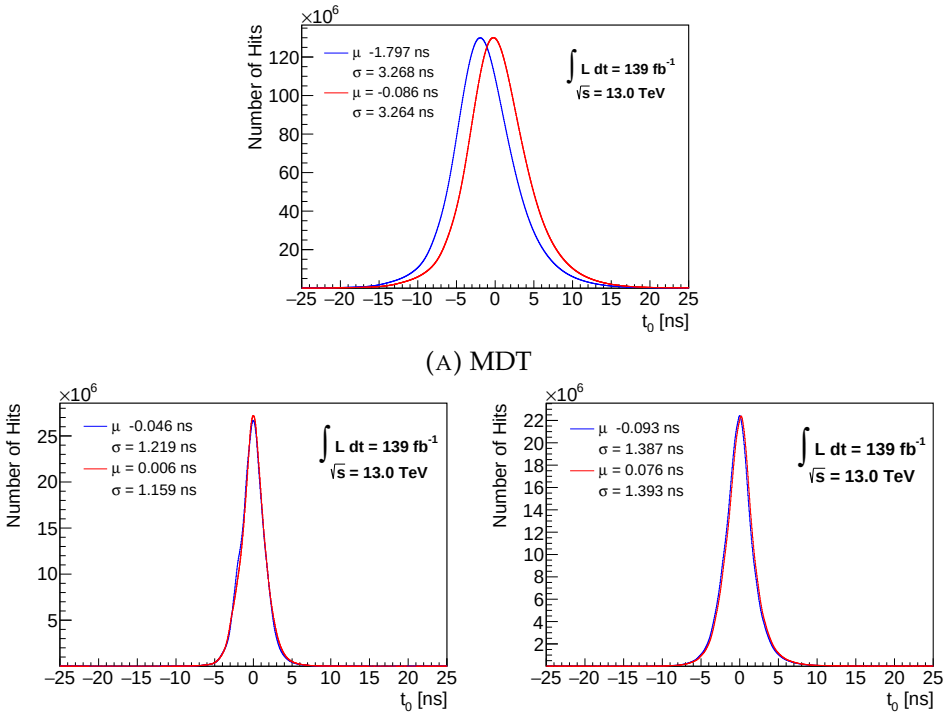

(A) MDT

(B) RPC η-strips

(C) RPC ϕ-strips

FIGURE 5.14: t_0 distributions before (blue) and after (red) the phi calibration is applied. Additionally, the mean and standard deviation of a Gaussian fit with reduced fitting window of mean $\pm$ RMS are given. (A) shows the phi calibration for MDT tubes, while (B) and (C) show the calibration for RPC η- and ϕ-stripes, respectively.

5.7 Final β Resolution and Pull

The goal of these calibration steps was to improve the t_0 measurement of each element in the ATLAS MS, and thereby the distribution of the combined β measurement, that can be calculated according to Equation 5.5. The effect of the calibration strategy described in this chapter on the timing measurement of the detector systems investigated in this thesis can be seen in Figure 5.15. The intention was to centre the t_0 distribution around $\bar{t}_0 = 0$ ns and to decrease the width of the distribution. For the MDT tubes, the mean of the distribution is moved from -1.518 ns to -0.086 ns and the standard deviation is improved from 3.552 ns to 3.264 ns. By getting rid of the shift introduced by the drift-time calibration, the mean should be pushed even further towards zero. The distribution for both RPC systems showed a spiky structure due to the granularity of the readout system. This jagged structure can be removed by the calibration method almost entirely. Only small side-bumps remain as possible remnants of the readout granularity. The distribution for RPC η-strips is pushed from a mean of -1.632 ns to 0.006 ns and thus is almost perfectly centred around zero. The standard deviation is reduced from 1.872 ns to 1.159 ns, and the general shape does comply with a Gaussian significantly better after the calibration is applied. For the RPC ϕ-strips, the mean is shifted from -2.249 ns to 0.076 ns and the standard deviation lowered from 2.918 ns to 1.393 ns and similarly to the distribution of the RPC η-strips, the t_0 distribution resembles a Gaussian significantly better after the calibration is performed.

The effect of this calibration process on the combined β measurement can be seen in Figure 5.16, and shows a clear improvement for every detector system. For all three detector systems, the mean of the distribution is pushed significantly closer towards $\bar{\beta} = 1$, and the width is reduced. For the MDT tubes, the standard deviation is reduced from 0.03 to 0.027, for RPC η-stripes from 0.042 to 0.028 and for RPC ϕ-stripes from 0.061 to 0.031. The bigger improvements for the RPC systems are most likely attributed to the dissolving of the spiky nature of the t_0 distributions coming from the readout granularity.

Before the measurements of the three detector systems can be combined in a meaningful way, it has to be assured that the σ_β represents the measurement uncertainties accurately. This can be done by evaluating the pull, as defined in Equation 5.6.

$$p := \frac{1 - \beta_i^{-1}}{\sigma_{beta_i^{-1}}} \tag{5.6}$$

If the measurement uncertainties are reflected correctly, the pull is known to be of Gaussian shape with a mean of zero and a standard deviation of one. The pull distributions for the different detector systems can be seen in Figure 5.17. The Figure shows a clear deviation of a Gaussian shape with mean zero and standard deviation one. Consequently, the σ_β have to be corrected according to Equation 5.7.

$$\sigma_\beta^{corr} = \sigma_\beta \cdot (1 + |1 - \sigma_p|) \tag{5.7}$$

Rounded to the same decimal, this leads to σ_β^{corr} being 0.027 for the MDT tubes, 0.030 for the RPC η-strips and 0.034 for the RPC ϕ-strips, which is an improvement compared to the uncalibrated data.

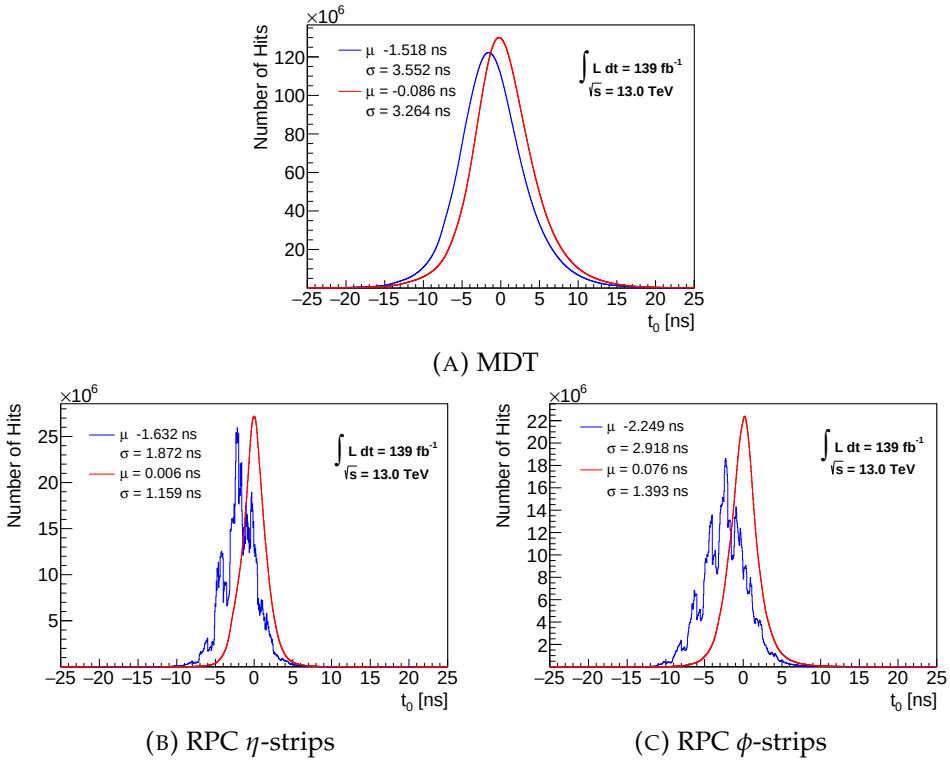

(A) MDT

(B) RPC η-strips

(C) RPC ϕ-strips

FIGURE 5.15: Comparison between the uncalibrated (blue) and calibrated (red) t_0 distributions for the MDT tubes in (A), and RPC η- and ϕ-stripes in (B) and (C), respectively. Additionally, the mean and standard deviation of a Gaussian fit using a reduced fitting window of mean $\pm$ RMS are given.

A comparison of the combined β measurement in the ATALS MS before and after the calibration is applied can be seen in Figure 5.18. The mean is pushed from 1.029 to 0.996 and thus significantly closer to the expected value of $\bar{\beta} = 1$. The standard deviation is reduced from 0.03 to 0.022. A previous analysis on a timing-calibration using the data from 2015 and 2016 of Run–2, which amounts to an integrated luminosity of 36.1 fb^{-1} [131], resulted in a final β distribution with $\bar{\beta}$ = 0.997 and σ_β = 0.021. This indicates, that the timing resolution for the first two years of Run–2 might be better than for the last two years. Another previously done analysis on the timing measurement of the ATLAS MS is presented in [127]. It was conducted during the end of the data-taking period of Run–2 and had a dataset of 128.3 fb^{-1}, resulting in a β distribution with $\bar{\beta}$ = 1.002 and σ_β = 0.022. While the width is comparable to the calibration presented in the work at hand, the mean is shifted closer towards the intended mean of $\bar{\beta}$ = 1. This is likely an effect of the shift introduced in the drift-time calibration, which is not fully reversed by the following phi-calibration.

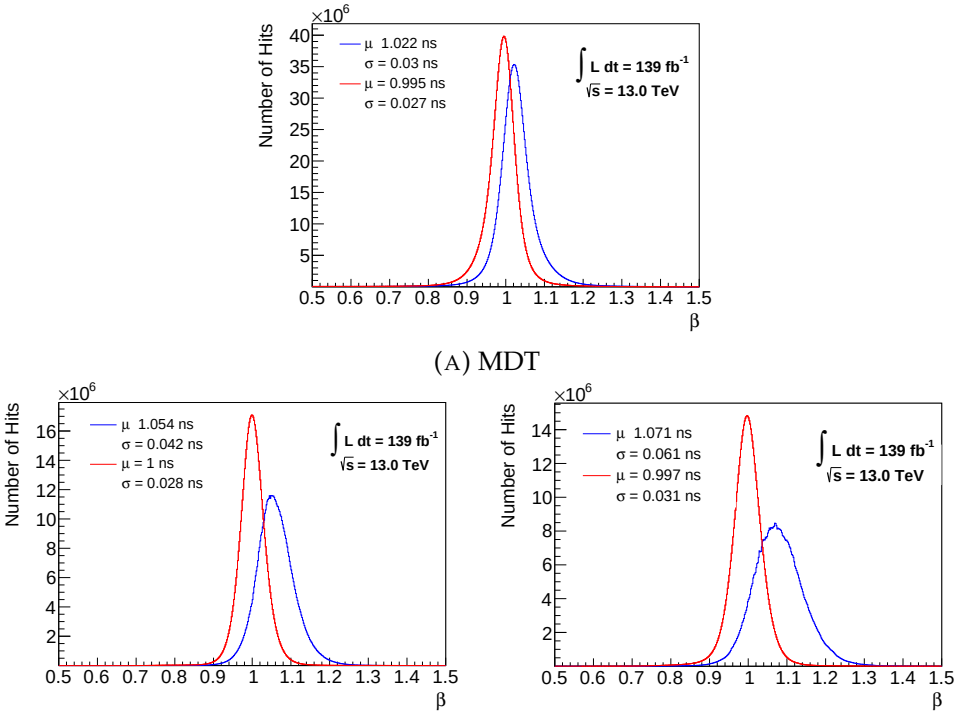

(A) MDT

(B) RPC η-strips

(C) RPC ϕ-strips

FIGURE 5.16: Comparison between the uncalibrated (blue) and calibrated (red) combined β distributions for the MDT tubes in (A), and RPC η- and ϕ-stripes in (B) and (C), respectively. Additionally, the mean and standard deviation of a Gaussian fit using a reduced fitting window of mean $\pm$ RMS are given.

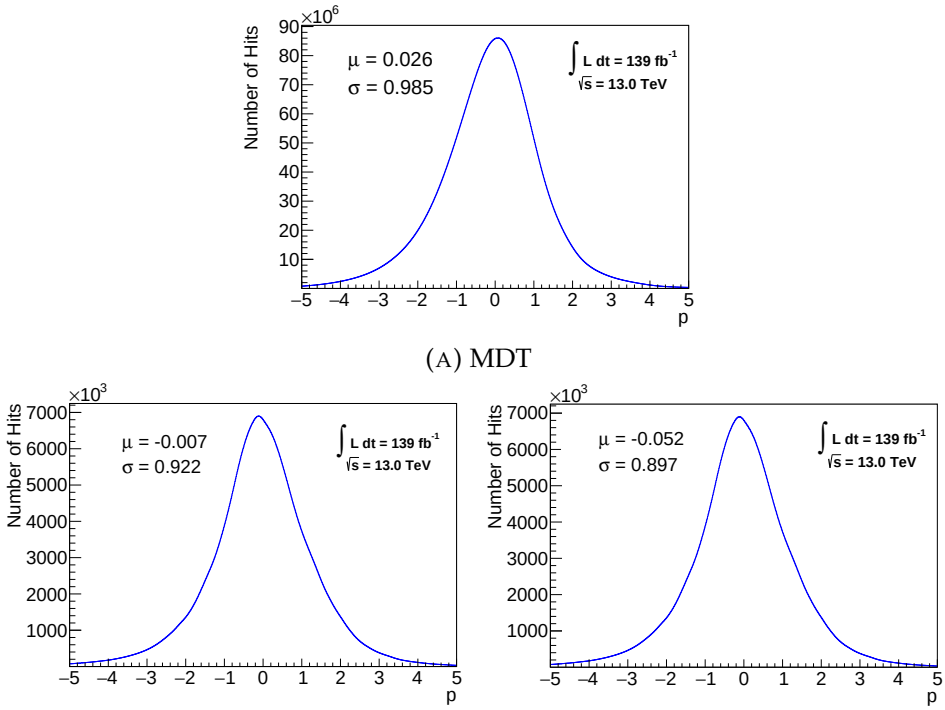

FIGURE 5.17: Pull distributions for the MDT tubes in (A), and RPC η- and ϕ-stripes in (B) and (C), respectively. Additionally, the mean and standard deviation of a Gaussian fit using a reduced fitting window of mean $\pm$ RMS are given.

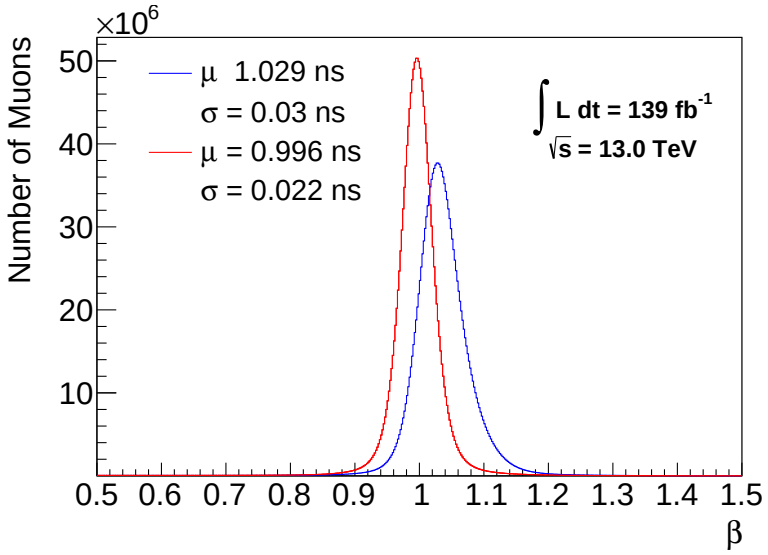

FIGURE 5.18: Comparison between the combined β measurement in the ATLAS MS before (blue) and after (red) the calibration is applied. Additionally, the the mean and standard deviation of a Gaussian fit using a reduced fitting window of mean $\pm$ RMS are given.

Chapter 6

Conclusion and Outlook

This thesis presents a calibration procedure for the timing measurement of the MDT and RPC system of the ATLAS muon spectrometer using Run–2 data with a search for charged stable massive particles in mind. To exploit the signature of slowly propagating SMPs by a time-of-flight measurement in the ATLAS muon spectrometer, a good understanding of the timing measurements of MDT tubes and RPC strips is necessary. Therefore, four calibration steps were conducted with the aim of improving the final β resolution. Since MDT tubes, RPC η-strips and RPC ϕ-strips are read out separately, the calibration steps are done individually for each system.

As the setup of the LHC and ATLAS might differ between each period of data-taking, the calibration procedure starts with a run-wise calibration. Afterwards, a correction constant is derived for each detector element individually to further increase the comparability of the measurements taken from two different detector elements. The third calibration step investigates the correlation between the drift-time calculated for MDT tubes and their timing measurement. The following final step is a correction of the timing measurement for the positioning along the ϕ-direction of the detector element. To accurately represent the measurement uncertainties, the final β uncertainties are adjusted by a pull correction. Through this procedure the the final β distribution is more accurately centred around $\bar{\beta} = 1$ and the resolution is improved from $\sigma = 0.03$ to $\sigma = 0.027$ for the MDT system, from $\sigma = 0.042$ to $\sigma = 0.030$ for the RPC η-strips and from $\sigma = 0.061$ to $\sigma = 0.034$ for the RPC ϕ-strips.

While this shows an improvement over the uncalibrated data, further investigation of the individual calibration steps might lead to in an even better result. The fitting procedure of the run-wise calibration was executed with an empirically found interval length of 2 ns. Here, a procedure automatically choosing the best interval length for each run individually might further increase the effectiveness of this calibration step. It might also be useful to further investigate the reason for the occurring side-peaks, especially as they do not appear with a timing-distance of 3.125 ns. This might be able to fully resolve the spiky nature of the t_0 distributions for the RPCs but might require information currently not available in the data-set used in this work. In the drift-time calibration, a general shift of the timing measurement was introduced, which is not intended. By finding and removing the cause of this shift, the results should increase further. For the phi calibration a division between the barrel and end-cap regions for the MDT tubes might proof beneficial, as well as a further investigation of the fitting method used for the RPC η-strips. Even though the ordering of the calibration steps was chosen to maximise the comparability between the timing measurements of different elements first, an investigation into how this ordering affects the outcome could be useful. Additionally, the effect of a flag set for muons, which comply with additional criteria for muons coming from $Z \rightarrow \mu\mu$

decays, could effect the outcome of the calibration. As it reduces the available statistics, this needs to be looked at for each calibration step individually.

Since searches for charged stable massive particles require Monte Carlo simulated events, the calibration must also be applied to simulated events and it must be assured that the t_0 and β distributions for the simulated events match those of the real data before a search for charged stable massive particles with the Run–2 data of the ATLAS detector can be conducted. Additionally, it is useful to combine the timing information of the MS with the timing measurement of the tile calorimeter. A calibration of the timing measurement in the tile calorimeter is currently in progress. When this is done, a search for charges stable massive particles can be done with the full dataset of 139 fb^{-1} taken during Run–2 at $\sqrt{s}$ = 13 TeV. Such a search should be able to either provide even stronger model-independent exclusion limits on the production cross-section for charged stable massive particles or be able to observe them directly and thus prove the existence of physics beyond the Standard Model.

Bibliography

[1] ATLAS Collaboration. "Observation of a new particle in the search for the Standard Model Higgs boson with the ATLAS detector at the LHC." In: *Phys. Lett. B* 716.arXiv:1207.7214. CERN-PH-EP-2012-218 (Aug. 2012), 1–29. 29 p. DOI: 10.1016/j.physletb.2012.08.020. URL: https://cds.cern.ch/record/1471031.

[2] CMS Collaboration. "Observation of a new boson at a mass of 125 GeV with the CMS experiment at the LHC." In: *Phys. Lett. B* 716.CMS-HIG-12-028. CMS-HIG-12-028. CERN-PH-EP-2012-220 (July 2012), 30–61. 32 p. DOI: 10.1016/j.physletb.2012.08.021. URL: https://cds.cern.ch/record/1471016.

[3] D. J. Griffiths. *Introduction to elementary particles; 2nd rev. version*. Physics textbook. New York, NY: Wiley, 2008. URL: https://cds.cern.ch/record/111880.

[4] Guido A. *Collider Physics within the Standard Model: a Primer*. 2013. arXiv: 1303.2842 [hep-ph].

[5] Particle Data Group. "Review of Particle Physics, 2014-2015." In: *Chin. Phys. C* 38 (2014). All tables, listings, and reviews (and errata) are also available on the Particle Data Group website: http://pdg.lbl.gov, p. 090001. DOI: 10.1088/1674-1137/38/9/090001. URL: https://cds.cern.ch/record/1753419.

[6] V. Martin. *Particle Physics Lecture Slides*. 2013. URL: https://www2.ph.ed.ac.uk/~vjm/Lectures/SH_IM_Particle_Physics_2013_files/ParticlePhysics2013Notes.pdf (visited on 07/22/2020).

[7] H. Nishino et al. "Search for Proton Decay via $p \to e^+\pi^0$ and $p \to \mu^+\pi^0$ in a Large Water Cherenkov Detector". In: *Phys. Rev. Lett.* 102 (14 Apr. 2009), p. 141801. DOI: 10.1103/PhysRevLett.102.141801. URL: https://link.aps.org/doi/10.1103/PhysRevLett.102.141801.

[8] J. Beringer et al. "Review of Particle Physics". In: *Phys. Rev. D* 86 (1 July 2012), p. 010001. DOI: 10.1103/PhysRevD.86.010001. URL: https://link.aps.org/doi/10.1103/PhysRevD.86.010001.

[9] S.L. Glashow, J. Iliopoulos, and L. Maiani. "Weak Interactions with Lepton-Hadron Symmetry". In: *Phys. Rev. D* 2 (1970), pp. 1285–1292. DOI: 10.1103/PhysRevD.2.1285.

[10] M. Kobayashi and T. Maskawa. "CP Violation in the Renormalizable Theory of Weak Interaction". In: *Prog. Theor. Phys.* 49 (1973), pp. 652–657. DOI: 10.1143/PTP.49.652.

[11] S. Weinberg. "A Model of Leptons". In: *Phys. Rev. Lett.* 19 (1967), pp. 1264–1266. DOI: 10.1103/PhysRevLett.19.1264.

[12] P. W. Higgs. "Broken Symmetries and the Masses of Gauge Bosons". In: *Phys. Rev. Lett.* 13 (1964). Ed. by J.C. Taylor, pp. 508–509. DOI: 10.1103/PhysRevLett.13.508.

[13] B. Aharmim et al. "Electron energy spectra, fluxes, and day-night asymmetries of B-8 solar neutrinos from measurements with NaCl dissolved in the heavy-water detector at the Sudbury Neutrino Observatory". In: *Phys. Rev. C* 72 (2005), p. 055502. DOI: 10.1103/PhysRevC.72.055502. arXiv: nucl-ex/0502021.

[14] M. Tanabashi et al. "Review of Particle Physics". In: *Phys. Rev. D* 98 (3 Aug. 2018), p. 030001. DOI: 10.1103/PhysRevD.98.030001. URL: https://link.aps.org/doi/10.1103/PhysRevD.98.030001.

[15] A. O. Sushkov, W. J. Kim, D. A. R. Dalvit, and S. K. Lamoreaux. "New Experimental Limits on Non-Newtonian Forces in the Micrometer Range". In: *Physical Review Letters* 107.17 (Oct. 2011). ISSN: 1079-7114. DOI: 10.1103/physrevlett.107.171101. URL: http://dx.doi.org/10.1103/PhysRevLett.107.171101.

[16] D. Croon, T. E. Gonzalo, L. Graf, N. Košnik, and G. White. "GUT Physics in the Era of the LHC". In: *Frontiers in Physics* 7 (June 2019). ISSN: 2296-424X. DOI: 10.3389/fphy.2019.00076. URL: http://dx.doi.org/10.3389/fphy.2019.00076.

[17] E. Corbelli and P. Salucci. "The extended rotation curve and the dark matter halo of M33". In: *Monthly Notices of the Royal Astronomical Society* 311.2 (2000), pp. 441–447. DOI: 10.1046/j.1365-8711.2000.03075.x. eprint: https://onlinelibrary.wiley.com/doi/pdf/10.1046/j.1365-8711.2000.03075.x. URL: https://onlinelibrary.wiley.com/doi/abs/10.1046/j.1365-8711.2000.03075.x.

[18] S.M. Faber and R.E. Jackson. "Velocity dispersions and mass to light ratios for elliptical galaxies". In: *Astrophys. J.* 204 (1976), p. 668. DOI: 10.1086/154215.

[19] X.-P. Wu, T. Chiueh, L.-Z. Fang, and Y.-J. Xue. "A comparison of different cluster mass estimates: consistency or discrepancy?" In: *Monthly Notices of the Royal Astronomical Society* 301.3 (1998), pp. 861–871. DOI: 10.1046/j.1365-8711.1998.02055.x. eprint: https://onlinelibrary.wiley.com/doi/pdf/10.1046/j.1365-8711.1998.02055.x. URL: https://onlinelibrary.wiley.com/doi/abs/10.1046/j.1365-8711.1998.02055.x.

[20] C.S. Frenk and S.D.M. White. "Dark matter and cosmic structure". In: *Annalen der Physik* 524.9-10 (2012), pp. 507–534. DOI: 10.1002/andp.201200212. eprint: https://onlinelibrary.wiley.com/doi/pdf/10.1002/andp.201200212. URL: https://onlinelibrary.wiley.com/doi/abs/10.1002/andp.201200212.

[21] Planck Collaboration. "Planck 2013 results. I. Overview of products and scientific results". In: *A&A* 571 (2014), A1. DOI: 10.1051/0004-6361/201321529. URL: https://doi.org/10.1051/0004-6361/201321529.

[22] L. Bergström. "Non-baryonic dark matter: Observational evidence and detection methods". In: *Reports on Progress in Physics* 63 (May 2000), p. 793. DOI: 10.1088/0034-4885/63/5/2r3.

[23] M.B. Gavela, P. Hernandez, J. Orloff, and O. Pene. "Standard model CP violation and baryon asymmetry". In: *Mod. Phys. Lett. A* 9 (1994), pp. 795–810. DOI: 10.1142/S0217732394000629. arXiv: hep-ph/9312215.

[24] M.B. Gavela, P. Hernandez, J. Orloff, O. Pene, and C. Quimbay. "Standard model CP violation and baryon asymmetry. Part 2: Finite temperature". In: *Nucl. Phys. B* 430 (1994), pp. 382–426. DOI: 10.1016/0550-3213(94)00410-2. arXiv: hep-ph/9406289.

[25] P. Huet and E. Sather. "Electroweak baryogenesis and standard model CP violation". In: *Phys. Rev. D* 51 (1995), pp. 379–394. DOI: 10.1103/PhysRevD.51.379. arXiv: hep-ph/9404302.

[26] K. G. Wilson. "The Renormalization Group and Strong Interactions". In: *Phys. Rev. D* 3 (1971), p. 1818. DOI: 10.1103/PhysRevD.3.1818.

[27] M. Dine. "Naturalness Under Stress". In: *Ann. Rev. Nucl. Part. Sci.* 65 (2015), pp. 43–62. DOI: 10.1146/annurev-nucl-102014-022053. arXiv: 1501.01035 [hep-ph].

[28] Gerard 't Hooft, C. Itzykson, A. Jaffe, H. Lehmann, P.K. Mitter, I.M. Singer, and R. Stora, eds. *Recent Developments in Gauge Theories. Proceedings, Nato Advanced Study Institute, Cargese, France, August 26 - September 8, 1979*. Vol. 59. 1980, pp.1–438. DOI: 10.1007/978-1-4684-7571-5.

[29] L. Susskind. "Dynamics of Spontaneous Symmetry Breaking in the Weinberg-Salam Theory". In: *Phys. Rev. D* 20 (1979), pp. 2619–2625. DOI: 10.1103/PhysRevD.20.2619.

[30] Y. A Gelfand and E. P. Likhtman. "Extension of the algebra of Poincare group generators and violation of P invariance". In: *JETP Lett.* 13.8 (1971), pp. 323–325. URL: http://cds.cern.ch/record/433516.

[31] D.V. Volkov and V.P. Akulov. "Is the Neutrino a Goldstone Particle?" In: *Phys. Lett. B* 46 (1973), pp. 109–110. DOI: 10.1016/0370-2693(73)90490-5.

[32] J. Wess and B. Zumino. "Supergauge transformations in four dimensions". In: *Nucl. Phys. B* 70.CERN-TH-1753. 1 (1974), pp. 39–50. DOI: 10.1016/0550-3213(74)90355-1. URL: https://cds.cern.ch/record/201649.

[33] J. Wess and B. Zumino. "Supergauge Invariant Extension of Quantum Electrodynamics". In: *Nucl. Phys. B* 78 (1974), p. 1. DOI: 10.1016/0550-3213(74)90112-6.

[34] S. Ferrara and B. Zumino. "Supergauge Invariant Yang-Mills Theories". In: *Nucl. Phys. B* 79 (1974), p. 413. DOI: 10.1016/0550-3213(74)90559-8.

[35] A. Salam and J.A. Strathdee. "Supersymmetry and Nonabelian Gauges". In: *Phys. Lett. B* 51 (1974), pp. 353–355. DOI: 10.1016/0370-2693(74)90226-3.

[36] N. Sakai. "Naturalness in Supersymmetric Guts". In: *Z. Phys. C* 11 (1981), p. 153. DOI: 10.1007/BF01573998.

[37] S. Dimopoulos, S. Raby, and F. Wilczek. "Supersymmetry and the Scale of Unification". In: *Phys. Rev. D* 24 (1981), pp. 1681–1683. DOI: 10.1103/PhysRevD.24.1681.

[38] L. E. Ibanez and G. G. Ross. "Low-Energy Predictions in Supersymmetric Grand Unified Theories". In: *Phys. Lett. B* 105 (1981), pp. 439–442. DOI: 10.1016/0370-2693(81)91200-4.

[39] S. Dimopoulos and H. Georgi. "Softly Broken Supersymmetry and SU(5)". In: *Nucl. Phys. B* 193 (1981), pp. 150–162. DOI: 10.1016/0550-3213(81)90522-8.

[40] H. Goldberg. "Constraint on the Photino Mass from Cosmology". In: *Phys. Rev. Lett.* 50 (1983). Ed. by M.A. Srednicki. [Erratum: Phys.Rev.Lett. 103, 099905 (2009)], p. 1419. DOI: 10.1103/PhysRevLett.50.1419.

[41] J. R. Ellis, J.S. Hagelin, D. V. Nanopoulos, K. A. Olive, and M. Srednicki. "Supersymmetric Relics from the Big Bang". In: *Nucl. Phys. B* 238 (1984). Ed. by M.A. Srednicki, pp. 453–476. DOI: 10.1016/0550-3213(84)90461-9.

[42] S. P. Martin. "A Supersymmetry primer". In: *Perspectives on supersymmetry. Vol.2*. Ed. by Gordon L. Kane. Vol. 21. 2010, pp. 1–153. DOI: 10.1142/9789812839657_0001. arXiv: hep-ph/9709356.

[43] M. Dine. *Supersymmetry and String Theory: Beyond the Standard Model*. Cambridge University Press, 2007. DOI: 10.1017/CBO9780511618482.

[44] J. A. Bagger. "Weak scale supersymmetry: Theory and practice". In: *Theoretical Advanced Study Institute in Elementary Particle Physics (TASI 95): QCD and Beyond*. Apr. 1996, pp. 109–162. arXiv: hep-ph/9604232.

[45] I. J.R. Aitchison. "Supersymmetry and the MSSM: An Elementary introduction". In: (May 2005). arXiv: hep-ph/0505105.

[46] G. R. Farrar and P. Fayet. "Phenomenology of the Production, Decay, and Detection of New Hadronic States Associated with Supersymmetry". In: *Phys. Lett. B* 76 (1978), pp. 575–579. DOI: 10.1016/0370-2693(78)90858-4.

[47] L. E. Ibáñez and G. G. Ross. "Discrete gauge symmetries and the origin of baryon and lepton number conservation in supersymmetric versions of the standard model". In: *Nucl. Phys. B* 368.CERN-TH-6111-91 (1992), pp. 3–37. DOI: 10.1016/0550-3213(92)90195-H. URL: http://cds.cern.ch/record/245866.

[48] S. Weinberg. "Supersymmetry at Ordinary Energies. 1. Masses and Conservation Laws". In: *Phys. Rev. D* 26 (1982), p. 287. DOI: 10.1103/PhysRevD.26.287.

[49] N. Sakai and T. Yanagida. "Proton Decay in a Class of Supersymmetric Grand Unified Models". In: *Nucl. Phys. B* 197 (1982), p. 533. DOI: 10.1016/0550-3213(82)90457-6.

[50] M. Lisanti. "Lectures on Dark Matter Physics". In: *Theoretical Advanced Study Institute in Elementary Particle Physics: New Frontiers in Fields and Strings*. 2017, pp. 399–446. DOI: 10.1142/9789813149441_0007. arXiv: 1603.03797 [hep-ph].

[51] L. Randall and R. Sundrum. "A Large mass hierarchy from a small extra dimension". In: *Phys. Rev. Lett.* 83 (1999), pp. 3370–3373. DOI: 10.1103/PhysRevLett.83.3370. arXiv: hep-ph/9905221.

[52] L. Randall and R. Sundrum. "An Alternative to compactification". In: *Phys. Rev. Lett.* 83 (1999), pp. 4690–4693. DOI: 10.1103/PhysRevLett.83.4690. arXiv: hep-th/9906064.

[53] C. F. Kolda. "Gauge mediated supersymmetry breaking: Introduction, review and update". In: *Nucl. Phys. B Proc. Suppl.* 62 (1998). Ed. by M. Cvetic and P. Langacker, pp. 266–275. DOI: 10.1016/S0920-5632(97)00667-1. arXiv: hep-ph/9707450.

[54] L. Randall and R. Sundrum. "Out of this world supersymmetry breaking". In: *Nucl. Phys. B* 557 (1999), pp. 79–118. DOI: 10.1016/S0550-3213(99)00359-4. arXiv: hep-th/9810155.

[55] A. Pomarol and R. Rattazzi. "Sparticle masses from the superconformal anomaly". In: *JHEP* 05 (1999), p. 013. DOI: 10.1088/1126-6708/1999/05/013. arXiv: hep-ph/9903448.

[56] A. H. Chamseddine, R. Arnowitt, and Pran Nath. "Locally Supersymmetric Grand Unification". In: *Phys. Rev. Lett.* 49 (14 Oct. 1982), pp. 970–974. DOI: 10.1103/PhysRevLett.49.970. URL: https://link.aps.org/doi/10.1103/PhysRevLett.49.970.

[57] R. Arnowitt and P. Nath. "Developments in Supergravity Unified Models". In: *Perspectives on supersymmetry. Vol.2*. Ed. by Gordon L. Kane. Vol. 21. 2010, pp. 222–243. DOI: 10.1142/9789814307505_0003. arXiv: 0912.2273 [hep-ph].

[58] R. Barbieri and G. F. Giudice. "Upper bounds on supersymmetric particle masses". In: *Nucl. Phys. B* 306.CERN-TH-4825-87 (Aug. 1987), 63–76. 19 p. DOI: 10.1016/0550-3213(88)90171-X. URL: https://cds.cern.ch/record/180560.

[59] B. de Carlos and J.A. Casas. "One-loop analysis of the electroweak breaking in supersymmetric models and the fine-tuning problem". In: *Phys. Lett. B* 309.hep-ph/9303291. CERN-TH-6835-93. IEM-FT-70 (Mar. 1993), 320–328. 16 p. DOI: 10.1016/0370-2693(93)90940-J. URL: http://cds.cern.ch/record/247620.

[60] ATLAS Collaboration. "Summary of the searches for squarks and gluinos using $\sqrt{s} = 8$ TeV pp collisions with the ATLAS experiment at the LHC". In: *JHEP* 10 (2015), p. 054. DOI: 10.1007/JHEP10(2015)054. arXiv: 1507.05525 [hep-ex].

[61] ATLAS Collaboration. "Search for electroweak production of supersymmetric particles in final states with two or three leptons at $\sqrt{s} = 13$ TeV with the ATLAS detector". In: *Eur. Phys. J. C* 78.12 (2018), p. 995. DOI: 10.1140/epjc/s10052-018-6423-7. arXiv: 1803.02762 [hep-ex].

[62] ATLAS Collaboration. "Summary of the ATLAS experiment's sensitivity to supersymmetry after LHC Run 1 — interpreted in the phenomenological MSSM". In: *JHEP* 10 (2015), p. 134. DOI: 10.1007/JHEP10(2015)134. arXiv: 1508.06608 [hep-ex].

[63] H. Baer, V. Barger, J. S. Gainer, P. Huang, M. Savoy, H. Serce, and X. Tata. "What hadron collider is required to discover or falsify natural supersymmetry?" In: *Phys. Lett. B* 774 (2017), pp. 451–455. DOI: 10.1016/j.physletb.2017.09.086. arXiv: 1702.06588 [hep-ph].

[64] S. Rappoccio. "The experimental status of direct searches for exotic physics beyond the standard model at the Large Hadron Collider". In: *Rev. Phys.* 4 (2019), p. 100027. DOI: 10.1016/j.revip.2018.100027. arXiv: 1810.10579 [hep-ex].

[65] S. Diglio, L. Feligioni, and G. Moultaka. "Stashing the stops in multijet events at the LHC". In: *Phys. Rev. D* 96.5 (2017), p. 055032. DOI: 10.1103/PhysRevD.96.055032. arXiv: 1611.05850 [hep-ph].

[66] T. Flacke, D. W. Kang, K. Kong, G. Mohlabeng, and S. C. Park. "Electroweak Kaluza-Klein Dark Matter". In: *JHEP* 04 (2017), p. 041. DOI: 10.1007/JHEP04(2017)041. arXiv: 1702.02949 [hep-ph].

[67] M. Fairbairn, A.C. Kraan, D.A. Milstead, T. Sjostrand, Peter Z. Skands, and T. Sloan. "Stable Massive Particles at Colliders". In: *Phys. Rept.* 438 (2007), pp. 1–63. DOI: 10.1016/j.physrep.2006.10.002. arXiv: hep-ph/0611040.

[68] H. Baer, K. Cheung, and J. F. Gunion. "A Heavy gluino as the lightest supersymmetric particle". In: *Phys. Rev. D* 59 (1999), p. 075002. DOI: 10.1103/PhysRevD.59.075002. arXiv: hep-ph/9806361.

[69] R. Barbier et al. "R-parity violating supersymmetry". In: *Phys. Rept.* 420 (2005), pp. 1–202. DOI: 10.1016/j.physrep.2005.08.006. arXiv: hep-ph/0406039.

[70] H. K. Dreiner. "An Introduction to explicit R-parity violation". In: *Perspectives on supersymmetry. Vol.2*. Ed. by Gordon L. Kane. Vol. 21. 2010, pp. 565–583. DOI: 10.1142/9789814307505_0017. arXiv: hep-ph/9707435.

[71] ATLAS Collaboration. "Search for heavy charged long-lived particles in the ATLAS detector in 36.1 fb^{-1} of proton-proton collision data at $\sqrt{s} = 13$ TeV". In: *Phys. Rev. D* 99.arXiv:1902.01636 (Feb. 2019), 092007. 34 p. DOI: 10.1103/PhysRevD.99.092007. URL: https://cds.cern.ch/record/2655808.

[72] CERN. *Our Member States*. 2020. URL: https://home.cern/about/who-we-are/our-governance/member-states (visited on 07/14/2020).

[73] "About CERN". In: (Jan. 2012). URL: http://cds.cern.ch/record/1997225.

[74] L. R Evans and P. Bryant. "LHC Machine". In: *JINST* 3 (2008). This report is an abridged version of the LHC Design Report (CERN-2004-003), S08001. 164 p. DOI: 10.1088/1748-0221/3/08/S08001. URL: http://cds.cern.ch/record/1129806.

[75] ATLAS Collaboration. "The ATLAS Experiment at the CERN Large Hadron Collider". In: *JINST* 3 (2008). Also published by CERN Geneva in 2010, S08003. 437 p. DOI: 10.1088/1748-0221/3/08/S08003. URL: https://cds.cern.ch/record/1129811.

[76] *LEP design report*. By the LEP Injector Study Group. Geneva: CERN, 1983. URL: https://cds.cern.ch/record/98881.

[77] *LEP design report*. Copies shelved as reports in LEP, PS and SPS libraries. Geneva: CERN, 1984. URL: https://cds.cern.ch/record/102083.

[78] C. Wyss. *LEP design report, v.3: LEP2*. Vol. 1-2 publ. in 1983-84. Geneva: CERN, 1996. URL: https://cds.cern.ch/record/314187.

[79] N. Grau. *The Heavy Ion Physics Program with ATLAS at the LHC*. 2007. arXiv: 0706.1983 [nucl-ex].

[80] V. Shiltsev and F. Zimmermann. *Modern and Future Colliders*. 2020. arXiv: 2003.09084 [physics.acc-ph].

[81] CERN. *Facts and figures about the LHC*. 2020. URL: https://home.cern/resources/faqs/facts-and-figures-about-lhc (visited on 07/14/2020).

[82] ALICE Collaboration. "The ALICE experiment at the CERN LHC". In: *JINST* 3 (2008), S08002. DOI: 10.1088/1748-0221/3/08/S08002.

[83] CMS Collaboration. "The CMS Experiment at the CERN LHC". In: *JINST* 3 (2008), S08004. DOI: 10.1088/1748-0221/3/08/S08004.

[84] LHCb Collaboration. "The LHCb Detector at the LHC". In: *JINST* 3 (2008), S08005. DOI: 10.1088/1748-0221/3/08/S08005.

[85] E. Mobs. "The CERN accelerator complex. Complexe des accélérateurs du CERN". In: (July 2016). General Photo. URL: https://cds.cern.ch/record/2197559.

[86] CERN. *CERN's accelerator complex*. 2020. URL: https://home.cern/science/accelerators/accelerator-complex (visited on 07/14/2020).

[87] ATLAS Collaboration. "ATLAS Run 1 searches for direct pair production of third-generation squarks at the Large Hadron Collider". In: *The European Physical Journal C* 75.10 (Oct. 2015). ISSN: 1434-6052. DOI: 10.1140/epjc/s10052-015-3726-9. URL: http://dx.doi.org/10.1140/epjc/s10052-015-3726-9.

[88] ATLAS Collaboration. "ATLAS data quality operations and performance for 2015–2018 data-taking". In: *Journal of Instrumentation* 15.04 (Apr. 2020), P04003–P04003. ISSN: 1748-0221. DOI: 10.1088/1748-0221/15/04/p04003. URL: http://dx.doi.org/10.1088/1748-0221/15/04/P04003.

[89] CERN. *Record luminosity: well done LHC*. 2020. URL: https://home.cern/news/news/accelerators/record-luminosity-well-done-lhc (visited on 07/16/2020).

[90] ATLAS Collaboration. *Luminosity Public Results Run 2*. 2020. URL: https://twiki.cern.ch/twiki/bin/view/AtlasPublic/LuminosityPublicResultsRun2#2015_pp_Collisions (visited on 07/16/2020).

[91] ATLAS Collaboration. *Detector - Magnet System*. 2020. URL: https://atlas.cern/discover/detector/magnet-system (visited on 07/17/2020).

[92] J. Pequenao and P. Schaffner. "How ATLAS detects particles: diagram of particle paths in the detector". Jan. 2013. URL: https://cds.cern.ch/record/1505342.

[93] U. Egede. "The search for a Standard Model Higgs at the LHC and electron identification using transition radiation in the ATLAS tracker". PhD thesis. Lund U., 1998.

[94] Yiming Abulaiti. "Search for Pair-Produced Supersymmetric Top Quark Partners with the ATLAS Experiment". PhD thesis. Stockholm U., Aug. 2016.

[95] R. E. Owen. "The ATLAS Trigger System". In: (Feb. 2018). URL: http://cds.cern.ch/record/2302730.

[96] ATLAS Collaboration. *The Inner Detector*. 2020. URL: https://atlas.cern/discover/detector/inner-detector (visited on 07/20/2020).

[97] K. Potamianos. "The upgraded Pixel detector and the commissioning of the Inner Detector tracking of the ATLAS experiment for Run-2 at the Large Hadron Collider". In: *PoS* EPS-HEP2015 (2015), p. 261. arXiv: 1608.07850 [physics.ins-det].

[98] H Oide. *The Pixel Detector of the ATLAS experiment for the Run 2 at the Large Hadron Collider*. Tech. rep. ATL-INDET-PROC-2014-005. 12. Geneva: CERN, Sept. 2014. DOI: 10.1088/1748-0221/9/12/C12034. URL: http://cds.cern.ch/record/1757476.

[99] M. Capeans, G. Darbo, K. Einsweiller, M. Elsing, T Flick, M Garcia-Sciveres, C Gemme, H Pernegger, O Rohne, and R Vuillermet. *ATLAS Insertable B-Layer Technical Design Report*. Tech. rep. CERN-LHCC-2010-013. ATLAS-TDR-19. Sept. 2010. URL: https://cds.cern.ch/record/1291633.

[100] ATLAS Collaboration. "ATLAS pixel detector electronics and sensors". In: *Journal of Instrumentation* 3.07 (July 2008), P07007–P07007. DOI: 10.1088/1748-0221/3/07/p07007. URL: https://doi.org/10.1088%2F1748-0221%2F3%2F07%2Fp07007.

[101] N. Barlow. *Operation of the ATLAS Semiconductor Tracker*. Tech. rep. ATL-INDET-PROC-2010-003. Geneva: CERN, Feb. 2010. URL: http://cds.cern.ch/record/1237401.

[102] B. Mindur. *ATLAS Transition Radiation Tracker (TRT): Straw tubes for tracking and particle identification at the Large Hadron Collider*. Tech. rep. ATL-INDET-PROC-2016-001. Geneva: CERN, Mar. 2016. DOI: 10.1016/j.nima.2016.04.026. URL: https://cds.cern.ch/record/2139567.

[103] *ATLAS liquid-argon calorimeter: Technical Design Report*. Technical Design Report ATLAS. Geneva: CERN, 1996. URL: https://cds.cern.ch/record/331061.

[104] ATLAS Collaboration. *ATLAS tile calorimeter: Technical Design Report*. Technical Design Report ATLAS. Geneva: CERN, 1996. URL: https://cds.cern.ch/record/331062.

[105] N J Buchanan et al. "Design and implementation of the Front End Board for the readout of the ATLAS liquid argon calorimeters". In: *Journal of Instrumentation* 3.03 (Mar. 2008), P03004–P03004. DOI: 10.1088/1748-0221/3/03/p03004. URL: https://doi.org/10.1088%2F1748-0221%2F3%2F03%2Fp03004.

[106] E. Diehl. *Calibration and Performance of the ATLAS Muon Spectrometer*. 2011. arXiv: 1109.6933 [physics.ins-det].

[107] ATLAS Collaboration. "Commissioning of the ATLAS Muon Spectrometer with cosmic rays". In: *The European Physical Journal C* 70.3 (Oct. 2010), pp. 875–916. ISSN: 1434-6052. DOI: 10.1140/epjc/s10052-010-1415-2. URL: http://dx.doi.org/10.1140/epjc/s10052-010-1415-2.

[108] ATLAS Collaboration. *Barrel sketch*. 2020. URL: https://atlas-muon-align.web.cern.ch/Plots/atlas_sketch.png (visited on 07/22/2020).

[109] J. Wotschack. *ATLAS Muon Chamber Construction Parameters for CSC, MDT, and RPC chambers*. Tech. rep. ATL-MUON-PUB-2008-006. ATL-COM-MUON-2008-008. Back-up document for the ATLAS Detector Paper. Geneva: CERN, Apr. 2008. URL: http://cds.cern.ch/record/1099400.

[110] ATLAS Collaboration. *Expected performance of the ATLAS experiment: detector, trigger and physics*. Geneva: CERN, 2009. URL: https://cds.cern.ch/record/1125884.

[111] ATLAS Collaboration. *ATLAS muon spectrometer: Technical Design Report*. Technical Design Report ATLAS. Geneva: CERN, 1997. URL: https://cds.cern.ch/record/331068.

[112] ATLAS Muon Group. *Monitored drift tubes in ATLAS*. 2020. URL: https://cds.cern.ch/record/319197/files/muon-96-129.pdf (visited on 07/22/2020).

[113] Y Arai et al. "ATLAS Muon Drift Tube Electronics". In: *JINST* 3.ATL-MUON-PUB-2008-008. (Apr. 2008), P09001. 58 p. DOI: 10.1088/1748-0221/3/09/P09001. URL: http://cds.cern.ch/record/1100199.

[114] D Boscherini. *Performance and operation of the ATLAS Resistive Plate Chamber system in LHC Run-1*. Tech. rep. ATL-MUON-PROC-2014-005. 12. Geneva: CERN, Sept. 2014. DOI: 10.1088/1748-0221/9/12/C12039. URL: http://cds.cern.ch/record/1753173.

[115] A Aloisio et al. *The RPC Level-1 Muon Trigger of the ATLAS Experiment at the LHC*. Tech. rep. ATL-DAQ-CONF-2006-004. ATL-COM-DAQ-2006-011. Geneva: CERN, Mar. 2006. DOI: 10.1109/RTC.2005.1547462. URL: http://cds.cern.ch/record/934478.

[116] ATLAS Collaboration. "Search for heavy charged long-lived particles in proton-proton collisions at $\sqrt{s} = 13$ TeV using an ionisation measurement with the ATLAS detector". In: *Phys. Lett. B* 788.arXiv:1808.04095 (Aug. 2018), 96–116. 21 p. DOI: 10.1016/j.physletb.2018.10.055. URL: http://cds.cern.ch/record/2634050.

[117] D. C. Swift and J. M. McNaney. "Approximate, analytic solutions of the Bethe equation for charged particle range". In: (Dec. 2008). arXiv: 0901.4145 [cond-mat.other].

[118] H. Schieck. *Nuclear Reactions - An Introduction*. Vol. 882. Jan. 2014. ISBN: 978-3-642-53985-5. DOI: 10.1007/978-3-642-53986-2.

[119] C. Becchi and M. D'Elia. "Introduction to the Basic Concepts of Modern Physics". In: *Introduction to the Basic Concepts of Modern Physics: Special Relativity, Quantum and Statistical Physics, UNITEXT. ISBN 978-88-470-1615-6. Springer-Verlag Milan, 2010* (Jan. 2010). DOI: 10.1007/978-88-470-1616-3.

[120] S. Tarem, Z. Tarem, N. Panikashvili, and O. Belkind. "MuGirl – Muon identification in the ATLAS detector from the inside out". In: *2006 IEEE Nuclear Science Symposium Conference Record*. Vol. 1. 2006, pp. 617–621.

[121] D. Fassouliotis, T. Lagouri, A. Poppleton, S. Robins, G. D. Stavropoulos, and I. Vichou. *Muon Identification using the MUID package*. Tech. rep. ATL-COM-MUON-2003-003. Geneva: CERN, Nov. 2000. URL: https://cds.cern.ch/record/681596.

[122] R. Nicolaidou, L. Chevalier, S. Hassani, J.F. Laporte, E. Le Menedeu, and A. Ouraou. "Muon identification procedure for the ATLAS detector at the LHC using Muonboy reconstruction package and tests of its performance using cosmic rays and single beam data". In: *J. Phys. Conf. Ser.* 219 (2010). Ed. by Jan Gruntorad and Milos Lokajicek, p. 032052. DOI: 10.1088/1742-6596/219/3/032052.

[123] ATLAS Collaboration. "Muon reconstruction performance of the ATLAS detector in proton–proton collision data at $\sqrt{s}$ =13 TeV". In: *Eur. Phys. J. C* 76.5 (2016), p. 292. DOI: 10.1140/epjc/s10052-016-4120-y. arXiv: 1603.05598 [hep-ex].

[124] S. Tarem, Shikma Bressler, H. Nomoto, and Alessandro Di Mattia. "Trigger and Reconstruction for a heavy long lived charged particles with the ATLAS detector". In: *European Physical Journal C* 62 (July 2009), pp. 281–292. DOI: 10.1140/epjc/s10052-009-1040-0.

[125] S. Tarem, S. Bressler, H. Nomoto, and A. Di Mattia. "Trigger and reconstruction for heavy long-lived charged particles with the ATLAS detector". In: *Eur. Phys. J. C* 62 (2009), pp. 281–292. DOI: 10.1140/epjc/s10052-009-1040-0.

[126] S Tarem. *Reconstruction And Identification Of Heavy Long-Lived Particles At The ATLAS Detector At The LHC*. Tech. rep. ATL-PHYS-PROC-2009-123. Geneva: CERN, Oct. 2009. URL: http://cds.cern.ch/record/1210439.

[127] M. Habedank. "Calibrating the ATLAS Muon Spectrometer for a Search for Charged Stable Massive Particles". MA thesis. Ludwig-Maximilians-Universität München, Nov. 2018.

[128] M. Adersberger. "Searches for Heavy Charged Long-Lived Particles with the ATLAS Detector". PhD thesis. Ludwig-Maximilians-Universität München, Nov. 2018.

[129] ATLAS Collaboration. *Luminosity determination in pp collisions at $\sqrt{s} = 13$ TeV using the ATLAS detector at the LHC*. Tech. rep. ATLAS-CONF-2019-021. Geneva: CERN, June 2019. URL: https://cds.cern.ch/record/2677054.

[130] J. Catmore, P. Laycock, E. Gramstad, T. Gillam, J. Cranshaw, N. Ozturk, and G. Stewart. *A New Petabyte-scale Data Derivation Framework for ATLAS*. Tech. rep. ATL-SOFT-PROC-2015-041. 7. Geneva: CERN, May 2015. DOI: 10.1088/1742-6596/664/7/072007. URL: https://cds.cern.ch/record/2016628.

[131] J. Heinrich. "Search for Charged Stable Massive Particles with the ATLAS Detector". PhD thesis. Ludwig-Maximilians-Universität München, Mar. 2018.

Declaration of Authorship

Hiermit erkläre ich, die vorliegende Arbeit selbstständig verfasst zu haben und keine anderen als die in der Arbeit angegebenen Quellen und Hilfsmittel benutzt zu haben.

München, _____

Unterschrift: _____